# ABSTRACT


| | |
|---|---|
| Title of Document: | THE SEARCH FOR NEUTRALINO DARK MATTER WITH THE AMANDA NEUTRINO TELESCOPE |
| | Ralf Ehrlich, Doctor of Philosophy, 2009 |
| Directed By: | Professor Gregory Sullivan<br>Department of Physics |

There is convincing indirect evidence based on cosmological data that approximately one quarter of the universe is made of dark matter. However, to this date there is no direct detection of the dark matter and its nature is unknown. Most theories suggest that this dark matter is made of Weakly Interacting Massive Particles (WIMPs), or more specifically: supersymmetric particles. The most promising candidate out of the supersymmetric particles is the lightest neutralino. These neutralinos can get trapped in the gravitational field of the Earth, where they accumulate and annihilate. The annihilation products decay and produce neutrinos (among other particles). These neutrinos (the focus is on muon-neutrinos here) can be detected with the AMANDA neutrino telescope located between one and two kilometers deep in the ice of the glacier near the South Pole.

Neutrinos cannot be detected directly. However, there is a small possibility that they interact with nuclei of the ice and create charged leptons. These charged leptons continue to travel in the same direction as the neutrinos (accompanied by electromagnetic/hadronic cascades, and δ electrons). As long as their speed is higher than the speed of light of the ice, they emit Cherenkov radiation which can be captured by photomultipliers installed inside the ice. The signals collected by the photomultipliers can be used to reconstruct the track of the lepton.

AMANDA – the Antarctic Muon and Neutrino Detector Array – makes use of the unique properties of the neutrino: Since neutrinos interact only weakly, they can travel through the Earth without being stopped. Therefore all detected particles which have been identified as upward going (i.e. through the Earth coming) must have been produced by charged leptons originating from neutrinos after they reacted with the nuclei of the ice. All other particles which do not come from below are rejected.

If the neutrino flux coming from the neutralino annihilation inside Earth is strong enough to be detected with AMANDA, it should show up as an excess over the expected neutrino flux, which comes from the atmospheric neutrinos produced in the northern hemisphere. This analysis which used data from 2001 and 2002 showed that there is no significant excess, yielding an upper limit on the neutrino flux that could have come from WIMP annihilation.

# THE SEARCH FOR NEUTRALINO DARK MATTER WITH THE AMANDA NEUTRINO TELESCOPE

By

Ralf Ehrlich

Dissertation submitted to the Faculty of the Graduate School of the
University of Maryland, College Park, in partial fulfillment
of the requirements for the degree of
Doctor of Philosophy
2009

Advisory Committee:
Professor Gregory Sullivan, Chair
Professor Kara Hoffman
Professor Rabindra Mohapatra
Professor Sarah Eno
Professor Coleman Miller

# Dedication

Für Mama und Papa

To Eddie

# Content

# List of Tables

# List of Figures

# Chapter 1: Introduction

This dissertation describes the analysis of data gathered from the AMANDA neutrino telescope. The analysis is done in an attempt to search for neutralino dark matter. The term "neutralino dark matter" indicates already that the search for these particles is motivated by two sides: the subatomic small scales and the astronomical large scales. Both points of view will be discussed in chapters 2 and 3. It will be shown that the universe contains a large fraction of matter – the dark matter – which consists of yet undetected and unknown particles. On the particle physics side, there is a theory which predicts the existence of a new set of particles – the supersymmetric particles. The neutralinos are a subset of these supersymmetric particles, where the lightest neutralino has the properties consistent with the properties inferred from the dark matter.

These neutralinos can get gravitationally trapped in the Earth. They accumulate and annihilate in the center of the Earth, and the annihilation products decay with a fraction of these decay products being neutrinos. These steps are explained in chapter 4.

The dissertation continues in chapter 5 with an explanation about the detection method of these neutrinos with the AMANDA telescope. Since they cannot be detected directly, one has to rely on the small probability that these neutrinos undergo a charged-current interaction with nuclei of the ice in and around the detector. This reaction leads to a muon. Usually it will travel faster than the speed of light in ice. Since it is a charged particle it will emit Cherenkov radiation. This Cherenkov radiation can be detected by the photomultiplier tubes (PMTs) in the ice. The data collected by the PMTs is used to reconstruct the track of the muon. Electromagnetic and hadronic cascades and $\delta$

electrons, which are created along the muon path, emit additional Cherenkov radiation, which increases the chance for an accurate reconstruction of the muon track.

In order to be able to distinguish these neutrino-turned-muons from the large cosmic ray background, one uses only events with upward going tracks, i.e. tracks which originate inside Earth. The neutrinos are able to travel "up" through the Earth, while the cosmic ray particles get absorbed. Therefore one can be confident that a particle coming from below must have been a neutrino. Particles which come from above are generally ignored, since no such assumption about the nature of the particle can be made, even though most of them are atmospheric muons produced by cosmic rays interactioning in the atmosphere.

Chapters 6, 7 and 8 focus on the data analysis of the data collected by AMANDA. It will be checked whether there is an excess of events over the expected number of events coming from atmospheric neutrinos (neutrinos which are produced in the atmosphere at the other side of the Earth). Such an excess would indicate a signal which may have originated from neutralino annihilation inside Earth.

# Chapter 2: Astrophysical Motivations

In this chapter, it will be shown that there is a large fraction of matter in the universe which we have no knowledge of yet. This matter is the so-called dark matter, a term which is used for matter which does not interact electromagnetically (i.e. it is invisible), but has effects on ordinary matter through its gravitational interaction. Evidence concerning the existence of this dark matter has been gathered by various methods. These methods and their results will be discussed in the first subsection. It will also be shown that there are arguments which suggest that dark matter is made of neutralinos – a type of particles which will be introduced in chapter 3. Assuming the dark matter is made of neutralinos, it is possible to estimate the neutralino's present relic abundance in the universe. This is done in the second subsection.

## 2.1 The dark matter problem

The first indications of a "problem" came from Jan Oort who studied the motion of stars in the Milkyway,[1] and Fritz Zwicky who observed the velocities of nebulae inside the Coma galaxy cluster.[2,3] By using Newtonian gravity they were able to estimate the mass of the respective systems. They found that the masses were much larger than they expected based on the luminosity of the Milkyway / Coma galaxy cluster.

Rotations curves of many galaxies, which were measured later, supported these initial findings. Here, the velocities of components of a galaxy are measured for different

distances from the center of the galaxy (see Figure 1). The velocities can be calculated from the (Doppler) redshift of light emitted by stars, neutral hydrogen (21-cm-radiation), etc. If the mass of galaxies were concentrated in the center bulge – as one might guess from the distribution of the stars in the galaxy – one would expect the velocity of stars (or gases, etc.) to decrease the further away from the center they are orbiting, similar to the planets orbiting around our sun. With Newton's law to $\frac{GMm}{r^2} = \frac{mv^2}{r}$ one would have a drop in velocity proportional to $v \sim r^{-1/2}$. However, this was not what was found. It turned out that the velocities were approximately unchanged even far away from the center of the galaxy. There were two major theories put forward: The first one was the

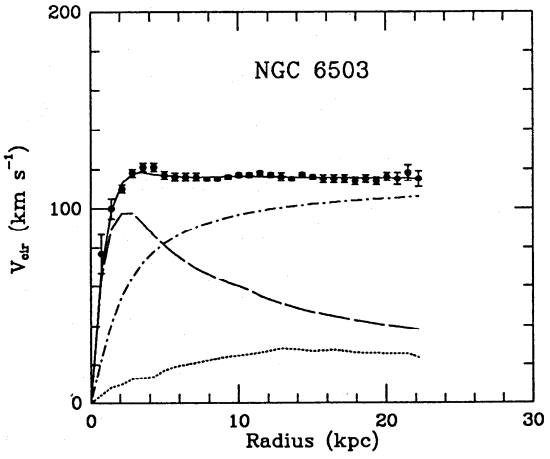


*Figure 1 Three-parameter dark-halo fit to the rotation curve of the spiral galaxy NGC 8603* [4]
dashed line: contribution of visible components
dotted line: contribution of gas
dash-dot line: contribution of dark halo
dots with error bars: measured velocities
solid line (under measured values): all three contributions combined

proposal of a large amount of matter that was invisible, hence "Dark Matter". The second one was that the laws of gravitation are somehow different in faraway regions of the universe. Today, the latter suggestion is essentially dismissed, since no further evidence for this idea could be found, but more and more hints for the existence of dark matter have been collected over the years (see next paragraphs).

A very recent finding (2006) came from the observation of the collision of two clusters of galaxies, where the smaller one is the so-called bullet cluster, which passed through the larger cluster. During the collision, the component of the two clusters (intracluster plasma, galaxies) got separated from each other. While the galaxies of the colliding clusters pass through each other like collisionless particles,[5] the plasma components get slowed down through their interaction with each other and lag behind of the stellar components. The gravitational potential of the clusters should essentially be created by the intracluster plasma, since it is the major mass component.[5] However, an analysis of the gravitational lensing maps showed that this is not the case (see Figure 2 – right image). It turned out that gravitational potential lines follow the distribution of the galaxies (see Figure 2 – left image),[5] which would be the case if there was another ("dark") component with negligible interaction (just like the galaxies, so that it would have a similar spatial distribution), but with much higher mass. This result provides strong evidence for the existence of dark matter.[5]

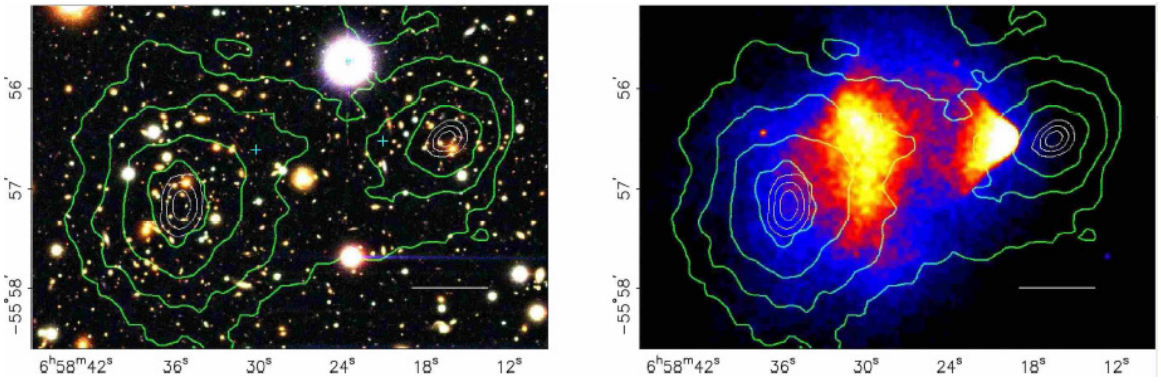


*Figure 2 Images of the merging cluster 1E0657−558*[5]
The left image was taken by the Magellan Telescope and shows the distribution of the galaxies. The right image was taken by the Chandra X-Ray Observatory and shows the intracluster plasma. The green contours on both images are related to the mass densities calculated from information obtained by the analysis of the gravitational lensing.

The most convincing evidence comes from latest results of the Wilkinson Microwave Anisotropy Probe (WMAP). The goal of this mission (which started in 2001) was to map the cosmic microwave background (CMB), or rather its anisotropies on various scales (Figure 3). The microwave background reaches back to just 380,000 years after the Big Bang (about 13.7 billion years ago),[6] the time of decoupling (see next paragraph).

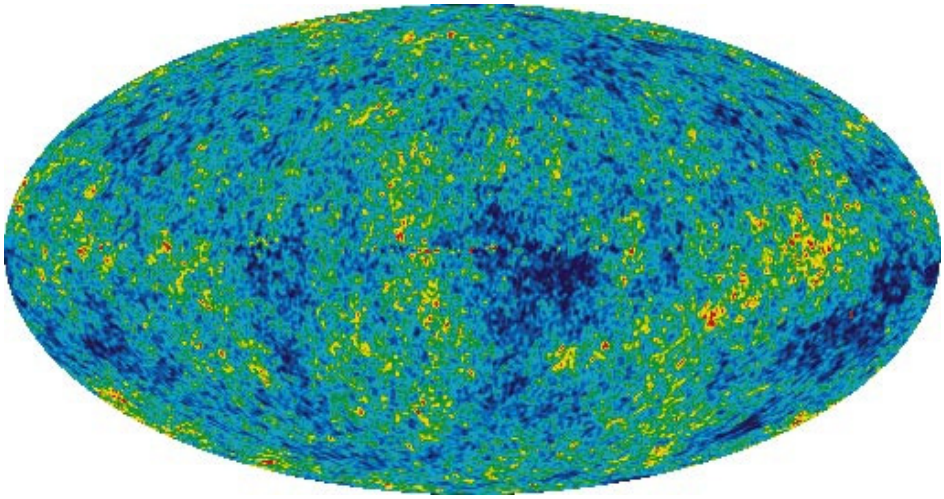

*Figure 3 The detailed, all-sky picture of the infant universe from three years of WMAP data.*[7]
The image reveals 13.7 billion year old temperature fluctuations (shown as color differences) that correspond to the seeds that grew to become the galaxies. The signal from our Galaxy was subtracted using the multi-frequency data. This image shows a temperature range of ± 200 μK.
Credit: NASA / WMAP Science Team

Before this time, the photons were subject to constant Thomson scattering with the free electrons which filled the young universe, so that the universe was opaque to photons, and the photons were in thermal equilibrium with the electrons. Thomson scattering with protons (and heavier nuclei) can be neglected as their mass is much higher, and therefore its scattering cross-section is much lower.[8] However, the protons are coupled to the electrons through the Coulomb interaction,[8] which keeps them in thermal equilibrium with the photons as well. The expansion of the universe led to a decrease of the temperature of the universe. Eventually the temperature dropped to a point, where electrons and protons could form neutral hydrogen atoms, i.e. they were not ionized

anymore by the photons. This happened at a temperature of about 3500K, which is equivalent to 0.3eV (which is much smaller than the ionization energy of 13.6eV)[9,10]. This process reduced the number of free electrons in the universe, which in turn reduced the Thomson scattering rate between photons and electrons. At the point in the history of the universe when the scattering rate dropped below the expansion rate of the universe, the photons decoupled from the electrons. That means they were no longer in thermal equilibrium with the electrons. This happened "shortly" after recombination when the temperature was 3000K (or 0.26eV)[9]. The photons could now travel freely (since Thomson scattering did not play a role anymore), and the universe became transparent to photons. As the universe further expanded, the wavelengths of these photons were scaled as well (while the blackbody spectrum was preserved), so that this radiation has now a wavelength distribution in the millimeter range. The distribution is that of a blackbody radiation with a temperature of 2.725K.[6] This radiation is nearly perfectly isotropic. However, it does have some tiny anisotropies (in the order of μK). This is the most interesting feature, since these anisotropies have its origin (for the most part) in fluctuations of the gravitational fields (gravitational red-/blue-shift which indicate inhomogeneities in the matter distribution) and in fluctuations of the photonenergy density right at the time of decoupling from matter. Before this time, photons, electrons and baryons (protons and heavier nuclei) were in thermal equilibrium, so that density fluctuations of the microwave background point to inhomogeneities in the baryon distribution.

In order to understand these anisotropies, one has to go back in time even further, and discuss some aspects of the structure formation in the early universe. Small fluctuations in the matter density can grow as soon as the universe becomes matter dominated,[11] i.e. the gravitational potential of over-dense regions in the universe attracts even more matter. However, this was possible only for non-baryonic (dark) matter. On the other hand, baryonic matter was still coupled to the photons (or more precisely the electrons are coupled to the photons through Thomson scattering, and heavier baryons such as hydrogen, helium, etc. are coupled to the electrons via Coulomb interaction). Therefore the radiation pressure from the photons counteracts any increase of the density of the baryonic matter. Both forces, the gravitational force originating from density fluctuations in the matter distribution in the universe and the restoring forces of the radiation pressure, led to oscillations of the baryon's density. The oscillations cause temporary density variations of the baryon-photon mixture. At the time of decoupling, the connection between baryons and photons is severed, and the oscillations stop. Afterwards the photons were allowed to stream freely through the universe leading to the CMB we see today. However, the photon's density fluctuations from the time when the oscillations ended did not vanish – they are still visible as small anisotropies in the CMB. After decoupling, baryons were not subject to the radiation pressure anymore so that they could fall into the potential wells provided by the dense regions of dark matter (which were able to grow even before decoupling).[12] From that time on, inhomogeneities of the baryons started growing (soon catching up to the size of the dark matter inhomogeneities), eventually leading to the structure of the universe as we see today. If there was no dark matter present, then the growth of matter density perturbations could

not have started after decoupling, and there would not have been enough time for them to grow to present size (or in other words, the anisotropies in the CMB needed to be much larger than observed in order to accommodate such a model).[12,13,14]

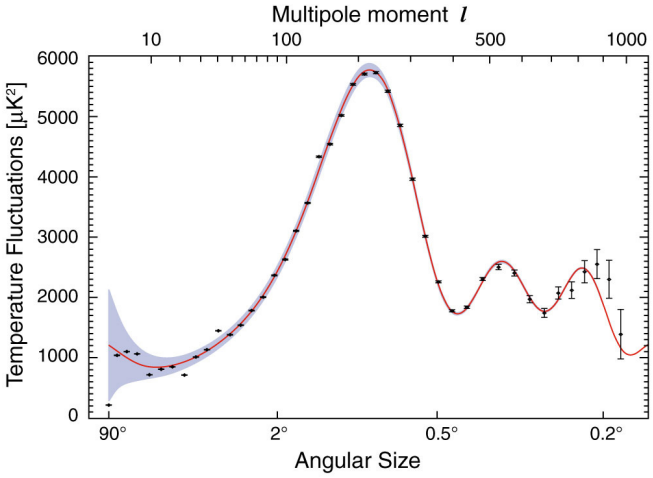


*Figure 4 Temperature Fluctuation by Angular Size*[6]
This graph illustrates how much the temperature fluctuates on different anglular sizes in the map. Very large angles are on the left, and smaller angles are on the right. Note that there is a large first peak, illustrating a preferred spot size in the map. This means that there is a preferred length for the sound waves in the early universe, just as a guitar string length produces a specific note. The second and third peaks are the harmonic overtones of the first peak. The third overtone is now clearly captured in the new 5-year WMAP data.
Credit: NASA / WMAP Science Team

The anisotropies of the CMB are analyzed in such a way that the temperature differences between two directions with a particular angular separation are measured. This is done across the entire sky for a wide range of angular differences. The temperature differences are plotted versus the angular separations (or rather multipole moments) leading to a power spectrum (Figure 4). The peaks seen in this power spectrum are related to the oscillation modes of the baryon-photon mixture before decoupling. Their positions in the histogram can be used to calculate key information about the universe:[15] the relative densities of the dark matter $\Omega_{\text{dark matter}} = 0.228 \pm 0.013$, the baryons $\Omega_{\text{baryons}} = 0.0456 \pm 0.0015$, the dark energy $\Omega_{\Lambda} = 0.726 \pm 0.015$, the photons $\Omega_{\gamma} = 2.469 \cdot 10^{-5} h^{-2}$, and the neutrinos $\Omega_{\nu} = \sum m_{\nu} / \left(94 h^2 \text{eV}\right) \leq 0.00713 h^{-2}$ with the limit on the sum of the mass of all neutrinos species $\sum m_{\nu} \leq 0.67 \text{eV}$. Other fundamental

parameters are the Hubble parameter $H_0 = 100h\,\mathrm{km}\cdot\mathrm{s}^{-1}\cdot\mathrm{Mpc}^{-1}$ $= 70.5 \pm 1.3\,\mathrm{km}\cdot\mathrm{s}^{-1}\cdot\mathrm{Mpc}^{-1}$, the age of the universe $t_0 = (13.72 \pm 0.12)\cdot 10^9\,\mathrm{yr}$, and the effective number of neutrino species $N_{eff} = 4.4 \pm 1.5$ (which allows our current model of three neutrino species). These values where derived from five years of data of the WMAP mission combined with data from other sources.[15] The quoted relative densities $\Omega_i$ are defined as the ratios between the present mass density $\rho_i$ of a particular species *i* and the critical mass density $\rho_{critical} = \frac{3H_0^2}{8\pi G}$. The present density values allow a total density of $\Omega = \sum \Omega_i = 1$, which gives a flat universe. A flat universe that contains dark energy (coming from a positive cosmological constant) will expand forever, and the expansion is accelerating (see Figure 5). The dark matter density of 0.23 means that more than 80% of the matter content of the universe is "invisible" – or even worse: "unknown".

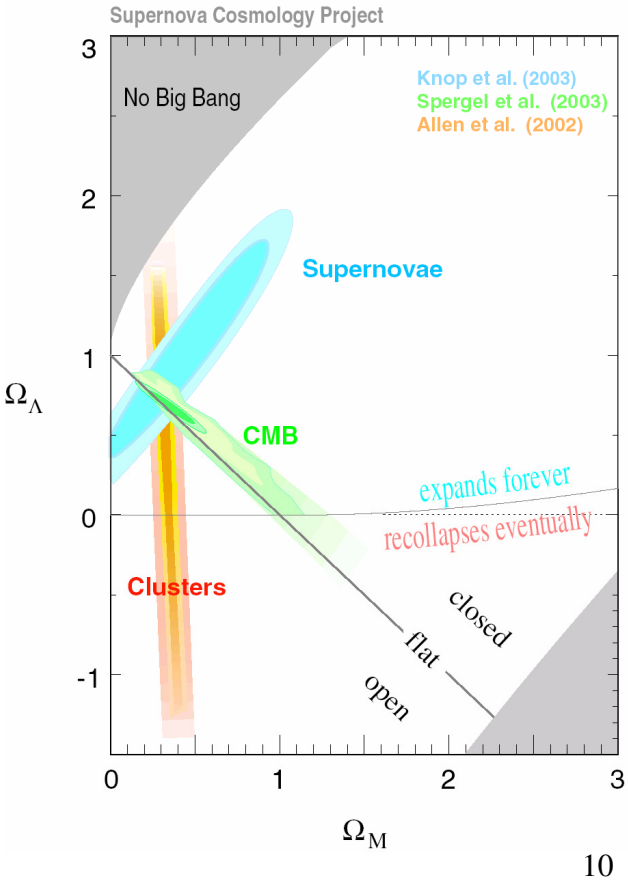


*Figure 5 Confidence regions for $\Omega_M$ vs $\Omega_\Lambda$* [16]
This diagram shows the confidence regions of the relative matter and dark energy densities of our universe obtained from the data of the cosmic microwave background (blue), galaxy clusters (red) and supernova measurements (green). The overlapping region points to dark energy density of about 0.7 and a matter density of about 0.3. This makes it likely, that the total energy density of our universe is exactly 1, which would result in a spatially flat universe. The presence of a (positive) dark energy density in this flat universe causes the universe to expand forever, with an accelerating expansion rate.

There are other arguments in favor of the existence of non-baryonic dark matter: The analysis of the abundance of light elements in the universe (using the model of the big-bang nucleosynthesis) leads only to a value of $0.017 \leq \Omega_{\text{baryons}} h^2 \leq 0.024$.[17] This value is consistent with the WMAP data. Also, there have not been any indications of a large number of objects consisting of invisible baryonic matter such as brown dwarfs, neutron stars, planets, etc.

Even without the findings of the WMAP group, one can show that dark matter cannot be made up of neutrinos either (at least not neutrinos alone), since they are fermions and have to obey Pauli's principle. This limits the number of neutrinos per phase-space volume.[18,19,20] In order to explain the large amount of dark matter despite the limitation of the number density of the neutrinos, neutrinos need to have a high mass. The required mass would be inconsistent with current experimental results and their relic density would exceed the cosmological bound on the neutrinos $\Omega_\nu = \sum m_\nu / \left(94 h^2 \text{eV}\right)$,[15,21] which should be smaller than 1. It should be mentioned that this formula is valid only for neutrinos which decoupled when they were relativistic. If this was not the case, there is a second threshold for neutrino masses which starts at about 2GeV or 5GeV (depending on whether one has Dirac or Majorana neutrinos). Above this value, neutrinos are again cosmologically allowed,[21] i.e. their relic density is smaller than 1. Such neutrinos could be for example sterile neutrinos (see appendix I), but no evidence for their existence has been found, yet.

There is another fact that needs to be considered. Since neutrinos were relativistic when they decoupled, they could only contribute to the so-called "hot" dark matter. However, hot dark matter was most likely not able to form the present-day structures in the universe.[22] The formation of the structure of the universe seems to be explained much better by "cold" (i.e. non-relativistic) dark matter.

An important property which these dark matter particles have to satisfy is that they have to be stable (or at least long living) in order to be responsible for the structure formation. They also cannot be subject to the strong interaction; otherwise they would show up in ordinary matter producing anomalous heavy isotopes.[23] They cannot interact via the electromagnetic force either, since reactions with photons would make them visible, hence it would not be dark matter anymore. Strong and/or electromagnetic interactions between dark matter and ordinary matter would have led to a tighter coupling of these particles to the photon-electron-baryon mixture in the early universe. In this case, the structure formation in the universe would have been different, and it would be inconsistent with the observations from the cosmic microwave background.[24] Another interesting argument against strongly interacting dark matter particles is their rate of heat production if they annihilated in the Earth's core. A dark matter particle that interacts strongly with ordinary matter has a higher scattering cross-section, and therefore a higher capture rate, and finally a higher annihilation rate. This would lead to a much higher heating rate than the observed value.[25] Note, that this does not rule out the possibility that the dark matter particle interacts strongly with itself. If dark matter does not interact strongly and electromagnetically, the only remaining interactions are the weak (and

gravitational interaction). A generic name for such a particle is “weakly interacting massive particle” (WIMP).

Since there are no Standard Model particles (except sterile neutrinos if one extends the Standard Model in this direction) which satisfy the requirements for the dark matter particle (stable, massive, not strongly / electromagnetically interacting), one has to look for particles proposed by theories beyond the Standard Model. Such a theory is supersymmetry (see chapter 3). Supersymmetry proposes the existence of a so-called LSP (the lightest supersymmetric particle) which would meet the requirements to be a dark matter particle. There are three LSP candidates: the sneutrino, the gravitino (the superpartner of the graviton, a particle which needs to be introduced in local supersymmetric theory) and the lightest of the four neutralinos. The sneutrino is excluded by LEP and direct search experiments,[23,26] however certain extended models (e.g. models with lepton number violations) allow the possibility for the sneutrino to be the LSP.[26,27] The gravitino is not ruled out yet.[28] Besides the mentioned supersymmetric particles and sterile neutrinos, there are dark matter candidates such as axions, Kaluza-Klein states, etc. The neutralino is the particle that will be discussed here. In the remaining chapters, the hypothesis is that the dark matter particle is the lightest neutralino.

## 2.2 Relic abundance of the neutralinos

In this section, a calculation is presented that shows that the relic abundance of the hypothesized neutralinos can indeed be responsible for the dark matter content in the universe. Their existence is assumed from here on.

In the early universe, neutralinos were originally in thermal equilibrium with the rest of the universe. The coupling of the neutralinos $\chi$ to ordinary particles was provided through pair-production from (and annihilation to) other particles $\psi$: $\chi\overline{\chi} \leftrightarrow \psi\overline{\psi}$. This equilibrium obviously depends on the annihilation/creation rate $\Gamma$, but the expansion rate of the universe, the Hubble parameter $H$ is crucial as well.

The annihilation rate for neutralinos is

(1) $$\Gamma = \langle \sigma_A v \rangle n ,$$

where $n$ is the number density of the neutralinos, and $\langle \sigma_A v \rangle$ is the average annihilation cross-section for neutralinos. Since the neutralinos are treated as a candidate for the "cold" dark matter, one can use the non-relativistic approximation of the number density[29,30]

(2) $$n = g\left(\frac{mT}{2\pi}\right)^{\frac{3}{2}} \exp\left(-\frac{m}{T}\right)$$

As long as the annihilation/creation rate of neutralinos was bigger than the expansion rate, the neutralinos were kept in equilibrium. However, as the universe became older, the temperature dropped and the number density decreased, so that the annihilation rate

decreased as well. Eventually the annihilation rate became smaller than the expansion rate, which is approximately the point where the neutralinos decouple from the rest of the universe.

(3) $$H \approx \Gamma$$

This can be imagined as the point in time, when the neutralinos were spread so thin that it became improbable for them to find an annihilation partner. Also, the temperature of the universe was already low enough to prevent further pair-creation of neutralinos.

After annihilation stopped, the number of neutralinos stayed approximately constant – there number density per co-moving volume "froze in". In order to estimate the abundance of neutralinos in the universe, one needs to solve equation (3). The annihilation rate is given by (1). The Hubble parameter can be expressed in terms of the total energy density (assuming negligible contributions from the curvature and cosmological constant in the early universe):

(4) $$H = \sqrt{\tfrac{8}{3}\pi G\rho}$$

The freeze-in happened at a time when the early universe was still radiation dominated, and the majority of the particles was relativistic. The energy densities for fermions and bosons are[30]

(5) $$\rho = \begin{cases} \frac{\pi^2}{30} gT^4 & \text{bosons} \\ \frac{7}{8}\frac{\pi^2}{30} gT^4 & \text{fermions} \end{cases}$$

The non-relativistic components can be ignored, since their energy densities are much smaller than the number densities of relativistic particles ( $\rho = g\left(\frac{mT}{2\pi}\right)^{3/2} e^{-m/T}$ )[30]. The total energy density at the radiation dominated universe is therefore

(6) $$\rho = \sum_{i=bosons} \tfrac{\pi^2}{30} g_i T_i^4 + \tfrac{7}{8} \sum_{i=fermions} \tfrac{\pi^2}{30} g_i T_i^4 \text{ , or}$$

(7) $$\rho = \tfrac{\pi^2}{30} g_{eff} T^4 ,$$

with the effective number of degrees of freedom[30]

(8) $$g_{eff} = \sum_{i=bosons} g_i \left(\tfrac{T_i}{T}\right)^4 + \tfrac{7}{8} \sum_{i=fermions} g_i \left(\tfrac{T_i}{T}\right)^4 .$$

The factor $\frac{T_i}{T}$ is necessary, since there were some particles which were not in good thermal contact with the rest of the universe anymore (e.g. decouples, "frozen-out"), so that they had a different temperature than $T$. Note that $g_{eff}$ decreases with lower temperatures (as the universe became older), since more and more particles became non-relativistic, and only the relativistic particles are considered.

Equation (4) can now be written as

(9) $$H = \sqrt{\frac{8\pi G}{3} \frac{\pi^2}{30} g_{eff}}\, T^2 ,$$

or with the gravitation constant replaced by the Planck mass $G = m_{Planck}^{-2} = 1.2 \cdot 10^{19}\,\text{GeV}$

(10) $$H = 1.66 \sqrt{g_{eff}}\, \frac{T^2}{m_{Planck}} ,$$

as it is usually written in the literature.[29,30] The freeze-out temperature can now be estimated from the freeze-out condition (3).

(11) $$1.66 \sqrt{g_{eff}}\, \frac{T^2}{m_{Planck}} = \langle \sigma_A v \rangle g \left(\frac{mT}{2\pi}\right)^{\frac{3}{2}} \exp\left(-\frac{m}{T}\right)$$

An example calculation for a neutralinos mass of $m = 100\text{GeV}$ (for an estimated weak-scale annihilation cross-section[29] $\langle \sigma_A v \rangle = 10^{-8}\,\text{GeV}^{-2}$ and an effective number of degrees

of freedom[29] $g_{eff} = 100$ for the early universe) gives a freeze-out temperature of about 4GeV. In general, freeze-out temperatures are around values of $T = m/20$.[29]

With the known freeze-out temperature, one can estimate the current relic abundance of the neutralinos. Since the universe has expanded from the time of freeze-out until today, the number density $n$ decreased. The easiest way to get around this problem is the use of the entropy density

(12) $$s = \frac{2\pi^2}{45} g_{eff,s} T^3$$

with

(13) $$g_{eff,s} = \sum_{i=bosons} g_i \left(\frac{T_i}{T}\right)^3 + \frac{7}{8} \sum_{i=fermions} g_i \left(\frac{T_i}{T}\right)^3 .$$

similar to the effective number of degrees of freedom for the energy density. The advantage of using the entropy is that $S = sR^3$ (the entropy per co-moving volume $R^3$) stays constant. Also, $N = nR^3$ (the number of neutralinos per co-moving volume) stays constant as well, since the neutralinos stopped annihilating and new neutralinos are not created anymore. This means that $N = n/s = const.$ and has the same value at freeze-out and today. Going back to the example above, one can use again $g_{eff,s} \approx g_{eff} = 100$ at the freeze-out of 4GeV, and today's value for the entropy density $s_0 = 4000\text{cm}^{-3}$,[29] which leads to today's neutralino number density

(14) $$n_0 = n\frac{s_0}{s} = g\left(\frac{mT}{2\pi}\right)^{\frac{3}{2}} \exp\left(-\frac{m}{T}\right) \cdot \frac{4000\text{cm}^{-3}}{\frac{2\pi^2}{45} g_{eff,s} T^3} = 2 \cdot 10^{-8}\,\text{cm}^{-3} .$$

and finally

(15) $$\Omega_0 = \frac{\rho_0}{\rho_{critical,0}} = \frac{m \cdot n_0}{5 \cdot 10^{-6}\,\mathrm{GeV} \cdot \mathrm{cm}^{-3}} = \frac{100\mathrm{GeV} \cdot 2 \cdot 10^{-8}\,\mathrm{cm}^{-3}}{5 \cdot 10^{-6}\,\mathrm{GeV} \cdot \mathrm{cm}^{-3}} = 0.4\,,$$

where $\rho_0 = mn_0$ is today's neutralino energy density of the universe, and $\rho_{critically,0} = \frac{3H_0^2}{8\pi G}$ is today's critical density for a flat universe. The exact value of the result in (15) is not important since it is just an estimate. However, the order of magnitude shows that such a particle could be responsible for a large fraction of the universe's energy content, and could indeed be the dark matter particle.[29]

A more accurate result can be obtained with the help of the Boltzmann equation

(16) $$\frac{dn}{dt} + 3nH = -\langle \sigma_A v \rangle \left( n^2 - n_{equilibrium}^2 \right)$$

where $n_{equilibrium}$ is the equilibrium neutralino density as shown in (2), and $n$ is the actual neutralino density. This differential equation has been solved in several publications.[31] Figure 6 shows some numerical solutions to the Boltzmann equation.

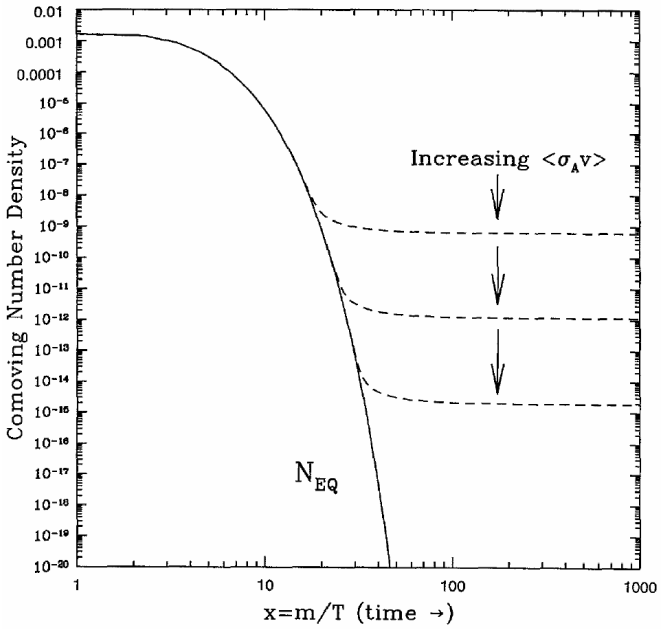


*Figure 6 Comoving number density of a WIMP in the early universe*[29]
solid line: equilibrium number density
dashed lines: actual number density
For higher velocity-averaged annihilation cross-sections $\langle \sigma_A v \rangle$, the freeze-out temperature becomes lower, and the relic abundance of the WIMPs becomes smaller.

Figure 6 shows that initially (at higher temperatures) the neutralino density follows the equilibrium density of equation (2). Eventually the neutralino density breaks away from the equilibrium density during the process of freeze-out. The exact point depends on the annihilation cross-section. Higher annihilation cross-sections lead to lower freeze-out temperatures, which lead to smaller neutralino relic abundances (since the equilibrium density is smaller for lower temperatures). The diagram also shows that the number of neutralinos per co-moving volume stays constant after freeze-out.

# Chapter 3: Particle Physics Motivation

In the previous chapter, cosmological motivations for the existence of a new type of particle were discussed. The question is, whether there are any theories – from the particle physics point of view – which may predict the existence of such particles. It turns out that there is indeed such a theory: supersymmetry. This chapter gives a brief overview of the idea behind supersymmetry. It starts by giving a short explanation of why there may be a need for supersymmetry. The chapter continues with an introduction of the Wess-Zumino model, which explains the basic concept of supersymmetry. The next chapters are dedicated to the development of a realistic supersymmetric model. Two fundamental so-called supermultiplets are introduced: the scalar supermultiplet and the vector supermultiplet. They are used to extend the Standard Model to the Minimal Supersymmetric Standard Model. The last section focuses on one particular sub-category of particles predicted in this new theory: the neutralino. As already mentioned, the lightest neutralino is a perfect candidate to make up the dark matter, and it is the particle which is searched for (in this thesis) with AMANDA.

## 3.1 Why do we need supersymmetry?

The Standard Model provides a highly accurate description of the observations made to date of elementary particles and their interactions. With the construction of new experiments, the only missing particle – the Higgs boson – is believed to be within the

grasp of measurement. Why then should theorists pursue an extended model, if the existing model works so well?

The problem with the Standard Model arises more from the theory than from the experiment. Taking a closer look at the theory, one will find that there is an inconsistency with the Higgs boson. Historically, the Higgs boson was introduced to allow particles of the Standard Model to have mass. A massive spin-1 field as carrier of the weak interaction does not produce a renormalizable theory.[32] Therefore one starts with intrinsically massless spin-1 fields and generates mass using the Higgs mechanism. This leads to a new problem: The Higgs acquires a mass, which diverges quadraticly for higher order loop corrections. The physical mass is in first order

(17) $$m^2_{H,physical} = m^2_{H,0} + \delta m^2_H ,$$

where $\delta m^2_H \sim \Lambda^2$.[33] $\Lambda$ is the cutoff momentum which is introduced to prevent the loop correction integrals to become infinite; $m_{H,0}$ is the bare mass. Since only the physical mass can be measured, the magnitude of the cutoff and the bare mass is in general irrelevant. In order to "achieve" this physical mass, $m_{H,0}$ has to compensate each change in $\Lambda$. This works very well for natural masses, i.e. masses that have either no divergence or only logarithmic divergences, where the mass depends only weakly on the chosen cutoff. The Higgs, however, diverges quadraticly. Its mass depends very strongly on the cutoff.

The cutoff momentum, up to which the loop corrections are taken into account, is the value where the Standard Model ceases to be an accurate description, because yet

unknown processes (which may remove the divergences "automatically") start playing a significant role. If one sets $\Lambda$ to e.g. GUT scale order ($10^{16}$ GeV), and uses an estimated Higgs mass of order of 100 GeV, $m^2_{H,physical}$ at the left-hand side of (17) becomes about 28 orders of magnitude smaller than $\delta m_H^2$.[33,34] This requires a very precise fine-tuning of $m_{H,0}$, which is considered to be un-natural. The situation worsens when higher orders of loop corrections are taken into account, since for every order of corrections an even more precise fine-tuning has to be done.

Of course, one can set the cutoff at a scale where the "fine-tuning problem" does not play a role, which could be at $\Lambda \leq 1\text{TeV}$.[33] This would mean that the Standard Model is valid only up to about 1TeV, and that there must be some kind of "new physics" which cannot be ignored anymore above this value. One candidate of such a new physics – which would take care of the divergences – is supersymmetry,[33] a symmetry which relates particles with different spin to each other, i.e. fermions and bosons.

Another problem arises from grand unified theories: They suggest that the coupling constants of the strong, weak and electromagnetic interactions would match at a certain energy. However, the Standard Model by itself does not allow for these coupling constants to meet at any point.[35] Supersymmetry provides a solution by introducing new particles which contribute to the interactions. This enables the coupling constants to converge at an energy of about $10^{16}$ GeV. [35,36,37] Even though this phenomenon is not going to be discussed further, it can be seen as another strong motivation for supersymmetry.

## 3.2 The Wess-Zumino model

The best way to introduce supersymmetry is to use the Wess-Zumino model, introduced by Julius Wess and Bruno Zumino in 1974.

Consider a multiplet consisting of a left-handed Weyl spinor field $\xi$, a scalar field $\phi$ and an auxiliary (scalar) field $F$.[38] With these particles one can construct a Lagrangian with a kinetic term, an interaction term and a mass term:

(18) $$\mathcal{L} = \mathcal{L}_{free} + \mathcal{L}_{int} + \mathcal{L}_{mass}$$

with the following terms

(19) $$\mathcal{L}_{free} = -\partial^{\mu}\phi^{*}\partial_{\mu}\phi - i\xi^{\dagger}\bar{\sigma}^{\mu}\partial_{\mu}\xi + F^{*}F\,,$$

(20) $$\mathcal{L}_{int} = -y\left[\tfrac{1}{2}\phi\xi\xi + \tfrac{1}{2}\phi^{*}\xi^{\dagger}\xi^{\dagger} - \tfrac{1}{2}\phi\phi F - \tfrac{1}{2}\phi^{*}\phi^{*}F^{*}\right].$$

(21) $$\mathcal{L}_{mass} = -m\left[\tfrac{1}{2}\xi\xi + \tfrac{1}{2}\xi^{\dagger}\xi^{\dagger} - \phi F - \phi^{*}F^{*}\right].$$

The last line includes an explicit mass term for the scalar and a Majorana mass term for the fermion. Note, that the fermion mass terms of the Standard Model are Dirac mass terms (with perhaps the exception of the right-handed neutrino which could have additionally a Majorana mass term – see appendix I). However, fermions with Majorana mass terms will be needed in the chapter about the Minimal Supersymmetric Standard Model. Also, all fields of the Standard Model obtain their mass through their interaction with the Higgs field – they do not have such explicit mass terms. The only exception is the Higgs field itself (therefore it is a useful example indeed).

The idea behind supersymmetry is that both types of particles – bosons and fermions – are governed by the same underlying physical principles. This implies that one can take a particular theory (in this case the Wess-Zumino model) and rotate the above introduced multiplet ($\xi$, $\phi$, $F$) in such a way that one gets a new linear combination of scalars and fermions without changing the physics described by the Lagrangian (18). This is realized for the Wess-Zumino model by the following transformation:

$$
\begin{array}{ll}
\delta\phi = \varepsilon\xi & \delta\phi^* = \varepsilon^\dagger\xi^\dagger \\
\delta(\xi)_\alpha = i\left(\sigma^\mu\varepsilon^\dagger\right)_\alpha\partial_\mu\phi + \varepsilon_\alpha F & \delta\left(\xi^\dagger\right)_{\dot\alpha} = -i\left(\varepsilon\sigma^\mu\right)_{\dot\alpha}\partial_\mu\phi^* + \left(\varepsilon^\dagger\right)_{\dot\alpha}F^* \\
\delta F = i\varepsilon^\dagger\bar\sigma^\mu\partial_\mu\xi & \delta F^* = -i\partial_\mu\xi^\dagger\bar\sigma^\mu\varepsilon
\end{array}
\tag{22}
$$

The total Lagrangian (18) changes under the transformation (22) only by a total derivative, so that the action and the equation of motions remain unchanged (see appendix C).[38] This ensures that the requirement of the unchanged physics is satisfied.

The auxiliary field $F$ does not have kinetic terms in the Lagrangian, and can be replaced in terms of $\xi$ and $\phi$ to get a Lagrangian that does not use the auxiliary field explicitely.[39] Applying the Euler-Lagrange equations to the total Lagrangian (18) with respect to the auxiliary field $F$ (and $F^*$) gives the following equations of motion:

$$
F^* + m\phi + \tfrac{1}{2}y\phi\phi = 0 \text{ and } F + m\phi^* + \tfrac{1}{2}y\phi^*\phi^* = 0 \tag{23}
$$

This result can be used to eliminate *F* from the Lagrangian (18) (see appendix D) to get a new Lagrangian which does not contain the auxiliary fields anymore:

$$
\begin{aligned}
\mathsf{L} = {} & -\partial^\mu\phi^*\partial_\mu\phi - i\xi^\dagger\bar\sigma^\mu\partial_\mu\xi - m\left[\tfrac{1}{2}\xi\xi + \tfrac{1}{2}\xi^\dagger\xi^\dagger\right] - y\left[\tfrac{1}{2}\phi\xi\xi + \tfrac{1}{2}\phi^*\xi^\dagger\xi^\dagger\right] \\
& - m^2\phi\phi^* - \tfrac{1}{2}my\phi\phi^*\phi^* - \tfrac{1}{2}my\phi\phi\phi^* - \tfrac{1}{4}y^2\phi\phi\phi^*\phi^*
\end{aligned}
\tag{24}
$$

The new transformation rules are

$$
\begin{aligned}
&\delta\phi = \varepsilon\xi \\
&\delta(\xi)_\alpha = i\left(\sigma^\mu \varepsilon^\dagger\right)_\alpha \partial_\mu \phi - \varepsilon_\alpha\left(m\phi^* + \tfrac{1}{2}\, y\phi^*\phi^*\right) \\
&\delta\phi^* = \varepsilon^\dagger \xi^\dagger \\
&\delta\left(\xi^\dagger\right)_{\dot\alpha} = -i\left(\varepsilon\sigma^\mu\right)_{\dot\alpha} \partial_\mu \phi^* - \left(\varepsilon^\dagger\right)_{\dot\alpha}\left(m\phi + \tfrac{1}{2}\, y\phi\phi\right)
\end{aligned}
\tag{25}
$$

One might ask why the auxiliary fields were introduced in the first place. First of all, the auxiliary fields are necessary to give a mathematical complete description of supersymmetry.[40,41,42] Also, using the equation of motions (which are derived from the *entire* Lagrangian) to replace the auxiliary fields makes the new SUSY transformation rules dependent on the *entire* Lagrangian. This would mean that such transformations are not model independent anymore (e.g. different interaction terms lead to different transformation rules). The mathematical formalism which gives the SUSY transformation rules along with the auxiliary fields is called superspace. A discussion of this topic is beyond the scope of this review, but can be found in many publications.[40,41,42]

The Lagrangian (24) describes the interaction of a scalar field $\phi$ and a left-handed Weyl spinor field $\xi$. The Lagrangian includes only one mass parameter *m* and only one coupling constant *y*. It is worth showing with an example that this model really removes the quadratic divergences, which was one of the reasons to construct this theory. First, the Weyl spinor fields are converted into four-component spinor fields since this is the "standard form" for which the Feynman rules are usually applied to, and the components of the complex scalar are treated as two separate particles (see appendix E):

$$
\begin{aligned}
\mathsf{L} = &-\tfrac{1}{2}\partial^\mu A \partial_\mu A - \tfrac{1}{2}\partial^\mu B \partial_\mu B - \tfrac{1}{2} i\,\overline{\psi}_M \gamma^\mu \partial_\mu \psi_M - \tfrac{1}{2} m\,\overline{\psi}_M \psi_M - \tfrac{1}{2\sqrt{2}}\, y\left[A\,\overline{\psi}_M \psi_M - iB\,\overline{\psi}_M \gamma^5 \psi_M\right] \\
&- \tfrac{1}{2} m^2\left(A^2 + B^2\right) - \tfrac{1}{2\sqrt{2}} my\left[A^3 + AB^2\right] - \tfrac{1}{16}\, y^2\left(A^4 + 2A^2B^2 + B^4\right)
\end{aligned}
\tag{26}
$$

In the following, all possible one-loop corrections to the A part of the scalar given by the Lagrangian (26) are shown in Table 1:[43,44,45]

| | |
|---|---|
| 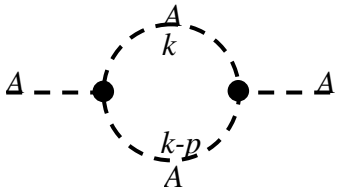  | $-iM_{(1)} = 3\cdot 3\cdot 2!\left(-\frac{imy}{2\sqrt{2}}\right)\cdot\left(-\frac{imy}{2\sqrt{2}}\right)\cdot\int d^4k\,\frac{i^2}{\left[k^2-m^2\right]\cdot\left[(k-p)^2-m^2\right]}$ |
| 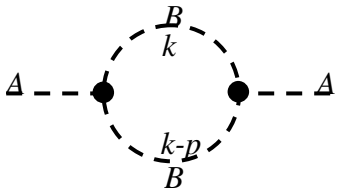  | $-iM_{(2)} = 2!\left(-\frac{imy}{2\sqrt{2}}\right)\cdot\left(-\frac{imy}{2\sqrt{2}}\right)\cdot\int d^4k\,\frac{i^2}{\left[k^2-m^2\right]\cdot\left[(k-p)^2-m^2\right]}$ |
| 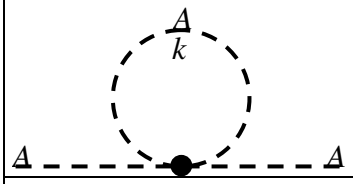  | $-iM_{(3)} = 4\cdot 3\cdot\frac{-iy^2}{16}\cdot\int d^4k\,\frac{i}{\left[k^2-m^2\right]}$ |
| 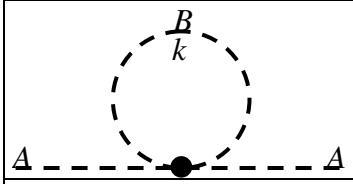  | $-iM_{(4)} = 2\cdot\frac{-iy^2}{8}\cdot\int d^4k\,\frac{i}{\left[k^2-m^2\right]}$ |
| 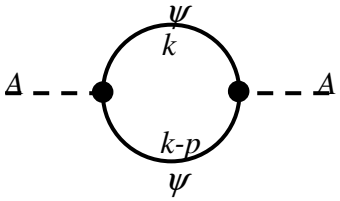  | $-iM_{(5)} = (-1)\cdot 2!\frac{-iy}{2\sqrt{2}}\cdot\frac{-iy}{2\sqrt{2}}\cdot\int d^4k\cdot\mathrm{Tr}\left[\frac{i}{\not k - m}\frac{i}{(\not k - \not p)-m}\right]$ The factor 2! is necessary since the fields connected to the vertices are Majorana fields where $\overline{\psi}_M = \psi_M^T C$ so that both vertices have actually two identically $\psi$,[46] as illustrated in the diagram. |

*Table 1 First order loop corrections to a scalar from the Lagrangian of the Wess-Zumino model*

$M_{(1)}$ and $M_{(2)}$ are only logarithmic divergent, so one does not have to care about them.

The remaining two diagrams lead to[43]

(27)

$$
\begin{aligned}
-iM_{(3)(4)(5)} &= \frac{12}{16} y^2 \int d^4k \frac{1}{k^2-m^2} + \frac{2}{8} y^2 \int d^4k \frac{1}{k^2-m^2} - \frac{1}{4} y^2 \int d^4k \cdot \mathrm{Tr} \frac{[\not k + m] \cdot [(\not k - \not p) + m]}{[k^2-m^2] \cdot [(k-p)^2 - m^2]} \\
&= y^2 \int d^4k \frac{1}{k^2-m^2} - \frac{1}{4} y^2 \int d^4k \frac{\mathrm{Tr}[\not k \not k - \not k \not p + 2 \not k m - \not p m + m^2]}{[k^2-m^2] \cdot [(k-p)^2 - m^2]} \\
&= y^2 \int d^4k \frac{1}{k^2-m^2} - \frac{1}{4} y^2 \int d^4k \frac{4k^2 - 4kp + 4m^2}{[k^2-m^2] \cdot [(k-p)^2 - m^2]} \\
&= y^2 \int d^4k \frac{1}{k^2-m^2} - \frac{1}{4} y^2 \int d^4k \frac{2[(k^2-m^2) + ((k-p)^2 - m^2) - p^2 + 4m^2]}{[k^2-m^2] \cdot [(k-p)^2 - m^2]} \\
&= y^2 \int d^4k \frac{1}{k^2-m^2} - \frac{1}{2} y^2 \int d^4k \left[ \frac{1}{(k-p)^2-m^2} + \frac{1}{k^2-m^2} + \frac{4m^2 - p^2}{[k^2-m^2] \cdot [(k-p)^2 - m^2]} \right]
\end{aligned}
$$

where the last term of the second integral is again only logarithmic divergent. The other parts cancel (using a change of variables for the first term of the second integral $k \to k' = k + p$ ), so that there are no quadratic divergences anymore:[43]

(28)

$$
\begin{aligned}
-iM_{(3)(4)(5)} &= y^2 \int d^4k \frac{1}{k^2-m^2} - \frac{1}{2} y^2 \int d^4k \cdot \frac{1}{(k-p)^2-m^2} - \frac{1}{2} y^2 \int d^4k \cdot \frac{1}{k^2-m^2} \\
&= y^2 \int d^4k \frac{1}{k^2-m^2} - \frac{1}{2} y^2 \int d^4k' \cdot \frac{1}{k'^2-m^2} - \frac{1}{2} y^2 \int d^4k \cdot \frac{1}{k^2-m^2} \\
&= 0
\end{aligned}
$$

The contributions of both the fermion and the two bosons are the reason that there is no more quadratic divergence anymore in the loop correction of the A part of the boson. The same can be shown for the B part of the boson (see appendix F).

From the last step one could get the impression that the fermion and boson masses have to be exactly equal to remove the quadratic divergences. If this would be the case, supersymmetric particles should have been discovered by now, since their masses would be in the range of our known Standard Model masses – e.g. there should be a scalar with

the same mass as the electron. Since this is not the case, supersymmetry must be broken (if one considers supersymmetry to be valid at all). A closer look shows that it is possible that the fermion and boson mass differs by a small amount without the reoccurrence of quadratic divergences. This kind of supersymmetry breaking is called soft supersymmetry breaking. For instance, changing the boson mass by adding a term like

$$\mathsf{L}_{soft} = -m'^2\phi^*\phi = -\tfrac{1}{2}m'^2\left(A^2 + B^2\right) \tag{29}$$

to the Lagrangian (26) would only add additional logarithmic divergent terms to $M_{(3)}$ and $M_{(4)}$, but no quadratic divergences:[47]

$$\int d^4k \frac{1}{k^2 - (m+m')^2} = \int d^4k \frac{1}{k^2 - m^2 - 2mm' - m'^2} = \int d^4k \left( \frac{1}{k^2 - m^2} + \frac{2mm'}{\left(k^2 - m^2\right)^2} + \frac{k^2 m'^2 + 3m^2 m'^2}{\left(k^2 - m^2\right)^3} + \ldots \right)$$

.

The quadratic divergent term was cancelled by $M_{(5)}$.

There are other soft supersymmetry breaking terms which can be added to the Lagrangian. They will be introduced in the section 3.4.

## 3.3 Supermultiplets

The model, which has been used to introduce supersymmetry, is of course only one example of a supersymmetric theory. In general, supersymmetry relates a particle to a superpartner of equal mass and charge (and other quantum numbers), but only differs by its spin. The particles and its superpartners are related to each other through a supersymmetry transformation. Both particles form a supermultiplet.

For the remaining chapters, two supermultiplets are of interest: the scalar supermultiplet and the vector supermultiplet.

The first one – the left-handed scalar supermultiplet – has been introduced already in the last chapter. It contains a Weyl spinor, a scalar field and a scalar auxiliary field. The SUSY transformation rules and the Lagrangian were shown in (22) and (18). It was possible to eliminate the auxiliary fields by satisfying their equations of motion. This led to the Lagrangian (24).

It is convenient to use the so-called superpotentials $W$ for further calculations, especially when one includes more than one scalar supermultiplet. This changes the Lagrangian (24) into[48]

(30) $$\mathsf{L} = -\partial^\mu \phi^{*i} \partial_\mu \phi_i - i\xi^{\dagger i} \bar{\sigma}^\mu \partial_\mu \xi_i - \tfrac{1}{2}\left(W^{ij}\xi_i\xi_j + W^{*ij}\xi^{\dagger i}\xi^{\dagger j}\right) - W^i W_i^* ,$$

where the sum has to be taken over the different supermultiplets, which are labeled by the indices $i$ and $j$. The symbols $W^i$ and $W^{ij}$ are defined as $W^i = \frac{\partial W}{\partial \phi_i}$ and $W^{ij} = \frac{\partial^2 W}{\partial \phi_i \partial \phi_j}$. An example for a superpotential is

(31) $$W = \tfrac{1}{2} m^{ij} \phi_i \phi_j + \tfrac{1}{6} y^{ijk} \phi_i \phi_j \phi_k ,$$

where one has again a sum over all supermultiplets *i*, *j*, and *k*. If one uses a superpotential consisting of only one supermultiplet (e.g. $W = \frac{1}{2} m\phi\phi + \frac{1}{6} y\phi\phi\phi$ ), one would get back the Lagrangian (24) (see appendix G). An important feature is that the superpotential cannot contain the complex conjugate of the scalar field $\phi^*$, only the scalar field $\phi$ itself; otherwise the Lagrangian would not be SUSY invariant anymore (see appendix H).[48]

The other type of supermultiplet – the vector supermultiplet – contains the gauge fields $A_\mu^a$ of the Standard Model. The gauge fields can be inserted into the Lagrangian (30) by replacing the ordinary derivatives by gauge-covariant derivatives $D_\mu\phi(x)=\left(\partial_\mu - ig\sum_a A_\mu^a(x)T^a\right)\phi(x)$ and $D_\mu\xi(x)=\left(\partial_\mu - ig\sum_a A_\mu^a(x)T^a\right)\xi(x)$ (see appendix B).

(32) $$\mathcal{L}_{scalar} = -\left(D^\mu\phi^i\right)^* D_\mu\phi_i - i\xi^{\dagger i}\bar{\sigma}^\mu D_\mu\xi_i - \tfrac{1}{2}\left(W^{ij}\xi_i\xi_j + W^{*ij}\xi^{\dagger i}\xi^{\dagger j}\right) - W^i W_i^*$$

The supersymmetric counterpart to the gauge field $A_\mu^a$ (spin 1 vector fields), is the gaugino field $\lambda^a$ (spin ½ spinor fields), which is the second member of the vector supermultiplet. The third member is the scalar auxiliary field $D^a$. The Lagrangian for the vector supermultiplet is[49]

(33) $$\mathcal{L}_{gauge} = -\tfrac{1}{4}F_{\mu\nu}^a F^{a\mu\nu} - i\lambda^{a\dagger}\bar{\sigma}^\mu D_\mu\lambda^a + \tfrac{1}{2}D^a D^a$$

with the gauge-covariant derivative $D_\mu\lambda^a = \partial_\mu\lambda^a - gf^{abc}A_\mu^b\lambda^c$ and the field strength $F_{\mu\nu}^a = \partial_\mu A_\nu^a - \partial_\nu A_\mu^a - gf^{abc}A_\mu^b A_\nu^c$.

The gauge-covariant supersymmetry transformations are[49]

(34) $$\begin{aligned}\delta A_\mu^a &= -\tfrac{1}{\sqrt{2}}\left(\varepsilon^\dagger\bar{\sigma}_\mu\lambda^a + \lambda^{a\dagger}\bar{\sigma}_\mu\varepsilon\right)\\ \delta\left(\lambda^a\right)_\alpha &= -\tfrac{i}{2\sqrt{2}}\left(\sigma^\mu\bar{\sigma}^\nu\varepsilon\right)_\alpha F_{\mu\nu}^a + \tfrac{1}{\sqrt{2}}\varepsilon_\alpha D^a\\ \delta D^a &= \tfrac{i}{\sqrt{2}}\left(\varepsilon^\dagger\bar{\sigma}^\mu D_\mu\lambda^a - D_\mu\lambda^{a\dagger}\bar{\sigma}^\mu\varepsilon\right)\end{aligned}$$

Elements of the vector supermultiplet – the gauge fields $A_\mu^a$ – were already introduced to the scalar supermultiplet via the gauge-covariant derivatives $D_\mu\phi_i$ and $D_\mu\xi_i$. Since these gauge fields transform under the SUSY transformation rules of the vector supermultiplet,

the SUSY transformation rules of the scalar supermultiplet have to be modified to counteract this effect. This is done by adding an additional term to the transformation of the auxiliary field:[49]

$$\begin{aligned} &\delta\phi = \varepsilon\xi \\ &\delta(\xi)_\alpha = i\left(\sigma^\mu \varepsilon^\dagger\right)_\alpha D_\mu \phi + \varepsilon_\alpha F \\ &\delta F = i\varepsilon^\dagger \bar{\sigma}^\mu D_\mu \xi + \sqrt{2} g\left(T^a \phi\right)\varepsilon^\dagger \lambda^{a\dagger} \end{aligned} \tag{35}$$

In order to get interactions between the fields of scalar and vector supermultiplets, one can add the following interaction terms to the Lagrangian:[49]

$$\mathsf{L}_{interaction} = -\sqrt{2} g\left[\left(\phi^{i*} T^a \xi_i\right)\lambda^a + \lambda^{a\dagger}\left(\xi^{i\dagger} T^a \phi_i\right)\right] + g\left(\phi^{i*} T^a \phi_i\right) D^a \tag{36}$$

The total Lagrangian can now be written as

$$\begin{aligned} \mathsf{L}_{total} &= \mathsf{L}_{scalar} + \mathsf{L}_{gauge} + \mathsf{L}_{interaction} = \\ &-\left(D^\mu \phi^i\right)^* D_\mu \phi_i - i\xi^{\dagger i} \bar{\sigma}^\mu D_\mu \xi_i - \tfrac{1}{2}\left(W^{ij} \xi_i \xi_j + W^{*ij} \xi^{\dagger i} \xi^{\dagger j}\right) - W^i W_i^* \\ &-\tfrac{1}{4} F^a_{\mu\nu} F^{a\mu\nu} - i\lambda^{a\dagger} \bar{\sigma}^\mu D_\mu \lambda^a + \tfrac{1}{2} D^a D^a \\ &-\sqrt{2} g\left[\left(\phi^{i*} T^a \xi_i\right)\lambda^a + \lambda^{a\dagger}\left(\xi^{i\dagger} T^a \phi_i\right)\right] + g\left(\phi^{i*} T^a \phi_i\right) D^a \end{aligned} \tag{37}$$

It is invariant under gauge and SUSY transformations.

With the help of the Euler-Lagrange equation, on can find the equation of motion for the auxiliary fields $D^a$ is

$$D^a + g\left(\phi^{i*} T^a \phi_i\right) = 0\,, \tag{38}$$

so that it is possible now to eliminate these fields. This leads to the final Lagrangian:[49,50,51]

$$
\begin{aligned}
\mathcal{L}_{total} = & -\left(D^{\mu}\phi^{i}\right)^{*} D_{\mu}\phi_{i} - i\xi^{\dagger i}\bar{\sigma}^{\mu} D_{\mu}\xi_{i} \\
& - \tfrac{1}{4} F^{a}_{\mu\nu} F^{a\mu\nu} - i\lambda^{a\dagger}\bar{\sigma}^{\mu} D_{\mu}\lambda^{a} \\
& - \tfrac{1}{2}\left(W^{ij}\xi_{i}\xi_{j} + W^{*ij}\xi^{\dagger i}\xi^{\dagger j}\right) \\
& - W^{i} W^{*}_{i} \\
& - \sqrt{2} g\left[\left(\phi^{i*} T^{a} \xi_{i}\right)\lambda^{a} + \lambda^{a\dagger}\left(\xi^{i\dagger} T^{a} \phi_{i}\right)\right] \\
& - \tfrac{1}{2}\left[g\left(\phi^{i*} T^{a} \phi_{i}\right)\right]^{2}
\end{aligned}
\tag{39}
$$

The sums run over all involved scalar supermultiplets (index $i$), and over all gauge/gaugino fields and associated generators (index $a$) of the used gauge group. Again, $\phi_i$ and $\xi_i$ are the scalars and Weyl spinors of the scalar supermultiplets, $\lambda^a$ are the Weyl spinors of the vector supermultiplets, $D_\mu$ is the gauge covariant derivative (note that they differ for the scalar and the vector supermultiplet), $F_{\mu\nu}$ is the field strength tensor and $g$ are the coupling constants for each gauge group. Both, $D_\mu$ and $F_{\mu\nu}$ contain the gauge field $A^a_\mu$.

The first line describes the gauge invariant kinetic term of the members of the scalar supermultiplet, which couples the scalars and fermions to the gauge fields. The former leads to the masses of the gauge bosons through $\left(D^{\mu}H\right)^{*} D_{\mu}H$, where $H$ is the Higgs boson (see appendix J).

The second line describes the gauge invariant kinetic term of the members of the vector supermultiplet, which couples the gauge fields to itself and to the gauginos.

The third line describes the Yukawa interaction between scalars and fermions of the scalar supermultiplet and can be used to give masses to the fermions through their interaction with the Higgs boson.

The fourth line describes the interactions of the scalars and can be used to give masses to scalars.

The fifth line describes the interactions of gauginos with the elements of the scalar supermultiplet.

The sixth line describes the interaction of the scalars.

## 3.4 Minimal Supersymmetric Standard Model (MSSM)

As one can see from the discussion of the last section, all Standard Model particles get a supersymmetric partner, which differs by spin ½. This means that the particle spectrum has to be doubled. The name convention for supersymmetric particles is the following: All bosonic partners of Standard Model fermions get the prefix "s-", like selectrons, sneutrinos or squarks for the SUSY partners of electrons, neutrinos and quarks. The fermionic partners of Standard Model bosons get the suffix "-ino", like photinos, gluinos, Higgsinos as the partners of photons, gluons and Higgs. The complete list of the particle content of the MSSM can be found in Table 2 and Table 3.

| | Super-multiplet | Particles | Sparticles | Eigenvalues of ... | | |
|---|---|---|---|---|---|---|
| | | | | $T_2^3 = \frac{1}{2}\sigma^3$ | $T_1 = \frac{1}{2}Y$ | $Q = T_2^3 + T_1$ |
| left-handed quarks/squarks (3 families) | $\hat{Q}_i$ | $Q_i = \begin{pmatrix} u_{iL} \\ d_{iL} \end{pmatrix}$ | $\tilde{Q}_i = \begin{pmatrix} \tilde{u}_{iL} \\ \tilde{d}_{iL} \end{pmatrix}$ | $+\frac{1}{2}$<br>$-\frac{1}{2}$ | $+\frac{1}{6}$ | $+\frac{2}{3}$<br>$-\frac{1}{3}$ |
| right-handed quarks/squarks (3 families) | $\hat{U}_i$ | $U_i = (u_{iR})^C$ | $\tilde{U}_i = (\tilde{u}_{iR})^C$ | 0 | $-\frac{2}{3}$ | $-\frac{2}{3}$ |
| | $\hat{D}_i$ | $D_i = (d_{iR})^C$ | $\tilde{D}_i = (\tilde{d}_{iR})^C$ | 0 | $+\frac{1}{3}$ | $+\frac{1}{3}$ |
| left-handed leptons/sleptons (3 families) | $\hat{L}_i$ | $L_i = \begin{pmatrix} \nu_{iL} \\ e_{iL} \end{pmatrix}$ | $\tilde{L}_i = \begin{pmatrix} \tilde{\nu}_{iL} \\ \tilde{e}_{iL} \end{pmatrix}$ | $+\frac{1}{2}$<br>$-\frac{1}{2}$ | $-\frac{1}{2}$ | 0<br>$-1$ |
| right-handed leptons/sleptons (3 families) | $\hat{E}_i$ | $E_i = (e_{iR})^C$ | $\tilde{E}_i = (\tilde{e}_{iR})^C$ | 0 | $+1$ | $+1$ |
| | $\hat{N}_i$ | $N_i = (\nu_{iR})^C$ | $\tilde{N}_i = (\tilde{\nu}_{iR})^C$ | 0 | 0 | 0 |
| Higgs/Higgsinos | $\hat{H}_1$ | $H_1 = \begin{pmatrix} h_1^+ \\ h_1^0 \end{pmatrix}$ | $\tilde{H}_1 = \begin{pmatrix} \tilde{h}_1^+ \\ \tilde{h}_1^0 \end{pmatrix}$ | $+\frac{1}{2}$<br>$-\frac{1}{2}$ | $+\frac{1}{2}$ | $+1$<br>0 |
| | $\hat{H}_2$ | $H_2 = \begin{pmatrix} h_2^0 \\ h_2^- \end{pmatrix}$ | $\tilde{H}_2 = \begin{pmatrix} \tilde{h}_2^0 \\ \tilde{h}_2^- \end{pmatrix}$ | $+\frac{1}{2}$<br>$-\frac{1}{2}$ | $-\frac{1}{2}$ | 0<br>$-1$ |

*Table 2 Particle content of the scalar supermultiplet*[52]

It is a convention that all fermions of the scalar supermultiplet are defined in terms of left-handed Weyl spinors. Therefore all right-handed fermions are listed as charge conjugated fields, since charge conjugation turns the right-handed $\chi^{\dot{\alpha}\dagger}$ into the left-handed $\chi_\alpha$ (see appendix A).

| | Super-multiplet | Particles | Sparticles |
|---|---|---|---|
| U(1) gauge boson/bino | $\hat{B}$ | $B$ | $\tilde{B}$ |
| $SU(2)_L$ gauge bosons/winos (3 fields) | $\hat{W}^a$ | $W^a$ | $\tilde{W}^a$ |
| SU(3) gluons/gluinos (8 fields) | $\hat{G}^a$ | $G^a$ | $\tilde{G}^a$ |

*Table 3 Particle content of the vector supermultiplet*[52]

In the Standard Model, the leptons and quarks acquire their (Dirac) mass through the coupling with the Higgs boson via

$$\mathsf{L}_{\mathrm{SM}} = y_L^{ij} L_i^{a\dagger} H_a e_{Rj}^\dagger + y_N^{ij} L_i^{a\dagger} H_a^C \nu_{Rj}^\dagger + y_D^{ij} Q_i^{a\dagger} H_a d_{Rj}^\dagger + y_U^{ij} Q_i^{a\dagger} H_a^C u_{Rj}^\dagger + h.c., \tag{40}$$

where $a$ is the weak isospin (SU(2)) index, $i, j$ are family indices and $y^{ij}$ are the Yukawa coupling constants, $L,Q$ are the left-handed lepton and quark SU(2) doublets, $e,\nu,d,u$ are the right-handed lepton and quark SU(2) singlets (all leptons and quarks are written in terms of Weyl spinors). Furthermore, this Lagrangian contains the Higgs SU(2) doublet $H$ with $\langle H \rangle = \begin{pmatrix} 0 & \frac{v}{\sqrt{2}} \end{pmatrix}^T$ which couples to the $T_2^3 = -\frac{1}{2}$ (lower) component of the fermion SU(2) doublets and $H^C = i\sigma^2 H^*$ with $\langle H^C \rangle = \begin{pmatrix} \frac{v}{\sqrt{2}} & 0 \end{pmatrix}^T$ which couples to the $T_2^3 = +\frac{1}{2}$ (upper) component of the fermion SU(2) doublet. Therefore, a superpotential which can do a similar job in the third line of (39) would need to contain the complex conjugated Higgs field $H^*$, which is not SUSY invariant anymore (see appendix H). The solution to this problem is introducing a second Higgs doublet, where the first Higgs $H_1 = \begin{pmatrix} h_1^+ & h_1^0 \end{pmatrix}^T$ with $\langle h_1^0 \rangle = v_1$ gives mass to the $T_2^3 = +\frac{1}{2}$ component and the second Higgs $H_2 = \begin{pmatrix} h_2^0 & h_2^- \end{pmatrix}^T$ with $\langle h_2^0 \rangle = v_2$ gives mass to the $T_2^3 = -\frac{1}{2}$ component of the fermion doublets. Note that one has to pay attention to the symbol $\varepsilon_{12} = 1 = -\varepsilon_{21}$ and $\varepsilon_{11} = \varepsilon_{22} = 0$ in (41).

Now it is possible to write down the superpotential containing the supermultiplets of the MSSM. Possible combinations are: [52,53,54]

$$W = \varepsilon_{ab}\mu H_1^a H_2^b + \varepsilon_{ab}\left[ y_E^{ij} H_1^a \tilde{L}_i^b \tilde{N}_j + y_N^{ij} H_2^a \tilde{L}_i^b \tilde{E}_j + y_D^{ij} H_1^a \tilde{Q}_i^b \tilde{U}_j + y_U^{ij} H_2^a \tilde{Q}_i^b \tilde{D}_j \right] \tag{41}$$

Here $i, j$ represent again the family indices, $a,b$ are the weak isospin indices and $y^{ij}$ are the Yukawa coupling constants (they form a 3×3 matrix in family space); the sum has to be taken over all indices. One could include more terms, but they would violate the

conservation of lepton numbers or baryon numbers. In order to solve this problem a new symmetry is introduced: the R parity. The R parity is defined as[55]

(42) $$R = (-1)^{3B-3L+2S}$$

where $B$ and $L$ are the baryon and lepton number. $S$ denotes the spin. All Standard Model particles have $R$ equal to +1. The sparticles carry an R parity of –1. It is assumed that the MSSM conserves the R parity. This has two important consequences:

There must be a lightest sparticle (LSP), which is stable. It cannot decay into ordinary particles, because this would violate R parity, and it cannot decay into a supersymmetric particle, since it is already the lightest supersymmetric particle. Also, every "decay chain" of SUSY particles will end with and odd number of LSPs in order to keep $R = -1$. Sparticles can only be pair produced ( $R = (-1)^2 = +1$ ) from ordinary particles ( $R = +1$ ), and can only annihilate in pairs.

The theory so far corresponds to an unbroken symmetry. As already mentioned that would mean that there should be supersymmetric particles in nature, which have the same mass as ordinary Standard Model particles. Since this is not the case, one needs to include soft symmetry breaking terms. Following the discussion about soft supersymmetry breaking, one has to add terms to the Lagrangian (39) which allow different masses for the partners of the supermultiplets, but do not reintroduce divergences. The most general soft supersymmetry breaking terms are[56]

(43) $$\mathcal{L}_{soft} = -\tfrac{1}{2}\left(M\lambda^a\lambda^a + h.c.\right) - \left(m^2\right)^i_j \phi^{j*}\phi_i - \left(\tfrac{1}{2}b^{ij}\phi_i\phi_j + h.c.\right) - \left(\tfrac{1}{6}a^{ijk}\phi_i\phi_j\phi_k + h.c.\right).$$

The first term describes a (Majorana) mass term for fermions, the second term is a scalar mass term, and the remaining terms are interaction terms. For the particles of the MSSM one gets[57,58]

$$
\begin{aligned}
\mathcal{L}_{soft} = & -\tfrac{1}{2}\left(M_1\tilde{B}\tilde{B} + M_2\tilde{W}^a\tilde{W}^a + M_3\tilde{G}^a\tilde{G}^a + h.c.\right) \\
& -\left(m_Q^2\right)_i^j \tilde{Q}^{*i}\tilde{Q}_j - \left(m_L^2\right)_i^j \tilde{L}^{*i}\tilde{L}_j - \left(m_U^2\right)_i^j \tilde{U}^{*i}\tilde{U}_j - \left(m_D^2\right)_i^j \tilde{D}^{*i}\tilde{D}_j - \left(m_E^2\right)_i^j \tilde{E}^{*i}\tilde{E}_j \\
& - m_{H_1}^2 H_1^* H_1 - m_{H_2}^2 H_2^* H_2 - \left(bH_1H_2 + h.c.\right) \\
& -\left(a_D^{ij} H_1 \tilde{Q}^i \tilde{D}^j + a_U^{ij} H_2 \tilde{Q}^i \tilde{U}^j + a_E^{ij} H_1 \tilde{L}^i \tilde{E}^j + h.c.\right)
\end{aligned}
\tag{44}
$$

where each of the $a$'s and $m^2$'s matrices are 3×3 complex matrices in family space; $i$ and $j$ are again the family indices. The weak isospin indices have been suppressed.

With equations (41) and (44) a lot of new parameters were introduced. The new supersymmetric Langrangian contains 105 free parameters.[57] However, some of these parameters can already be set to zero or strongly limited in order to be consistent with experimental results, or they can be fixed by certain theoretical assumptions.[62]

## 3.5 Mass eigenstates of the neutralinos

Out of all the supersymmetric particles, the neutralinos are the particles which this analysis is most interested in. The reason is that they are the strongest dark matter candidates (see next chapter). It will be explained in the next chapter that the dark matter particles are the ones which AMANDA is trying to find.

The neutralinos are the supersymmetric partners of the neutral gauge bosons and the neutral Higgs bosons: the bino, the neutral wino and the two neutral Higgsinos. From the soft breaking term (44) we know that $M_1$ and $M_2$ give mass to the binos and winos

$$\mathsf{L} = -\tfrac{1}{2}\left(M_1\tilde{B}\tilde{B} + M_2\tilde{W}^a\tilde{W}^a\right) + h.c. \tag{45}$$

The mass terms involving the two neutral Higgsinos can be found from the superpotential (41), which contains $W = \varepsilon_{ab}\mu H_1^a H_2^b$, with the neutral part $W = \varepsilon_{21}\mu H_1^2 H_2^1 = -\mu h_1^0 h_2^0$. After using the third line of the Lagrangian (39) one gets

$$\begin{aligned}\mathsf{L} &= -\tfrac{1}{2}\left(W^{ij}\tilde{h}_i^0\tilde{h}_j^0\right) + h.c. = -\tfrac{1}{2}\left(\frac{\partial^2 W}{\partial h_1^0 \partial h_2^0}\tilde{h}_1^0\tilde{h}_2^0 + \frac{\partial^2 W}{\partial h_2^0 \partial h_1^0}\tilde{h}_2^0\tilde{h}_1^0\right) + h.c. \\ &= \frac{1}{2}\mu\left(\tilde{h}_1^0\tilde{h}_2^0 + \tilde{h}_2^0\tilde{h}_1^0\right) + h.c.\end{aligned} \tag{46}$$

Furthermore the couplings between the Higgsinos and the gauginos have to be considered. An appropriate term can be found from the fifth line of equation (39). This term contains the information about the interaction between Higgs, Higgsinos and gauginos $\mathsf{L} = -\sqrt{2}g\left[\left(\phi^{i*}T^a\xi_i\right)\lambda^a + \lambda^{a\dagger}\left(\xi^{i\dagger}T^a\phi_i\right)\right]$. The coupling constants are $g_{SU(2)} = g$ and $g_{U(1)} = g'$. While SU(2) has the neutral gaugino $\lambda_2^3 = \tilde{W}^3$ with the group generator $T_2^3 = \frac{1}{2}\sigma^3$, U(1) has the bino $\lambda_1 = \tilde{B}$ with the group generator $T_1 = \frac{1}{2}Y$. These operators can be substituted by their eigenvalues (see Table 2). The eigenvalues for the third component of the weak isospin operator are $T_2^3 h_{1/2}^0 = \pm\frac{1}{2}h_{1/2}^0$ and $T_2^3\tilde{h}_{1/2}^0 = \pm\frac{1}{2}\tilde{h}_{1/2}^0$. The eigenvalues of the hypercharge are $T_1 h_{1/2}^0 = \mp\frac{1}{2}h_{1/2}^0$ and $T_1\tilde{h}_1^0 = \mp\frac{1}{2}\tilde{h}_{1/2}^0$. Furthermore one has to use the vacuum expectation values for the two Higgs bosons $\left\langle h_1^0\right\rangle = v_1$, $\left\langle h_2^0\right\rangle = v_2$. This leads e.g. for the combination $\tilde{h}_1^0$, $\tilde{W}^3$ to the term

(47)

$$\begin{aligned}
\mathsf{L} &= -\sqrt{2}g\left[\left(h_1^{0^*}T_2^3\tilde{h}_1^0\right)\tilde{W}^3 + \tilde{W}^{3^\dagger}\left(\tilde{h}_1^{0^\dagger}T_2^3h_1^0\right)\right] = -\sqrt{2}g\left[\left(\tfrac{1}{2}h_1^{0^*}\tilde{h}_1^0\right)\tilde{W}^3 + \tilde{W}^{3^\dagger}\left(\tfrac{1}{2}\tilde{h}_1^{0^\dagger}h_1^0\right)\right] \\
\langle\mathsf{L}\rangle &= -\sqrt{2}g\left[\left(\tfrac{1}{2}v_1\tilde{h}_1^0\right)\tilde{W}^3 + \tilde{W}^{3^\dagger}\left(\tfrac{1}{2}\tilde{h}_1^{0^\dagger}v_1\right)\right] = -\tfrac{1}{\sqrt{2}}v_1g\tilde{h}_1^0\tilde{W}^3 + h.c. \\
&= -\tfrac{1}{2}\left(\tfrac{1}{\sqrt{2}}v_1g\tilde{h}_1^0\tilde{W}^3 + \tfrac{1}{\sqrt{2}}v_1g\tilde{W}^3\tilde{h}_1^0\right) + h.c.
\end{aligned}$$

With a basis $\left(\tilde{B} \quad \tilde{W}^3 \quad \tilde{h}_1^0 \quad \tilde{h}_2^0\right)^T$, one can fill two elements of a matrix in the following expression

(48) $$\mathsf{L}_{mass,neutralinos} = -\frac{1}{2}\cdot\left(\tilde{B} \quad \tilde{W}^3 \quad \tilde{h}_1^0 \quad \tilde{h}_2^0\right)\left(\begin{array}{cc|cc} \cdot & \cdot & \cdot & \cdot \\ \cdot & \cdot & \frac{1}{\sqrt{2}}gv_1 & \cdot \\ \hline \cdot & \frac{1}{\sqrt{2}}gv_1 & \cdot & \cdot \\ \cdot & \cdot & \cdot & \cdot \end{array}\right)\left(\begin{array}{c} \tilde{B} \\ \tilde{W}^3 \\ \tilde{h}_1^0 \\ \tilde{h}_2^0 \end{array}\right) + h.c.$$

The other elements of the 2nd and 3rd block can be found in a similar way.

All the above-mentioned information can be brought together to the following equation:

(49) $$\mathsf{L}_{mass,neutralinos} = -\frac{1}{2}\psi_n^T\hat{\mathbf{M}}_\mathbf{n}\psi_n + h.c.,$$

where $\hat{\mathbf{M}}_\mathbf{n} = \left(\begin{array}{cc|cc} M_1 & 0 & \frac{-1}{\sqrt{2}}g'v_1 & \frac{1}{\sqrt{2}}g'v_2 \\ 0 & M_2 & \frac{1}{\sqrt{2}}gv_1 & \frac{-1}{\sqrt{2}}gv_2 \\ \hline \frac{-1}{\sqrt{2}}g'v_1 & \frac{1}{\sqrt{2}}gv_1 & 0 & -\mu \\ \frac{1}{\sqrt{2}}g'v_2 & \frac{-1}{\sqrt{2}}gv_2 & -\mu & 0 \end{array}\right)$ is the neutralino mass matrix and

$\psi_n = \left(\begin{array}{c} \tilde{B} \\ \tilde{W}^3 \\ \tilde{h}_1^0 \\ \tilde{h}_2^0 \end{array}\right)$ is the neutralino gauge-eigenstate basis.[59] Using the relationships

$\frac{g\cdot v}{\sqrt{2}} = m_Z\cdot\cos\vartheta_W$ ($\vartheta_W$ is the Weinberg angle with $\sin^2\vartheta_W \approx 0.231$)[60], $g' = g\tan\vartheta_W$,

$v_1 = v \cdot \sin\beta$ and $v_2 = v \cdot \cos\beta$, the mass matrix $\hat{\mathbf{M}}_\mathbf{n}$ can be written in a more convenient way[61]

$$\hat{\mathbf{M}}_\mathbf{n} = \begin{pmatrix} M_1 & 0 & -m_Z \sin\beta \sin\vartheta_W & m_Z \cos\beta \sin\vartheta_W \\ 0 & M_2 & m_Z \sin\beta \cos\vartheta_W & -m_Z \cos\beta \cos\vartheta_W \\ -m_Z \sin\beta \sin\vartheta_W & m_Z \sin\beta \cos\vartheta_W & 0 & -\mu \\ m_Z \cos\beta \sin\vartheta_W & -m_Z \cos\beta \cos\vartheta_W & -\mu & 0 \end{pmatrix} \tag{50}$$

Since this matrix contains off-diagonal elements, the four fields in $\psi_n$ are not mass eigenstates. These mass eigenstates can be found by diagonalizing $\hat{\mathbf{M}}_\mathbf{n}$ (in other words finding the eigenvalues), i.e.

$$\psi_n^T \hat{\mathbf{M}}_\mathbf{n} \psi_n = \psi_n^T U U^{-1} \hat{\mathbf{M}}_\mathbf{n} U U^{-1} \psi_n = \chi^T \hat{\mathbf{M}}_\chi \chi\,, \tag{51}$$

where $U$ is an unitary transformation matrix (constructed with the eigenvectors of $\hat{\mathbf{M}}_\mathbf{n}$). The diagonal elements $m_{\chi_i}$ of $\hat{\mathbf{M}}_\chi = U^{-1} \hat{\mathbf{M}}_\mathbf{n} U$ (i.e. the eigenvalues of $\hat{\mathbf{M}}_\mathbf{n}$) represent the masses of corresponding mass eigenstates $\chi = U^{-1} \psi_n$, so that the mass terms in the Lagrangian are now $m_{\chi_i} \chi_i \chi_i + h.c.$, which are obviously Majorana mass terms. The convention is that the lightest neutralino get the lowest number, that means $m_{\chi_1} < m_{\chi_2} < m_{\chi_3} < m_{\chi_4}$. It is assumed that the lightest neutralino is the LSP.

The properties of the neutralino depend mainly on four parameters: the gaugino mass parameters $M_1$ and $M_2$, the Higgsino mass parameter $\mu$, and the ratio of the two Higgs vacuum expectation values $\frac{v_1}{v_2} = \tan\beta$. Various experiments give constraints on these values, which can be found, e.g. in the publications of the data particle group.[62] Just as

one assumes that the coupling constants unify at $10^{16}$GeV for the GUT model, it is predicted that the gaugino masses converge as well.[63] This leads to the relationship[61]

(52) $$M_1 = \tfrac{5}{3}\tan^2\vartheta_W M_2 \approx 0.5 M_2$$

which reduces the number of free parameters to three.

An example of a neutralino will be given here, which will be used in the next chapter to illustrate the calculation of capture, annihilation, and detection rates: $M_2 = 1200\text{GeV}$, $\mu = 110\text{GeV}$ and $\tan\beta = 2$.

(53) $$\hat{\mathbf{M}}_{\mathbf{n}} = \begin{pmatrix} 600 & 0 & -39 & 20 \\ 0 & 1200 & 70 & -36 \\ -39 & 70 & 0 & -110 \\ 20 & -36 & -110 & 0 \end{pmatrix}$$

Diagonalizing leads to

(54) $$\hat{\mathbf{M}}_{\chi} = U^{-1}\hat{\mathbf{M}}_{\mathbf{n}}U = diag(-110 \quad 100 \quad 600 \quad 1200)$$

which means that the second neutralino $\chi_2$ is the lightest one (and most likely the LSP) with a mass of 100GeV. It is composed of

(55) $$\chi_2 = \left(U^{-1}\psi_n\right)_2 = -0.08\tilde{B} + 0.07\tilde{W}^3 - 0.69\tilde{h}_1^0 + 0.71\hat{h}_2^0.$$

One can see that for this particular choice of parameters, the lightest neutralino is almost a pure higgsino.

# Chapter 4: General concepts of the Neutralino detection

In this chapter the concept of the detection of neutralino dark matter is discussed. The emphasis lies on the indirect detection of neutralinos annihilating in the center of the Earth.

Following the discussion of the previous chapter, one can assume that a huge fraction of the mass of our galaxy is made of dark matter. For this thesis, it will further be assumed that this dark matter is composed of neutralinos. These particles should be subject to gravitational fields provided by massive objects such as the Earth (or the sun, or the entire galaxy). The idea is that these neutralinos could lose energy through elastic scattering with atomic nuclei in the Earth, and become gravitational trapped. They would then undergo further scattering so that they eventually accumulate at the center of the Earth. The neutralino density in the Earth's center may be high enough to cause a significant annihilation rate among the neutralinos. The annihilation products should include neutrinos, which can be detected with the IceCube/AMANDA neutrino detector, while other annihilation products would be absorbed in the Earth before they were able to reach the Earth's surface. The neutrino is therefore an ideal messenger for such a reaction.

## 4.1 Neutralino capture rates

In the following only a rough estimate of the capture rate is made. A very detailed calculation can be found in[64,65]. In order to estimate the capture rate of neutralinos within

the Earth's gravitational field, one has to start with some basic assumptions: Usually one uses a dark matter density in our part of the galaxy with $\rho = 0.3\text{GeV/cm}^3$ and assumes an isotropic Maxwell-Boltzmann velocity distribution[64] with a peak at $v_0 = 220\text{km/s}$ (which corresponds to a root mean square velocity of $\bar{v} = 270\text{km/s}$ ).[66,67] The "observable" velocity distribution gets modified by the fact that the solar system orbits around the center of the galaxy with a speed of 220km/s.[67] This pushes the peak of the neutralino velocity distribution to a value of about $v_0' = 300\text{km/s}$.[64] This distribution gets slightly modified by the motion of the Earth around the sun.

There is a very small probability that a neutralino traveling through the Earth scatters elastically with a nuclei. Here one has to distinguish between two cases: scattering via axial-vector interaction (spin-dependent), and scattering via scalar interaction (spin-independent). Axial-vector interactions of neutralinos $\psi$ are reactions which are given by Lagrangians that involve interaction terms like $\bar{\psi}\gamma^{\mu}\gamma^{5}\psi$, while scalar interactions are governed by interaction terms containing $\bar{\psi}\psi$. Some examples are shown in Figure 7. An overview over all possible combinations is given in[68], where the total expressions become quiet lengthy, since they depend on the exact composition of the neutralino mass-eigenstates $\chi$ given in (51). It is important to note that certain neutralino models disfavor either the spin-dependent or the spin-independent interaction. This has to be taken into account for an accurate calculation of the capture rate (see below), and the choice of the detector material for direct detection experiments (see chapter 4.4).

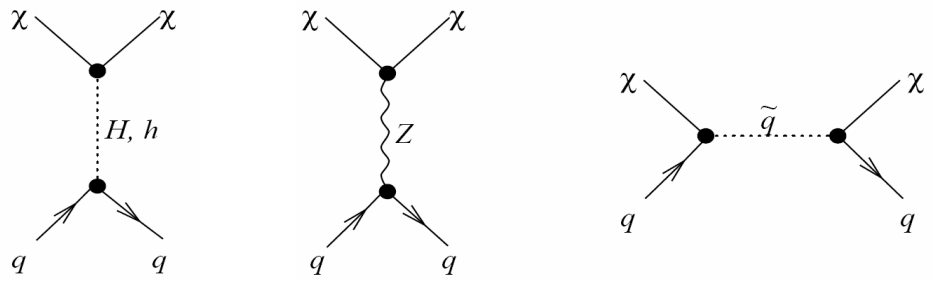


(a) (b) (c)

*Figure 7 Feynman diagrams contributing to the elastic scattering amplitude of neutralinos from quarks.*[69]
(a), (c) scalar (spin-independent) interaction
(b), (c) axial-vector (spin-dependent) interaction

The idea is that neutralinos (with kinetic energy $E_\infty = \frac{1}{2} m v_\infty^2$) from the galactic halo can lose energy through elastic scattering with atomic nuclei in massive objects like the sun or the Earth. The maximum energy loss in a collision with a nucleus is (for a scattering angle of 180°)

$$\Delta E = \frac{4 m_N m_\chi}{\left(m_N + m_\chi\right)^2} E \tag{56}$$

Within the gravitational field the neutralino's kinetic energy is $E = E_\infty + E_{esc}$, where $E_{esc} = \frac{1}{2} m v_{esc}^2$ is the kinetic energy gained at the distance $R$ from the center of the gravitational field (the loss of potential energy due to the gravitational field is compensated by this gain in kinetic energy; $v_{esc}$ is the escape velocity).[70] After a scattering with a nucleus, the neutralino's new kinetic energy is $E' = E - \Delta E$. In order to get trapped gravitationally, the kinetic energy after the collision has to be smaller that the potential energy at $R$ (which equals the kinetic energy $E_{esc}$ for the escape velocity at $R$): $E' = E - \Delta E \le E_{esc}$. This means with (56) that

$$E_\infty + E_{esc} - \frac{4 m_N m_\chi}{\left(m_N + m_\chi\right)^2}\left(E_\infty + E_{esc}\right) \le E_{esc} \text{ or}$$[70]

(57) $$E_\infty \leq \frac{4m_N m_\chi}{(m_N - m_\chi)^2} E_{esc}$$

which means that only neutralinos with energies smaller than or equal to $\frac{4m_N m_\chi}{(m_N - m_\chi)^2} E_{esc}$ lose enough energy to get trapped. This limits the maximal possible value for the neutralino velocity $v_\infty$ to[71]

(58) $$v_\infty \leq v_{crit} = v_{esc} \sqrt{\frac{4m_N m_\chi}{(m_N - m_\chi)^2}}$$

Considering that the mean escape velocity on Earth (averaged over all depths) is just 13km/s (which is much smaller than $v_0' = 300\text{km/s}$ of the neutralino velocity), usually only a small fraction of the Maxwell-Boltzmann distribution can be gravitationally caught in the Earth (i.e. most of the neutralinos are too fast). Since the average energy loss is smaller than the maximum energy loss given in (56), this fraction gets even smaller. However, this fraction of neutralinos that can be caught gets significant bigger (smaller) if the mass difference between the neutralino and nucleus is very small (large). For instance, a neutralino of 50GeV scattering on an iron nucleus gets a critical velocity of about 38.9 times the escape velocity of the Earth, which means that the entire velocity distribution of the neutralino can be considered, while this factor becomes only 3.1 for a 100GeV neutralino on iron, or even 0.3 for a 50GeV neutralino on a hydrogen nucleus. One can see that the neutralino capture on Earth is suppressed for neutralinos with masses far away from the mass of the iron nucleus. There are also other effects that need to be taken into consideration: The potential well of the sun leads to an increase of the neutralino speed for all neutralinos which enter the solar system, which reduces the

number of neutralinos that can be caught (since the average velocities are pushed further away from the critical velocity).[72] At the other hand, gravitational diffusion of neutralinos between different bound and unbound solar orbits counters this effect, so that resulting velocity distribution is similar to the case of an absent potential well.[72] However, there are newer studies which show that there is a possibility that a large part of the solar bound neutralinos maybe driven into the sun so that the probability of a neutralino being captured by the Earth is reduced again.[73]

Most of the scattering happens via scalar interaction (spin-independent), since there is only a very small fraction of nuclei with spin on Earth.[70] An exact calculation[64] would exceed the frame of this work, so only an approximate result is given here. The capture rate for neutralino-nucleon scattering via scalar interaction inside of the volume of the Earth is (taking the entire kinematics of the neutralinos into account)[74]

$$\Gamma_C = 4.8 \cdot 10^{15}\,\mathrm{s}^{-1} \frac{\rho / 0.3 \frac{\mathrm{GeV}}{\mathrm{cm}^3}}{\left(m_\chi / \mathrm{GeV}\right)\left(\bar{v} / 270 \frac{\mathrm{km}}{\mathrm{s}}\right)} \sum_i F_i \frac{\sigma_i}{10^{-40}\,\mathrm{cm}^2} f_i \phi_i S_i \frac{1}{m_{N_i} / \mathrm{GeV}} \tag{59}$$

with the neutralino density $\rho = 0.3\mathrm{GeV/cm}^3$, the neutralino mass $m_\chi$ (here 100GeV to continue the example introduced at the end of section 3.5), and the root mean square speed of the neutralinos $\bar{v} = 270\mathrm{km/s}$ (from the isotropic Maxwell-Boltzmann distribution – the motion of the solar system is implicitly included in the formula). This formula contains a sum over all nuclei $i$ found in the Earth, where one has to account for the nuclei specific parameters:[74]

- The mass of the nuclei $m_{N_i}$ (see Table 4)

- The fractional abundance of the nuclei $f_i$ (see Table 4)

- A factor depending on the velocity distribution of the nuclei in the Earth $\phi_i$ (see Table 4)

- The kinematic suppression factor $S_i = \left( \frac{A^b}{1+A^b} \right)^{1/b}$, with $A = \frac{3}{2} \frac{m_N m_\chi}{\left(m_N - m_\chi\right)^2} \left( \frac{\langle v_{esc} \rangle}{\bar{v}} \right)^2$, $b = 1.5$ and $\langle v_{esc} \rangle = 13.2\text{km/s}$, which is the mean escape velocity for the Earth (when all depths of the Earth are taken into account)

- The form-factor suppression $F_i$ is only relevant for nuclei with a high mass and/or if the energy transfer during the scattering is large. These conditions are not met. The example of $^{56}Fe$ gives $F_i \approx 1 - 0.26 \frac{A}{1+A} \approx 0.998$ for a neutralino mass of 100GeV, which shows that this factor can be ignored (nuclei which are heavier than $^{56}Fe$ or $^{59}Ni$ play only an insignificant role in the Earth's composition).

- The scalar neutrino-nucleon cross-section, which very strongly depends on the parameters of the neutralino such as gaugino-higgsino mixing ratio, the higgsino mass parameter, etc. (see (50)).[75] An approximate value can be obtained with[76] $\sigma = \alpha_H \left( G_F m_N^2 \right)^2 \frac{m_\chi^2}{\left(m_N + m_\chi\right)^2} \frac{m_Z^2}{m_H^4}$, with the Higgs mass $m_H$, the mass of the Z vector boson $m_Z = 91\text{GeV}$ and the Fermi constant $G_F = 1.2 \cdot 10^{-5}\,\text{GeV}^{-2} \left(\hbar c\right)^3$. The value of the parameter $\alpha_H$ can be taken from Figure 8. It depends on the values from (50) $M_2, \mu, \tan\beta$. Following the example form the end of section 3.5 with $M_2 = 1200\text{GeV}$, $\mu = 110\text{GeV}$ and $\tan\beta = 2$ one gets $\alpha_H \approx 0.1$.

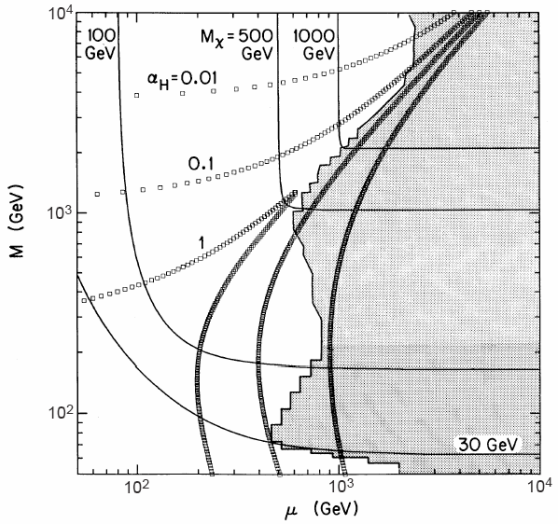


*Figure 8 MSSM parameter space for the lightest neutralino*[76]
Contours in the $M$ (Wino mass parameter), $\mu$ (Higgsino mass parameter) plane of constant $\alpha_H$ = 1.0, 0.1, 0.01 (boxes) and constant neutralino mass $M\chi$ = 30, 100, 500 and 1000 GeV (solid). The variable $\alpha_H$ is used to scale the coupling constant in the formula used in the text. The ratio of the vacuum expectation values of the Higgs was set to tanβ=2 The shaded region is excluded by cosmological considerations.

| | $N_i$ | $f_i$ | $\phi_i$ | $S_i$ * | $\sigma_i / \mathrm{cm}^{-40}$ * | $\Gamma_{Ci} / s^{-1}$ ** |
|---|---|---|---|---|---|---|
| Fe | 56 | 0.3 | 1.6 | 0.0084 | 7010 | $2.6 \cdot 10^{13}$ |
| O | 16 | 0.3 | 1.2 | 0.0007 | 82 | $7.1 \cdot 10^{10}$ |
| Si | 28 | 0.15 | 1.2 | 0.0017 | 640 | $3.7 \cdot 10^{11}$ |
| Mg | 24 | 0.14 | 1.2 | 0.0013 | 367 | $1.8 \cdot 10^{11}$ |
| S | 32 | 0.05 | 1.6 | 0.0022 | 1029 | $2.9 \cdot 10^{11}$ |
| Ni | 59 | 0.03 | 1.6 | 0.0100 | 8327 | $3.5 \cdot 10^{12}$ |
| Ca | 40 | 0.015 | 1.2 | 0.0035 | 2245 | $1.8 \cdot 10^{11}$ |
| P | 30 | 0.011 | 1.2 | 0.0020 | 818 | $3.6 \cdot 10^{10}$ |

*Table 4 List of the properties of the most abundant nuclei in the Earth*[74]
*These are values which were calculated with the formulas given in the previous page. The following values were used as an example: $m_\chi = 100\mathrm{GeV}$, $\alpha_H = 0.1$, $m_H = 120\mathrm{GeV}$.
**This is the fractional capture rate for each element

A list with the most abundant nuclei in the Earth can be found in Table 4. Putting everything into (59) one gets a capture rate for a 100GeV neutralino (with the properties chosen the end of section 3.5) in the Earth of

(60) $$\Gamma_C = 3 \cdot 10^{13}\,\mathrm{s}^{-1}$$

## 4.2 Neutralino annihilation rates

Once the neutralinos get trapped gravitationally in the Earth, they can lose more and more energy through further scattering. Eventually they can sink to Earth's core. There it is possible for two neutralinos to annihilate. Therefore, the number of neutralinos $N$ in the Earth increases through neutralino capture $\Gamma_C$ and decreases through neutralino annihilation $\Gamma_A$. This can be expressed in the following differential equation[77]

(61) $$\frac{dN}{dt} = \Gamma_C - 2\Gamma_A(N)$$

while the annihilation rate needs to be multiplied by two, since with every annihilation two neutralinos disappear (neutralinos are Majorana particles – they are their own anti-particles, and can annihilate with themselves). The annihilation rate is of course a function of $N$ – the more neutralinos are present, the higher the possibility for an annihilation:

(62) $$\Gamma_A(N) = \tfrac{1}{2} CN^2$$

The quantity $C$ will be discussed below. Note that these rates (annihilation rate, capture rate) are rates with respect to the entire volume of the Earth, unlike the annihilation rate (1) used for the calculation of the neutralino relic density or the annihilation rate per volume (77) discussed below. The differential equation becomes now

(63) $$\frac{dN}{dt} = \Gamma_C - CN^2$$

Separating variables leads to $\frac{dN}{1-\frac{C}{\Gamma_C}N^2} = \Gamma_C dt$, and the substitution $u = \sqrt{\frac{C}{\Gamma_C}}N$ leads to

$\sqrt{\frac{\Gamma_C}{C}}\int \frac{du}{1-u^2} = \Gamma_C \int dt$. The solution is $\sqrt{\frac{\Gamma_C}{C}}\operatorname{ar\,tanh}(u) = \Gamma_C t + A$ or

(64) $$N(t) = \sqrt{\frac{\Gamma_C}{C}} \tanh\left(\sqrt{C\Gamma_C}\, t\right),$$

since $A = 0$ (with the boundary condition $N(t=0) = 0$). With this expression one can also write down the annihilation rate as defined in (62)

(65) $$\Gamma_A = \frac{\Gamma_C}{2} \tanh^2\left(\sqrt{C\Gamma_C}\, t\right)$$

The quantity $C$ is calculated in the following way:[77]

(66) $$C = \langle \sigma_A v \rangle \frac{V_2}{V_1^2}$$

with the annihilation cross-section $\langle \sigma_A v \rangle$ and the effective volumes $V_j = \left( \frac{3m_{Planck}^2 T}{2\, j m_\chi \rho} \right)^{3/2}$.

With the Earth's temperature $T$ and the core density $\rho$, the effective volume becomes[77]

$$V_j = 2.6 \cdot 10^{66}\, \mathrm{GeV}^{-3} \left( j \frac{m_\chi}{10\mathrm{GeV}} \right)^{-3/2}$$

The annihilation products can be quark-antiquark pairs, lepton-antilepton pairs (soft channels), various combinations of gauge boson and/or Higgs bosons (hard channels).[78]

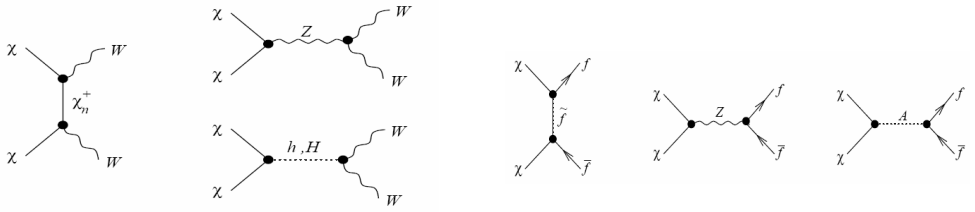


*Figure 9 A small selection of the annihilation channels of two neutralinos.*[78]

The calculation of the annihilation cross-section is very complex,[78] so that only the approximation $\langle \sigma_A v \rangle = 10^{-8}\, \mathrm{GeV}^{-2}$ (already introduced for the calculation of the relic

abundance)[29] is used here to estimate the neutralino annihilation rate. With this information one can now calculate $C$ for a neutralino mass of 100GeV: $C = 1.48 \cdot 10^{-48} \mathrm{s}^{-1}$. Using the age of the Earth $t = 1.42 \cdot 10^{17} \mathrm{s}$ and the previously calculated capture rate $\Gamma_C = 3 \cdot 10^{13} \mathrm{s}^{-1}$, one can see that the argument inside $\tanh(\sqrt{C\Gamma_C}\, t)$ becomes 0.94, and therefore $\tanh(\sqrt{C\Gamma_C}\, t) = 0.74$. This means that neutralino capture and annihilation are not in equilibrium yet, and (65) needs to be written as

(67) $$\Gamma_A = 0.27\Gamma_C$$

This leads to a value for the annihilation rate for the entire Earth of $\Gamma_A = 8 \cdot 10^{12} \mathrm{s}^{-1}$ for the above introduced example. If there was equilibrium already (like for the sun), then the annihilation rate would be exactly half the capture rate, which is easy to understand: If the equilibrium is to be maintained (the number of neutralinos stays constant), two neutralino captures are necessary for one annihilation (which removes two neutralinos).

These particles which are created through the neutralino annihilation will initiate a reaction chain, which may lead to a final state containing neutrinos. These neutrinos are the only products which can escape the core of the Earth without being absorbed. About 10% of all neutralino annihilations lead to muon-neutrinos.[79] Their energies are usually around a half (one third) of the original neutralino mass for the hard (soft) annihilation channel. The resulting muon has half the energy of the neutrino.[79]

Since the neutralinos are only weakly interacting, they are not disturbed by the presence of the matter inside the Earth, or by the presence of each other. The only influence they

experience is the gravitational field of the Earth. Therefore the neutralinos inside the Earth behave like an ideal gas. Its properties can be derived from the barometric law

(68) $$dp = -\rho_\chi g \cdot dr ,$$

where $g = G\frac{4}{3}\pi\rho_E r$ is the gravitational acceleration inside a solid sphere with density $\rho_E$ (depending on the distance from the center), and $\rho_\chi$ is the neutralino mass density, which can be expressed as

(69) $$\rho_\chi = m_\chi n_\chi ,$$

where $n_\chi$ is the neutralino number density. With the ideal gas law, the number density is $n_\chi = \frac{N_\chi}{V} = \frac{p}{kT}$, so that (assuming uniform temperature)

(70) $$dp = kT \cdot dn_\chi .$$

Expressions (69) and (70) can be plugged into (68) which leads to the follow differential equation

(71) $kT \cdot dn_\chi = -m_\chi n_\chi G\frac{4}{3}\pi\rho_E r \cdot dr$ which has the following solution[80]

(72) $$n_\chi(r) = n_{\chi 0} \exp\left(-\frac{m_\chi G\frac{4}{3}\pi\rho_E r^2}{2kT}\right) = n_{\chi 0} \exp\left(-\frac{r^2}{2A^2}\right),$$

with $A^2 = \dfrac{kT}{m_\chi G\frac{4}{3}\pi\rho_E}$ (which is $1.28 \cdot 10^{11}\,\mathrm{m}^2$ for a neutralino mass of 100GeV, an Earth core temperature[80] of 6000K, and an Earth core density of 13000kg/m$^3$)

The value of $n_{\chi 0}$ needs to be chosen in such a way that the total number of neutralinos in the entire Earth agrees with the numbers of neutralinos used in equation (62). Equation (62) leads to an expression for the number of neutralinos in the volume of the Earth:

$N = \sqrt{\frac{2\Gamma_A}{C}}$ which needs to be equal to the number density in (72) integrated over the volume of the Earth.

(73) $$\int_V n_\chi(r)dV = 4\pi n_{\chi 0}\int_0^R \exp\left(-\frac{r^2}{2A^2}\right)r^2 dr = \sqrt{\frac{2\Gamma_A}{C}}$$

Since most of the neutralinos are expected to be concentrated in the center of the Earth, this integral can be extended to infinity without a big change in the result. The result is

$4\pi n_{\chi 0}\frac{\sqrt{\pi}}{4\left(\frac{1}{2A^2}\right)^{3/2}} = \sqrt{\frac{2\Gamma_A}{C}}$ or

(74) $$n_{\chi 0} = \sqrt{\frac{2\Gamma_A}{\left(2A^2\pi\right)^3 C}}$$

which gives a value of $n_{\chi 0} = 5\cdot 10^{12}\,\mathrm{m}^{-3}$ for the example above.

## 4.3 Neutrino fluxes from neutralino annihilations

As already mentioned, there is a chance that these neutralinos annihilate. The annihilation products are usually unstable, and a fraction of their decay channels include neutrinos. For an estimation of the neutrino detection rate one can simply approximate that all annihilations happen in the center of the Earth, and that therefore all signal neutrinos are straight upward going at the surface of the Earth. In this case, one can use the total annihilation rate for the Earth calculated above: $\Gamma_A = 8\cdot 10^{12}\,\mathrm{s}^{-1}$. This leads to a neutrino flux at the Earth's surface of

(75) $$\Phi_\nu = \frac{\frac{1}{10}\Gamma_A}{4\pi R^2} = 2\cdot 10^3\,\mathrm{s^{-1}km^{-2}},$$

where $R$ is the Earth radius. The factor $\frac{1}{10}$ comes from the fact that about 10% of the annihilations lead to neutrinos. In the next chapters, it will be explained that these neutrinos can be detected, if they undergo a charged current interaction with a nucleon in the ice and produce a muon. The muon rate per detector volume can be estimated with the expression

(76) $$\frac{\frac{dR_\mu}{dt}}{V} = \Phi_\nu \sigma_{\nu N\to\mu N'}(E) n_N,$$

where $n_N$ is the nucleon density of the ice in the detector and $\sigma_{\nu N\to\mu N'}$ is the energy dependent cross-section. In order to follow the example of the 100 GeV neutralino from 4.2, one can assume that it annihilates, its annihilation products decay, and the decay products contain a 50 GeV muon-neutrino. The cross-section of such a neutrino is[79] $\sigma_{\nu N\to\mu N'} = 5\cdot 10^{-39}\,\mathrm{cm^2}\,\frac{E_\nu}{\mathrm{GeV}} = 2.5\cdot 10^{-37}\,\mathrm{cm^2}$. The nucleon density of the ice is $n_N = \rho_{ice}/m_{H_2O} \approx 1\frac{\mathrm{g}}{\mathrm{cm^3}}/3\cdot 10^{-23}\,\mathrm{g} = 3.3\cdot 10^{22}\,\mathrm{cm^{-3}}$. For a detector volume of $V = 10^7\,\mathrm{m^3}$ one gets a rate of $\frac{dR_\mu}{dt} = 0.5\,\mathrm{year^{-1}}$. Of course, this result is only an estimation for a hypothetical particle for which an arbitrary model was picked. Also, a lot of simplifications were introduced for each step of the calculation.

In order to calculate the angular distribution of signal neutrinos (as seen from the detector), one has to use the neutralino density (72). The neutralino annihilation rate (1) $\Gamma = \langle \sigma_A v\rangle n$ (which is actually the number of reactions of particle 1 per target particle 2

per time: $\frac{dR_A}{dtdN_2} = \langle \sigma_A v \rangle \frac{dN_1}{dV}$) can be transformed into an annihilation rate *per volume* by multiplying it with the "target" density $\frac{dN_2}{dV}$. One gets $\frac{dR_A}{dtdN_2}\frac{dN_2}{dV} = \langle \sigma_A v \rangle \frac{dN_1}{dV}\frac{dN_2}{dV}$ or $\frac{dR_A}{dtdV} = \langle \sigma_A v \rangle n^2$ (if one uses the fact that particle 1 and particle 2 both stand for neutralinos, and therefore have the same density). Multiplying this expression with the factor $\frac{1}{10}$ (one tenth of all annihilations lead to muon-neutrinos) leads to a neutrino "production rate per volume":

(77) $$\frac{dR_\nu}{dtdV} = \frac{1}{10}\langle \sigma_A v \rangle n^2$$

Together with equation (72) and the assumption that these neutrinos propagate radially from their position of creation, one can find the zenith distribution of the neutrino flux (see appendix L, see also[81])

(78) $$\frac{d\Phi}{\cos\vartheta \cdot d\vartheta} = \frac{1}{20}\langle \sigma_A v \rangle n_0^2 A\sqrt{\pi}\exp\left(-\frac{R^2}{A^2}\sin^2\vartheta\right)\mathrm{erf}\left(\frac{R\cos\vartheta}{A}\right)$$

where $A^2 = \frac{kT}{m_\chi G \frac{4}{3}\pi\rho_E}$ as defined in (72). This distribution is shown in Figure 10. From this angular distribution shown in Figure 10 one can see that most of the neutrinos from neutralino annihilation are straight upward going from the center of the Earth. The width of this distribution can be used to determine the mass of the neutralino. One has to keep in mind however that one does not observe the neutrino itself, but the associated muon after the neutrino underwent a charged-current interaction with a nucleus. The angular difference between the neutrino and the muon can be up to 10° for neutrinos with energies near the detector threshold, but goes down to much smaller values for higher energies (see Figure 16). This leads to zenith distributions which are more spread out.

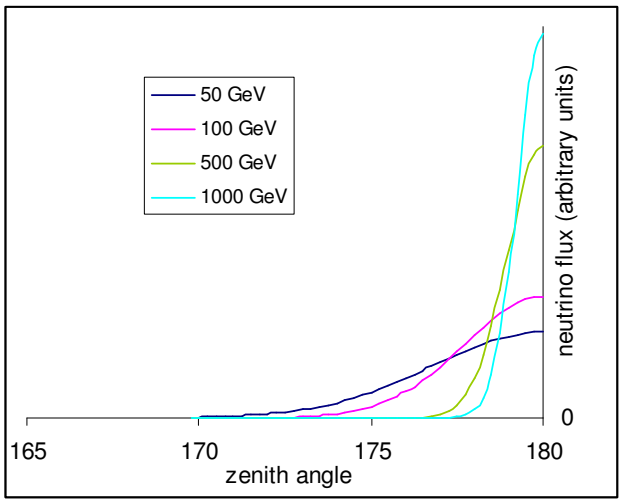


*Figure 10 Zenith distribution of the neutrino flux on the surface of the Earth for different neutralino masses*
One can see that the higher neutralino masses give a neutrino distribution with a strong peak around the vertical, while lower neutralino masses lead to broader distributions. If one discovers a signal, the zenith distribution can be used to estimate the mass of the neutralino. Note that the zenith distribution of the muon spreads this neutrino zenith distribution to wider angles (see Figure 16).

## 4.4 Other detection methods

There are – of course – other detection methods for neutralinos. The method described above is an indirect detection method, since it does not measure the neutralino itself, but rather its annihilation products. This idea of looking for neutralino annihilation products can also be accomplished in other ways.

Just like for the Earth, one expects neutralinos to get trapped inside the gravitational field of the sun. Since the escape velocity of the sun is so much higher than for the Earth, the total kinetic energy of neutralinos entering the gravitational field of the sun is also much higher. Therefore, the energy loss for a scattering with a nucleus in the sun gets also significantly higher (see (56)). This has the consequence that the form-factor suppression for this interaction has to be taken into account, especially when the neutralino mass is close to the mass of the nucleus.[70] This is certainly not the case for hydrogen, but cannot be neglected for elements with higher mass, and it has a very strong impact on the

scattering with iron. On the other hand, the high escape velocity of the sun makes it possible that a much bigger fraction of the velocity distribution of the dark matter neutralinos can be considered for capture (see (58)), provided that the mass difference between neutralino and nucleus is not too big. The large mass of the sun significantly increases the capture rate as well.

About three quarters of the sun's nuclei are hydrogen nuclei with spin ½. Their spin enables them to participate in axial-vector interaction with the neutralinos (scattering via scalar interaction is less significant for hydrogen since the cross-section for scalar interaction scales with the square of the mass of the nucleus). This might be important if it turns out that the nature of the neutralino suppresses scalar neutralino-nucleus interactions. The example in appendix M shows that spin-dependent scattering on hydrogen contributes one third of the total capture rate for the particular neutralino chosen in (55). Other nuclei with spin can be neglected for the sun.

The neutralinos accumulate inside the sun's core, and annihilate eventually. The annihilation products decay, which leads to the production of neutrinos. These neutrinos escape the sun, and can be observed with neutrino detectors such as AMANDA. Due to the large distance between sun and Earth, the neutrino flux gets strongly reduced ( $\sim R^{-2}$ ). Because of the distance between sun and Earth, the sun appears as a point source. It can be observed with AMANDA only for about half a year when the sun is below the horizon (since only upward-going neutrinos can be adequately separated from the background of downgoing muons). For this time window, the sun is never more than 23° below the horizon, so that all these neutrinos would trigger nearly horizontal events. These neutrinos have a much higher energy (about one quarter of the neutralino mass) than the

neutrinos coming from the nuclear fusion in the sun (in the order of MeV). Therefore they cannot be mistaken for ordinary solar neutrinos (which AMANDA would not be able to detect anyway).

A calculation of the detection rate for neutrinos from neutralino annihilation in the sun is done in appendix M.

Another indirect detection method makes use of the (hypothetical) neutralino annihilation in our galaxy, which would lead to detectable cosmic rays.[82] The GLAST experiment can be mentioned as an example for this particular method. GLAST is looking for mono-energetic gamma-rays originating from neutralino annihilations.

Direct detection methods make use of the small probability that neutralinos scatter elastically with nuclei of the particular detector material. For these events, a momentum transfer from the neutralino to the nuclei should occur, which may be detectable.[83] Unlike the indirect detection methods (which can only detect the neutralino's annihilation products), this method measures dark matter particles directly as they pass through Earth (or more specifically: through the detector). As mentioned before, neutralinos scattering with nuclei occurs as a combination of scalar and axial-vector interaction. Many experiments focus on scattering via scalar interaction, since the associated cross-section scales with the square of the nucleon mass. In this case, a detector material with a high nucleon mass and spin 0 is used such as $^{76}$Ge – e.g. for the experiment at the Soudan underground laboratory. Since the exact nature of the neutralino is unknown, there may be the possibility that scattering via scalar interaction is suppressed. Therefore it is important that there are also direct detection experiments that use scattering via axial-

vector interaction. An example for such an experiment is the PICASSO experiment, which uses fluorine as detector material.

A clear signature for possible neutralino signals would be an annual modulation of the event rate which comes from the motion of the Earth around the sun (which modulates the relative neutralino velocity with respect to the Earth). So far no such signals have been discovered, so that only upper limits of the cross-section could be obtained.

For a comparison on the limits achieved by various direct and indirect methods (including this analysis) see chapter 8.2.1.

Both, the direct and indirect detection methods described above, search for the dark matter particles in the universe. If these dark matter particles are indeed supersymmetric particles (or more specifically neutralinos), it will be possible to create them with a particle accelerator. The energies which can be achieved with the Large Hadron Collider (LHC) are sufficient to cover a wide range of possible neutralino models. There are a couple of different reactions involving neutralinos that may be observed at the LHC. The collision of the two initial protons can (hypothetically) create a pair of supersymmetric particles (SUSY particles must always be created in pairs due to R parity) which decay into Standard Model particles, and the lightest supersymmetric particle (LSP). If the LSP is the neutralino, it will leave no trace in the detector (since it is neutral). Its signature will be a missing momentum and missing energy.[84] If the properties of the LSP discovered at the LHC are consistent with the results obtained from the dark matter search, then one has a strong argument that the dark matter is composed of neutralinos.

# Chapter 5: The experiment

In this chapter, the practical details of the experiment are discussed. It starts by explaining the general idea behind the AMANDA detector. The next sub-section is dedicated to the neutrino itself, followed by two sub-sections which deal with background events registered by the detector, such as neutrinos from sources other than the neutralino annihilation (e.g. atmospheric neutrinos). This is followed by an explanation of the concept of neutrino-detection. It will be explained that neutrinos are detected by their associated charged leptons, which are produced by an interaction of the neutrino with the nucleus of the ice of the detector. Afterwards, the propagation of the muon through the detector will be discussed, in connection with a brief summary about Cherenkov radiation. This chapter concludes with a description of the detector hardware.

## 5.1 The idea behind the AMANDA detector

Neutrinos cannot be observed directly since they interact only weakly and gravitationally. However, this weak interaction can be used to detect the neutrino indirectly. If the neutrino undergoes a weak interaction with a nucleus, an observable cascade may be created at the interaction vertex. Furthermore, if this weak interaction happens via an exchange of a W (charged-current interaction), this neutrino will change into its associated charged lepton. These leptons will carry about half the energy of the original neutrino so that they will have a speed which exceeds the speed of light of the detector material (which is ice for the case of the AMANDA). Since charged particles with a

speed greater than the speed of light in a given material emit Cherenkov radiation, one has a method to observe the path of the lepton as it travels through the detecto,: This Cherenkov light can be captured by photomultiplier tubes which comprise the detector, and the information gathered by them can be used to reconstruct the path of this lepton. These leptons interact with the detector material which leads to cascades around the track of the lepton. These cascades, and the cascades at the interaction vertex also contain particles which exceed the speed of light of the detector material. Therefore they can also be observed via their Cherenkov radiation.

Neutrinos have a very small cross section, i.e. a very small probability to interact. Therefore one needs to have a detector, which is large enough to get at least a small number of neutrino events. Furthermore, the detector material has to be transparent enough to observe the Cherenkov radiation. The only materials which can satisfy both requirements (and is naturally available in large volumes) are water or ice. While there are experiments that use water as detector material (e.g. the ANTARES experiment on the French Mediterranean Sea coast), AMANDA is built into the ice of the glacier at the South Pole. The very low background noise rates in the ice (detectors that use water as detector material, e.g. sea water, usually have a higher noise rate coming from bioluminescence and the decay of $^{40}$K), a stable support for the detector (i.e. the solid ice), and the already existing infrastructure (Amundsen-Scott station) are big advantages which speak in favor for using the ice at the South Pole.

Their small cross section gives neutrinos an advantage over all other particles: Neutrinos are the only particles which can travel through the Earth (almost) without interaction. Therefore only particles which reach the detector after they traveled through the Earth (going upward at the detector) are used for analysis in the experiment. Only for these upgoing particles can one have a high certainty that they are neutrinos (or rather their associated charged leptons). That means we are only looking for neutrinos coming from the northern sky or neutrinos originating from the Earth's core (for the neutralino search).

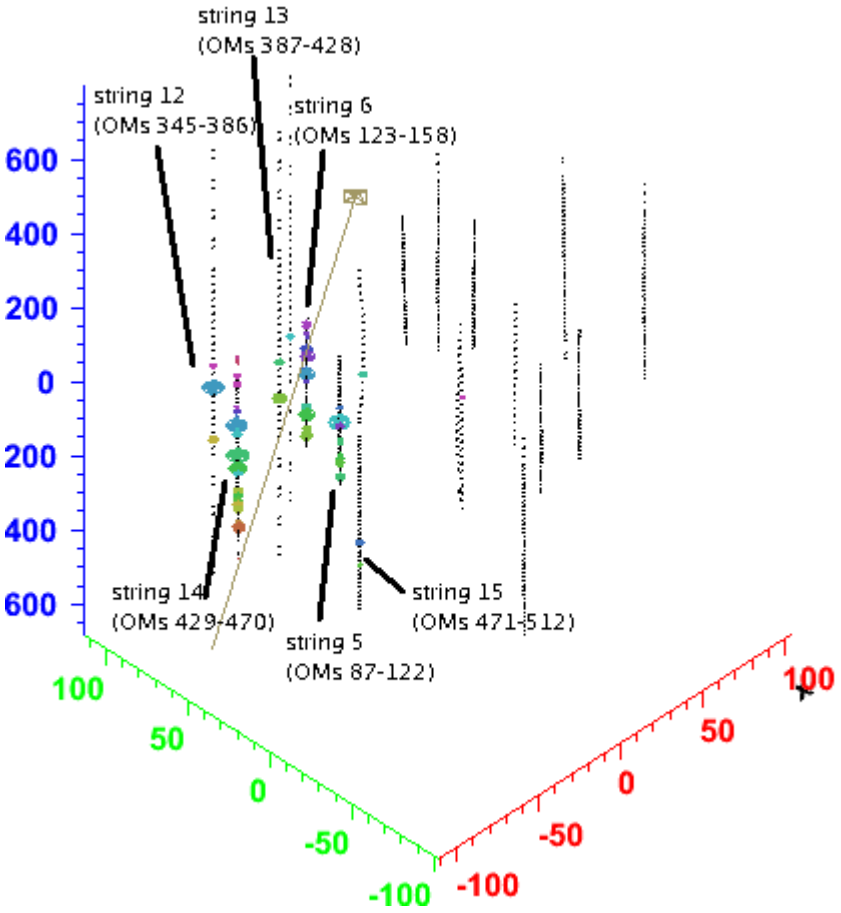


*Figure 11 Neutrino event visualized by the EventViewer.*
One can see the strings of with the attached OMs depicted as black dots. The larger circles symbolize hit OMs, where different colors and sizes stand for different arrival times and amplitudes.
The arrow indicates the reconstructed muon

## 5.2 General remarks about neutrinos

The existence of the neutrino has been first proposed by Wolfgang Pauli in 1930 to explain the missing momentum and energy of the beta decay.[85] The first detection of a neutrino took place in 1956.[85] It turned out that there are in fact three types of neutrinos. Each kind of neutrino is associated with a particular charged lepton: the electron-neutrino, the muon-neutrino, and the tau-neutrino. All of them have been observed.

Neutrinos are fermions and carry the spin ½. They belong to the class of leptons, just as their associated partners, the electron, the muon, and the tau. The neutrinos do not carry a charge, and are colorless. This means they do not participate in the electromagnetic and strong interaction. While left-handed neutrinos are subject to the weak interaction, right-handed neutrinos are not. Left-handed leptons form SU(2) doublets $\begin{pmatrix} \nu_L \\ l_L \end{pmatrix}$. Right-handed leptons are singlets under SU(2): $\nu_R$ and $l_R$.

There is evidence that neutrinos possess a mass. This is a fact which was unknown until recently when the so-called neutrino oscillation was discovered. Before that time, the neutrino was usually treated as a massless particle traveling with the speed of light. This approximation is still used today for many purposes since the neutrino mass is indeed very small.

For more information about the neutrino mass, including neutrino mixing, neutrino osciallation, the seesaw mechanism and sterile neutrinos see appendix I.

## 5.3 Background neutrinos

The major source of background neutrinos comes from atmospheric neutrinos. They are produced by cosmic rays – consisting mostly of protons, but also helium nuclei, and heavier elements – interacting with the nuclei of Earth's atmosphere. The resulting reactions lead mainly to protons, neutrons, pions, kaons. Pions and kaons are unstable particles; their decay products include neutrinos (the atmospheric neutrinos) and other particles which may decay further (which leads to additional neutrinos). The dominant decay channels are listed in Table 5. For energies considered here, the production of charmed mesons does not play a significant role; however, it becomes the dominant neutrino source for higher energy.

| decay channel | fraction |
|---|---|
| $\mu^+ \to e^+ \nu_e \overline{\nu}_\mu$ | ≈100% |
| $\pi^+ \to \mu^+ \nu_\mu$ | (99.98770±0.00004)% * |
| $\pi^0 \to \gamma\gamma$ | (98.798±0.032)% |
| $\pi^0 \to e^- e^+ \gamma$ | ( 1.198±0.032)% |
| $K^+ \to \mu^+ \nu_\mu$ | (63.54 ±0.14)% * |
| $K^+ \to \pi^+ \pi^0$ | (20.68 ±0.13)% |
| $K^+ \to \pi^+ \pi^+ \pi^-$ | ( 5.59 ±0.04)% |
| $K^+ \to \pi^+ \pi^0 \pi^0$ | ( 1.761±0.022)% |
| $K^+ \to \pi^0 e^+ \nu_e$ | ( 5.08 ±0.05)% |
| $K^+ \to \pi^0 \mu^+ \nu_\mu$ | ( 3.35 ±0.04)% |
| $K_S^0 \to \pi^+ \pi^-$ | (69.20 ±0.05)% |
| $K_S^0 \to \pi^0 \pi^0$ | (30.69 ±0.05)% |
| $K_L^0 \to \pi^+ e^- \overline{\nu}_e, \pi^- e^+ \nu_e$ | (40.55 ±0.12)% |
| $K_L^0 \to \pi^+ \mu^- \overline{\nu}_\mu, \pi^- \mu^+ \nu_\mu$ | (27.04 ±0.07)% |
| $K_L^0 \to \pi^0 \pi^0 \pi^0$ | (19.52 ±0.12)% |
| $K_L^0 \to \pi^+ \pi^- \pi^0$ | (12.54 ±0.02)% |

*Table 5 Dominant decay channels of myons, pions and kaons.*[86]

*The decay into electrons (positrons) and (anti-) electron-neutrinos is suppressed. An explanation for that can be found in appendix K.

One can see in Table 5 that the muon-neutrinos make up a large fraction of the neutrinos produced in the atmosphere by cosmic rays. Additionally to these mentioned decay channels, the particles continue to interact with the atoms of the atmosphere which lead to extensive electromagnetic and hadronic cascades – the so-called air shower. The energy spectrum of the flux of the atmospheric neutrinos can be described by a power law $\Phi \sim E^{-2.7}$ for neutrinos up to 100GeV and $\Phi \sim E^{-3.7}$ for higher energies.[87]

In addition to these atmospheric neutrinos, one also expects neutrinos of extra-terrestrial origin, and they are in fact one of the main motivations behind the AMANDA/IceCube experiment. Examples are neutrinos coming from our galaxy due to the interaction of cosmic rays with the interstellar matter, but also neutrinos produced through interaction of cosmic rays with the solar atmosphere (which is an important factor when looking for neutrinos coming from neutralino annihilation in the sun). On the other hand, neutrinos coming from the thermonuclear synthesis in the sun have only energies on the order of 1 MeV, and can therefore not be detected with AMANDA. Other, more distant possible sources include active galactic nuclei, gamma-ray bursts, supernovae, supernova remnants, etc.

Neutrinos from radioactive decays do not contribute since their energies are too low, typically in the keV and MeV range. This is far below the threshold of AMANDA, which is around 10GeV.

Neutrinos are unique messengers from astrophysical sources for energy regions where other particles fail. Probably the most natural candidate – the photon – can be used as messenger only for energies up to $10^{12}$eV. Above this energy, they interact with the infrared radiation in the universe, the cosmic microwave background (CMB), and even radio waves to produce electron-positron pairs, so that their attenuation length gets

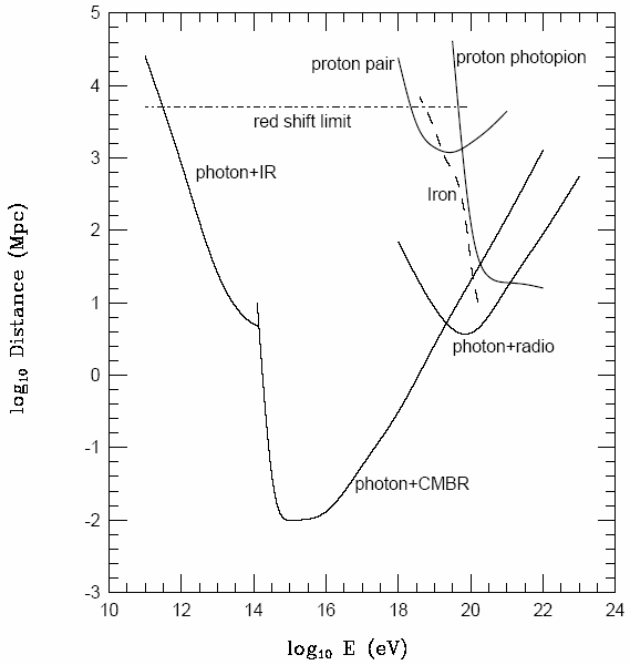


*Figure 12 Attenuation length of photons, protons and iron in various background radiations as a function of energy.*[88]
The dot-dashed line represents the absolute upper limit on the distance a particle can travel towards Earth, regardless of its initial energy.

significantly reduced (see Figure 12).[88] Other particles are either unstable, so that they are useless as information carrier or they are electrically charged. Charged particles, such as protons and electrons are bent by the magnetic field of the universe so that their origin cannot be reconstructed. Only protons in the range above $10^{19}$ eV may have high enough velocities so that their curve radii are large enough that they still point back to their source. However, these protons have another limitation at about $5 \cdot 10^{19}$ eV where they start to react with the CMB, so that their mean free path gets strongly reduced. This so-called GZK limit (named after Greisen, Zatsepin, Kuzmin) provides a very important upper limit to the cosmic rays. It is governed by the following reaction

$p + \gamma_{2.7\mathrm{K}} \left\{ \rightarrow \Delta^{+}_{1232} \right\} \rightarrow \pi^{+} + n \ \left( \text{or } \ \pi^{0} + p \right)$ where the $\pi^{+}$ decays and can produce very high energetic muon neutrinos. Another reaction which limits the mean free path of the protons is the electron-positron pair-production caused by their interaction with the CMB, however this reaction has a much smaller impact. The mean free path of electrons and positrons is limited by the inverse Compton Effect.

The aforementioned atmospheric neutrinos represent an irreducible part of the background. In order to distinguish potential signal neutrinos (e.g. extraterrestrial neutrinos, neutrinos from neutralino annihilation) from the atmospheric neutrinos, one has to look for a clustering of events around a particular direction (in the case of point sources) and/or an excess of neutrino events over the expected background level of atmospheric neutrinos. Finding an excess of events provides a difficulty, since the number of expected events depends on the type of cuts (for filtering, etc.) which are applied on the data. This means that there is no "fixed" number of expected events. Therefore it is necessary to compare the date with simulated atmospheric neutrinos to which the same cuts are applied. The topic of the simulation is discussed in chapter 7.1.2.

## 5.4 Other background particles

Of course, the background does not just consist of neutrinos. The most important contribution to the background comes from so-called atmospheric muons produced in the air showers (see above), which can penetrate the detector from above. Other components of the air showers are blocked by the ice layers on top of the detector.

The atmospheric muons make up by far the largest fraction of events registered by the detector. Fortunately these particles cannot travel through Earth – neutrinos are the only particles which are able to pass through Earth. Therefore particles that have been identified as upward going (through the Earth) are neutrinos (detected by their associated muons from charged current interaction); particles which come from above are ignored. In other words, the AMANDA experiment uses the Earth as a filter, which lets only neutrinos through and filters out all other particles. Since such a neutrino filter does not exist for particles coming from above, only particles coming from below are considered here.

## 5.5 The detection of neutrinos

Neutrinos are subject to weak interaction only. This means that there are two classes of reactions to be considered:

(79) the neutral current interaction (NC) via an exchange of a $Z^0$:

$$\nu_l + N \rightarrow \nu_l + X$$

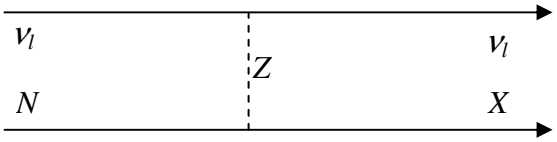


*Figure 13 Neutral current interaction between a neutrino and a nucleus*

(80) and the charged current interaction (CC) via an exchange of a $W^{\pm}$:

$$\nu_l + N \rightarrow l + X$$

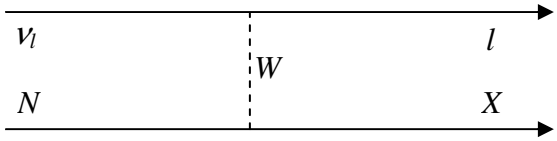


*Figure 14 Charged current interaction between a neutrino and a nucleus*

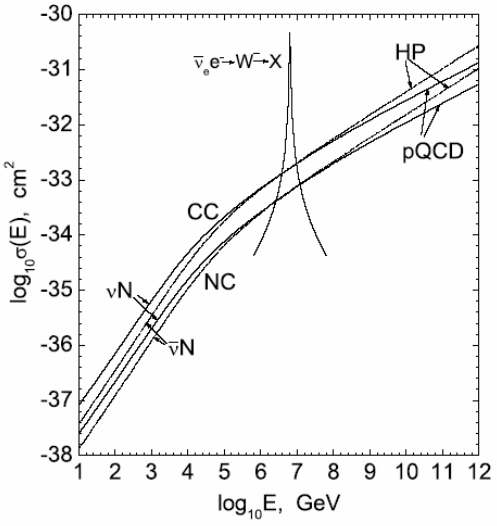


*Figure 15 Neutrino-nucleon cross-section and neutrinos-electron resonance cross-section*[89]

Both interactions lead to hadronic cascades $X$ at the interaction vertex. In the case of the NC interaction this hadronic cascade is the only effect than can be observed, since the neutrino continues to travel through the ice without further interaction.

The picture looks different for the CC interaction. This reaction leads to a charged lepton which interacts with the ice. However, the interactions are different for each lepton flavor.

An electron leads to an electromagnetic cascade. Since the electron travels only a short distance before it is stopped in the ice, the cascade is limited to the vicinity of the original vertex.

A muon, at the other hand, can travel large distances before it stops or decays. On its way, the muon is subject to different kinds of interactions, such as ionization, bremsstrahlung, direct pair-production, and photo-nuclear interactions (see next chapter). These processes lead to electromagnetic cascades (or hadronic cascades in the case of photo-nuclear interactions) along the muon track.

The tau lepton decays very fast, and produces a hadronic cascade at its decay vertex due to the decay into a meson (e.g. pion or kaon) or an electromagnetic cascade for a decay into a muon or electron. Since the distance between creation and decay is very short, the cascades at both vertices cannot be distinguished. Only for very high energies are both cascades separated by a significant distance. The tau is (like the muon) subject to interactions with the ice, however the cascades produced along the tau track are much weaker than those produced by the muon.

As one can see, the only process that creates a detectable track is the charged current interaction of muon-neutrinos, which produce muon tracks.

An electromagnetic cascade is triggered when a charged lepton emits bremsstrahlung due to its deceleration (and acceleration) caused by the presence of an electromagnetic field of a nucleus. The beginning of an electromagnetic cascade can also be the direct pair-production of an electron-positron pair (where the charged lepton emits a virtual photon which interacts with the electromagnetic field of a nucleus to trigger an electron-positron pair-production). If the “real” photons of the bremsstrahlung interact with the field of a nucleus, it can also lead to pair-production. These new particles itself can also trigger a direct pair-production or emit bremsstrahlung (which can again lead to pair-production), and so on (therefore the name cascade). All electrons/positrons of the cascade cause Cherenkov radiation as long as they are faster than the speed of light in ice (see chapter about Cherenkov radiation).

The development of a hadronic cascade is similar to the electromagnetic cascade. The difference is that it involves hadrons and is driven by the strong force rather than the electromagnetic force (the weak force is insignificant since decay channels via the weak force have a very low rate). Only the charged particles (as long as they are faster than the speed of light in ice) of the cascade can contribute to the Cherenkov radiation. This is one of the reasons why hadronic cascades produce less Cherenkov radiation than electromagnetic cascades. Another reason is that the particles involved have more mass. That means that fewer particles can be produced, and they move slower. Since charged particles are a part of the hadronic cascades, a fraction of the hadronic cascade can turn into an electromagnetic cascade.

The Cherenkov radiation emitted by the "original" charged lepton and by its associated cascades is captured by the AMANDA detector.

If one uses muons to get information about its parent neutrino, one has to keep in mind that there is an angular difference between the incoming neutrino and the outgoing muon (see Figure 16).[89] The mean difference goes up to 10° for neutrinos near the energy threshold of the detector, but becomes significantly smaller for neutrinos with higher energies. This causes the original zenith distribution of the neutrinos coming from neutralino annihilation shown in Figure 10 to get spread out.

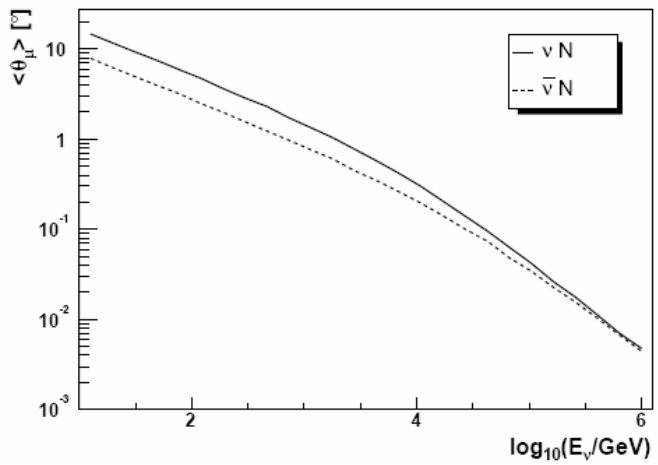


*Figure 16 Average angle between the incoming neutrino and the outgoing muon in a CC reaction as a function of the neutrino energy.*[89]

## 5.6 Muon propagation in the ice

While neutrinos interact only weakly and therefore have a very small interaction rate so that they pass through matter almost undisturbed, the muons have a much higher interaction rate due to the fact that they are also subject to the electro-magnetic interaction in addition to the weak interaction. There are five phenomena that take place while the muon propagates through the ice. They can be categorized into two groups: continuous processes and stochastic processes, which happen only randomly.

The two processes which belong to the first group are the ionization of the surrounding matter and the Cherenkov radiation. While Cherenkov radiation (explained in the next section) leads only to an insignificant energy loss, ionization is the major factor for the decrease of the muon's energy for lower energies. The energy loss due to ionization happens through Coulomb interaction of the muon with the electrons of the atoms along

its path. This leads to an energy transfer to the electrons, which either excite the atoms or even ionize them (where the freed electron is called δ-electron).

Stochastic processes include bremsstrahlung, direct pair-production, and photo-nuclear interactions. These reactions become the dominant source of the energy loss of the muon for higher energies. Bremsstrahlung is the phenomenon that leads to the radiation of photons for charged particles which are decelerated (and also when accelerated), e.g. because of the presence of an electromagnetic field such as the field of a nucleus. Virtual photons emitted by the muon may also interact with the electromagnetic fields of the nucleon. This may lead to the production of electron-positron pairs (the so-called direct pair-production) or to the excitation of the nucleus itself, which in turn can result in a hadronic cascade. Both, the bremsstrahlung and the direct pair-production can trigger an electromagnetic cascade.

If the particles of the cascades (and also the δ-electrons) are faster than the speed of light of the ice, then they produce Cherenkov radiation. This enhances the visibility of the muon track.

The average energy loss of the muon can be parameterized by the following equation:

(81) $$\left\langle \frac{dE}{dX} \right\rangle = \alpha(E) + \beta(E)E ,$$

where $X$ is the thickness of the material which the muon has traveled through (in $\mathrm{g \cdot cm^{-2}}$), $\alpha \approx 2\mathrm{MeV g^{-1} cm^{2}}$ describes the energy loss due to ionization, and

$\beta \approx 4 \cdot 10^{-6} \mathrm{g}^{-1}\mathrm{cm}^2$ stands for the energy loss caused by bremsstrahlung, direct pair-production and photo-nuclear interactions.[90]

The higher the energy of the muon the longer length of the path it can travel before it is stopped and/or decays. This path length is also called muon range. High muon ranges enable the detector to observe muons which were produced far away from the instrumented detector volume (as long as their path intersects the detector). This leads to an increase of the effective volume of the detector for high energy muons.

## 5.7 Cherenkov Radiation

Even though this type of radiation was observed before, it had not been studied in detail before 1934 by Vavilov and Cherenkov (that's why the term Vavilov-Cherenkov radiation is used in Russian texts). A theoretical description was provided by Frank and Tamm in 1937.

The phenomenon of the Cherenkov radiation occurs when charged particles travel through a medium with a velocity $v$ which is higher than the medium's phase velocity of light $c_{phase,medium}(\omega) = \frac{c}{n(\omega)}$, where $n(\omega)$ is the frequency dependent index of refraction of the medium. The radiation is emitted with an angle of $\vartheta_C(\omega) = \arccos\frac{c_{phase,medium}(\omega)}{v} = \arccos\frac{c}{vn(\omega)}$. The radiation spectrum can be characterized by the Frank-Tamm formula $\frac{d^2E}{dxd\omega} = \frac{q^2}{4\pi\varepsilon_0 c^2}\omega\left(1 - \frac{c^2}{n(\omega)^2 v^2}\right)$, where $E$ is the radiated

energy, $q$ is the charge of the particle and $x$ is the distance traveled by the particle. Cherenkov radiation has a continuous spectrum. However, it is limited by the above mentioned Cherenkov condition that the particle speed needs to be larger than the phase velocity of light inside the medium. At high frequencies (typically far ultraviolet), most media have an index of refraction that is smaller than one, which leads to a phase velocity exceeding the speed of light (this doesn't violate relativity since the signal velocity does not exceed the speed of light). For these frequencies, the Cherenkov condition cannot be satisfied anymore, so that the Cherenkov radiation spectrum has a cut-off at high frequencies.

In the visible region, the intensity is approximately proportional to the frequency, since $n(\omega)$ does not change much for these frequencies, so that the violet end of the spectrum has the highest intensity. This is the reason why Cherenkov radiation can be observed as a bluish light, e.g. in the water tanks of nuclear reactors.

Specifically for this experiment: The index of refraction for ice is 1.33 in the visible region. Under the assumption that the particles travel with the speed of light, one gets a Cherenkov angle of 41.2°. The Cherenkov radiation can be detected by photomultiplier tubes placed around the path of the muon traveling through the ice.

## 5.8 Photomultiplier Tubes

Photomultiplier tubes[91] (PMTs) are light-sensitive devices which are able to produce electrical signals in response to *single* photons. This gives them the ability to detect even the faintest signal. Another advantage is their very fast response. The rise times of a pulse and the pulse widths are typically just a few nanoseconds. This enables them to provide a very high time resolution for the AMANDA detector.

The basic elements of a PMT are the photocathode, a number of dynodes and the anode, which are put inside a vacuum tube. If a photon with a particular energy $E = hf$ hits the photocathode, it can transfer its energy to an electron of the cathode material. If the energy is bigger than the work function of the material, then the electron is able to leave the surface (external photoelectric effect). This happens with a probability (quantum efficiency) of around 10% to 30% depending on the wave length.[91]

The free electron (photoelectron) is accelerated by an electric field between the cathode and the first dynode (the first dynode has a higher electric potential than the cathode). After the electron hits the dynode, the energy it acquired gets transferred to other electrons at the dynode. These electrons can leave the surface of the dynode if they get enough energy from the photoelectron. These electrons get accelerated again by an electric field between the first dynode and the second dynode (the second dynode is at a higher electric potential than the first dynode). There, the electrons transfer their energy to the electrons of the second dynode, which will be accelerated towards the third dynode, and so on. The ratio $\delta$ between the number of (emitted) secondary electrons and

(incoming) primary electrons at each dynode is between 3 and 6, and depends on the voltage difference between two dynodes.[91]

Each AMANDA PMT consists of $n = 14$ dynodes[92], so that where one has an amplification of $\delta^n$ after the last dynode. After the last dynode, the electrons get accelerated towards the anode, which is put at the highest electric potential compared to the cathode and the dynodes. The anode collects the electrons, which leads to a measurable electrical signal. The anode efficiency $\alpha$ multiplied by the dynode amplification gives the gain[91] of the PMT $\mu = \alpha \cdot \delta^n$.

Unfortunately, there is a chance that a signal is produced even without a photon striking the cathode. There are several reasons for this effect, which are described for example in the PMT handbook by Hamamatsu[91]. One of the first analysis steps is used to remove these noise pulses (see hit cleaning 6.2)..

## 5.9 AMANDA's hardware and DAQ

The AMANDA detector consists of 680 optical modules (OMs). Each OM contains a photomultiplier tube (PMT) which is put into a glass pressure housing, and connected to a high voltage cable and a signal cable (see Figure 18). These OMs are attached on strings which were embedded into the ice after a hot water drill created a hole of up to 2400m deep (depending on the string number). The detector consists of 19 strings which were deployed between 1996 and 2000 (see Figure 17 and Table 6).

| strings | deployed | signal cables |
|---|---|---|
| 1–4 | January 1996 | coaxial cables |
| 5–10 | December 1996 / January 1997 | twisted pair cables |
| 11–19 | January 1998,<br>December 1999 / January 2000 | fiber optics cables |

*Table 6 Deployment stages of the AMANDA detector*[92]

The major part of the active volume of the detector lies between 1500m and 2000m below the surface of the Antarctic ice (at this depth most of the ambient light from the surface has been absorbed). The strings are arranged in concentric circles, where the outer-most circle has a radius of about 100m.

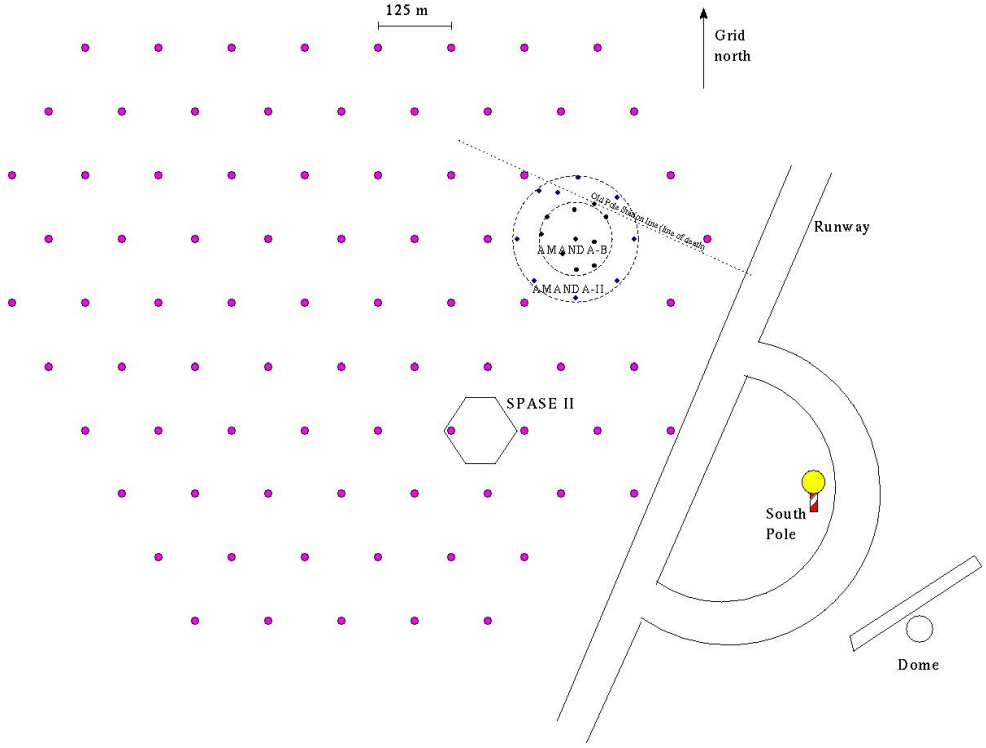


*Figure 17 Map of the AMANDA detector as part of the IceCube detector, which is close to the geographic South Pole*[93]

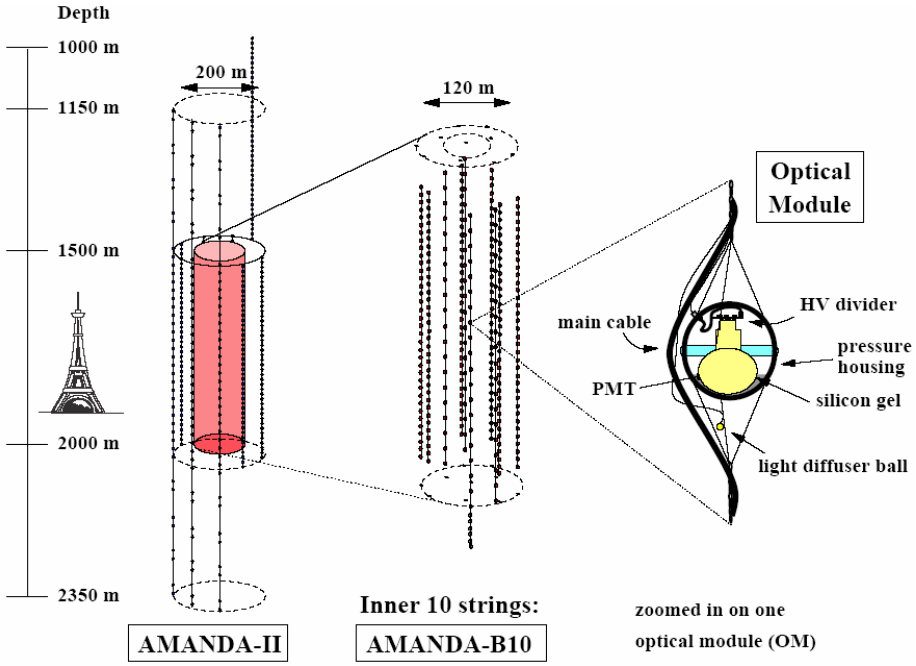


*Figure 18 The AMANDA detector*[94]

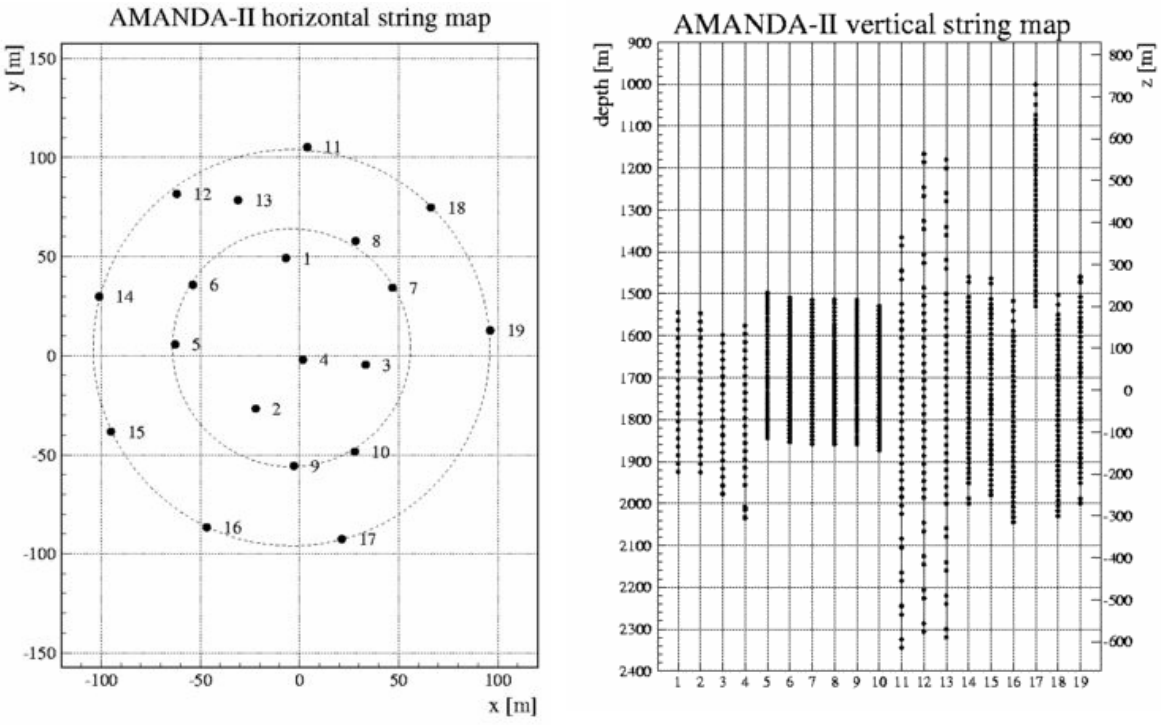


*Figure 19 The AMANDA coordinate system*[95]
The x-coordinate has longitude 90° East
The y-coordinate has longitude 0° and is Grid North in Figure 17

The PMTs[92,96] (8 inch PMT manufactured by Hamamatsu) are operated at a gain of about $10^9$ ($3 \cdot 10^8$ for strings 14-19), which leads to an amplitude of about 1V for a pulse produced by one photoelectron with a pulse width of about 7ns. This signal is transmitted from the optical module to the surface. For electrical cables (twisted pair and coaxial cables) the signal disperses to up to 200ns (or even more for coaxial cables), because of the travel length of 1 to 2 km to reach the surface (see Figure 20). For fiber optic cables the dispersion is minimal, so that the signal gets stretched to a width of only about 14ns.[92] In addition to the optical modules which transport the signals to the surface in an analog form, string 18 uses digital optical modules (DOMs), which transform the PMT output directly into a digital waveform.[92] These waveforms are transmitted to the surface without loss of information. Even though there are huge signal dispersions for electrical cables, it is still possible to achieve a time resolution of 5ns.[92]

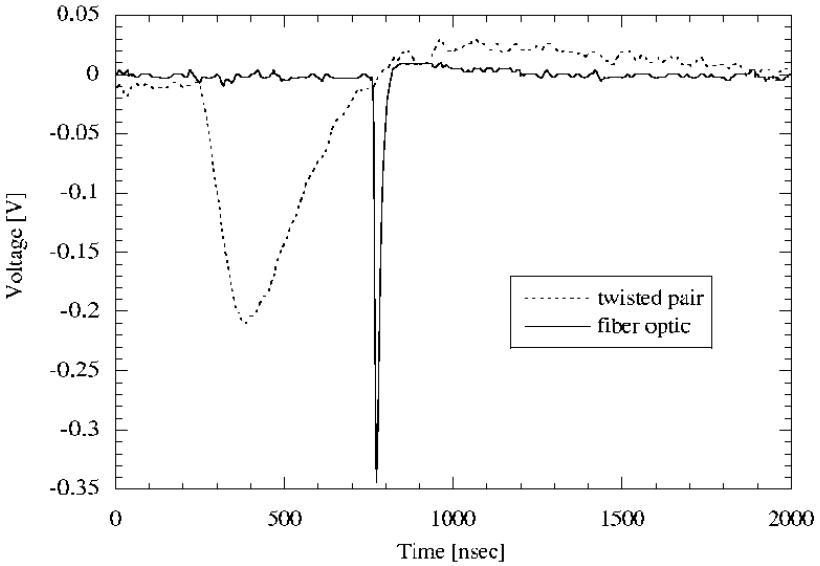


*Figure 20 Single photoelectron pulse recorded with twisted pair cable and optical fiber transmission.*[92]

The analog signals from each OM (basically the anode current) are collected at the surface in the counting house. The electrical signals from strings 1-10 are sent to the SWAMP (Swedish Amplifier) where they are amplified.[97] Signals coming through the

fiber optics cable from strings 11-19 get converted into electrical signals at the ORB (Optical Receiver Board).[97] In both cases the signal is split into prompt and delayed signals, where the delay is about 2μs.[97] The prompt signal is sent to a voltage discriminator, which in turn sends its output to the AMANDA trigger system and the TDC (time-to-digital converter).[97] The TDC stores the times of up to 16 pulse edges (leading and trailing edges of a pulse, i.e. when the voltages passes the discriminator threshold) within 32μs with a precision in the order of 1ns.[98] The delayed signal is used by the ADC (analog-to-digital converter), were the highest amplitude of the voltage within 6μs is recorded.[97]

The internal trigger system provides two options: The first one is the multiplicity trigger which requires 24 hit OMs within a time window of 2.5μs (where the time window is constantly shifted). The other one is the string trigger which requires 7 hit OMs out of 11 neighboring OMs on one string within the same time window of 2.5μs (or 6 out of 9 OMs for string numbers 1-4). There are also external triggers which can be incorporated, e.g. signals from SPASE (the South Pole Air Shower Experiment at the surface of the ice at the location of AMANDA). Once a trigger condition is satisfied, the ADC gate is opened for a time window of 4μs.[98] After 10μs a stop is issued to the TDC.[98] The TDC and ADC information, together with the GPS time of the event are stored. Afterwards the system incurs a dead time.

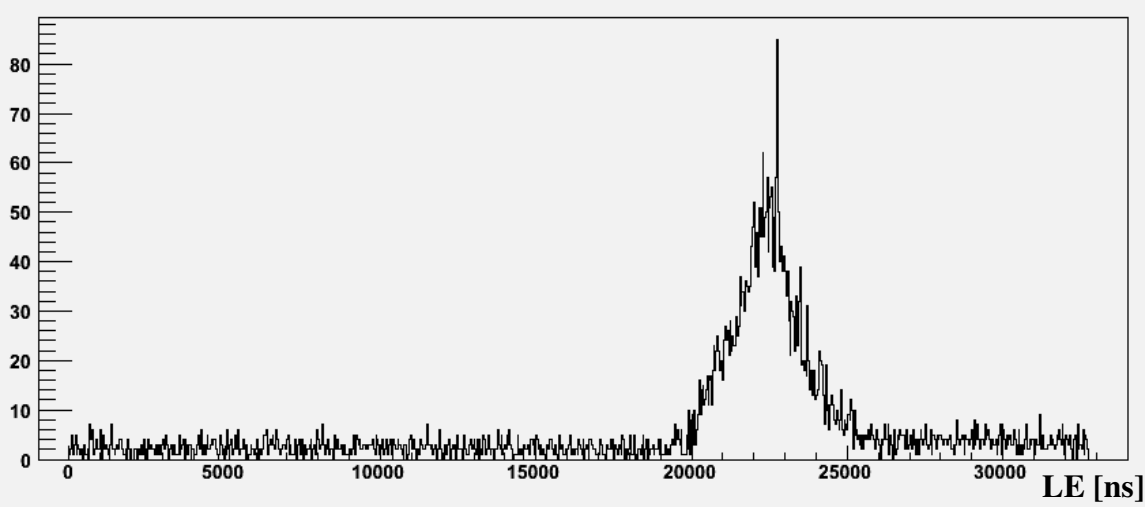


*Figure 21 Leading Edge Histogram for OM 30 on String 5.*
The peak at around 23000ns corresponds to the times when this particular OM was the one which triggered the event, i.e. it was the 24$^{th}$ hit within 2.5µs. Entries which are far outside of the bulk of the distribution are either noise hits or after pulses. Note that these entries are not calibrated yet.

With these time settings, up to 16 edges are recorded for each OM starting at 22µs before the trigger time until 10µs after the trigger time. This means that up to 8 full pulses can be stored. If leading and/or trailing edges of some of these 8 pulses are missing, edges of other pulses are recorded instead. The information about all other edges is lost.

The peak (ADC value) is selected from the highest amplitudes within a time frame starting at 2µs before the trigger time and until 2µs after the trigger time (which takes into account that the ADC uses the delayed signal mentioned above). It is a disadvantage of this setup that only the voltage of the highest peak is recorded. If there is more than one pulse, the amplitudes of the other pulses are lost. Also, there is no information about which pulse belongs to the amplitude that was recorded, i.e. which pulse had the highest peak.

The data is stored on magnetic tapes (which are shipped from the Pole during the Antarctic summer), and partially also transmitted to the northern hemisphere via satellite. For 2001 there was a data rate of 80 kB/s.[92]

### 5.9.1 Outlook for IceCube

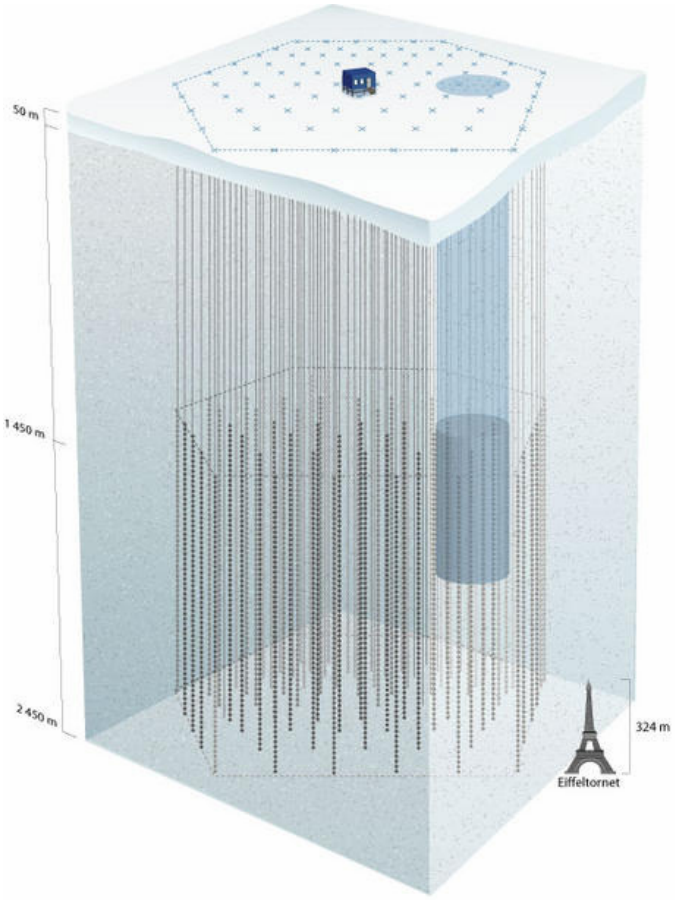


*Figure 22 The IceCube Detector*

The success demonstrating that AMANDA could detect neutrinos led to the construction of a new experiment: the IceCube neutrino telescope. This new detector is built around the old AMANDA detector (see Figure 17). It will consist of 80 strings with 60 OMs each. The first string was deployed January 2005, and it is anticipated that the last string will be installed in the ice by 2011. 40 strings are deployed currently. IceCube operates under the same principle as AMANDA, however several improvements were made, where the most significant change is that the OMs are now digital optical modules. This means that the waveforms produced by the photomultiplier tubes get digitized directly at the OMs.

The IceCube detector will cover a physical volume of $1km^3$. This will significantly improve the detection rate. However, a larger spacing between individual strings will be a disadvantage for the detection of low energy muons (since they have shorter track lengths), which are especially important for the detection of signals from low mass neutralinos. This problem is a little bit less significant for vertical upward going tracks in proximity to a string, since the OM spacing along the strings is small enough to give a sufficient number of hits even for tracks with a short length (i.e. with low energy). This is the type of tracks one expects from neutrinos coming from neutralino annihilation in the Earth.

There is a plan for an extension to IceCube, which is "Deep Core". Deep Core will be situated inside of IceCube at a location of very clear ice and will consist of six additional strings with much smaller spacing between the strings and also a much smaller distance between the OMs along the string. Also, the OMs will have a higher quantum efficiency. This will give Deep Core a much better behaviour in the lower energy region (and also a lower energy threshold), which is very important for the detection of neutrinos coming from the annihilation of low mass neutralinos.

# Chapter 6: Data Processing

The ADC and TDC information recorded – the so-called raw data – cannot be used directly. First, the raw data needs to be converted into "useful" units, such as number of photo electrons, and time. The next step is the hit cleaning which tries to remove hits that were most likely not caused by a "particle event", i.e. noise, cross-talk, etc. Afterwards the remaining hits are used to reconstruct the track of the particle that caused this event.

## 6.1 Calibration

The voltage given by the ADC is simply multiplied by an OM specific factor (after subtracting the OM specific pedestal) to get the number of photo electrons that caused this pulse.

The TDC values must also be multiplied by an OM specific value ($\beta$), in order to translate them from "counts" of leading and trailing edges ($LE_{raw}$ and $TE_{raw}$) into times. Furthermore the cable length must be taken into account. Here one subtracts the time ($t_0$) it takes for the signal to travel from the position of the OM to the DAQ electronics. This time offset is determined with the help of laser pulses (from a YAG laser) which are sent via optical fiber to a diffuser located below the OM. Another correction has to be done: The higher the peak of the pulse is, the earlier the voltage crosses the threshold (i.e. the leading edge), since the rise time for larger pulses is shorter. This effect is equal to the inverse of the square root of the amplitude ($A$) times an OM depending constant ($\alpha$).

The total equation for the leading edge is $LE = LE_{raw} \cdot \beta - t_0 - \alpha / \sqrt{A}$. The time over threshold is $TOT = (TE_{raw} - LE_{raw}) \cdot \beta$.

## 6.2 Hit Cleaning

The recorded events usually contain many noise hits. There are several techniques to remove them. In order for a hit not to be regarded as a noise hit, it needs to satisfy certain criteria. These include:

- The time over threshold (TOT) must be inside a certain range. This range is determined for each OM individually.
- The LE must be between 16500ns and 23500ns.
- The amplitude must be between 0.1 and 1000 photoelectrons.
- Each hit must satisfy a coincidence requirement, i.e. there must be at least one other hit within 100m and a time interval of 500ns.

There is a list of OMs which are considered to be either unstable or dead. “Hits” which occur on those OMs must be removed as well.

There is another category of hits that must be removed. These are hits which are produced by crosstalk between cables at the same string. This phenomenon only presents itself on strings which use twisted pair cables (strings 5–10). There are two signatures for crosstalk that one can search for.

It has been found that hits that were produced by crosstalk have a certain TOT-ADC correlation. In a TOT-ADC plot there are certain regions which should be excluded since hits in this region are most likely produced by crosstalk. The border of this region can be described by the following: All hits that have an uncalibrated ADC value which is larger than $ADC = \exp(a + b \cdot (TOT + \alpha)^c + [(TOT + \alpha)/e]^d + \beta$ (blue line in histogram below) are considered to be cross-talk hits (the constants $a, b, c, d, e, h$ are OM specific, $\alpha$ and $\beta$ are global constants).

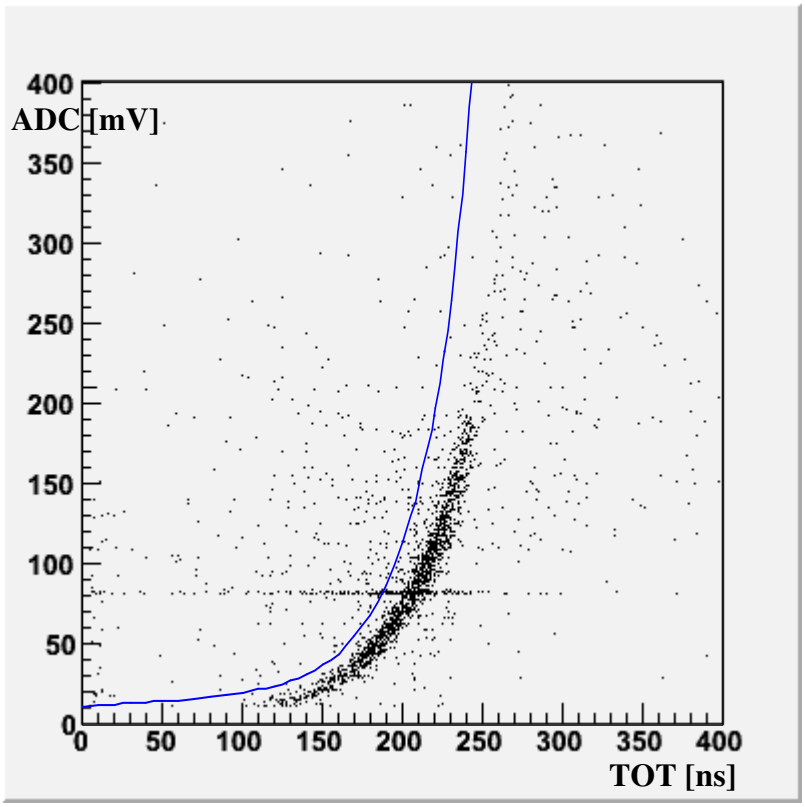


*Figure 23 ADC-TOT cross-talk plot*
This plot visualizes the region in which hits are rejected because they are suspected to be cross-talk hits: All hits above the blue line are rejected.

One can also look at certain correlations between two OMs. If one OM (the "sender") produces a signal above a certain amplitude and another OM (the "receiver") has a signal during a time window around the other hit (at the sender OM), then one can assume that

this hit (at the receive OM) was produced by crosstalk. The values of the thresholds and the size of the time window are OM specific.

## 6.3 Retriggering

Since the hit cleaning procedure removes hits, some events do not satisfy the trigger requirements anymore. Therefore all events need to be checked again, whether they still satisfy either the multiplicity requirement or the string trigger requirement, otherwise these events are removed.

## 6.4 Reconstructions – First guess methods

The hit information that was recorded for an event is used to reconstruct the path of the particle that caused these hits. Here, one starts with so-called first-guess methods. They usually have only a limited accuracy, but provide a fast way to estimate whether an event comes from an up-going or down-going particle. This step is done early in the data processing cycle, so that one can remove a huge fraction of the background. The results of the first-guess methods are also used as seeds for more complex reconstruction methods.

The easiest first-guess method is comes from the linefit algorithm. The idea behind it is the minimization of the sum of the squares of the differences between the fitted function and actually occurring hits, e.g. for the x-coordinate $\sum_{n=0}^{N} \Delta_n^2 = \sum_{n=0}^{N} \left( x(t_n) - x_n \right)^2 = \min$ and

similar for the y- and z-coordinate. $N$ is the total number of hits, $n$ is the hit number, $x_n$ is the x-component of the coordinate where the hit occurred, and $t_n$ is the time at which it happened. The fitted function is $x(t) = v_x t + a_x$ with the open parameters $v_x$ and $a_x$. The minimization requires therefore

$$0 = \frac{d}{dv_x}\sum_{n=0}^{N}\Delta_n^2 = 2\sum_{n=0}^{N}(v_x t_n + a_x - x_n)t_n \rightarrow 0 = v_x\sum_{n=0}^{N}t_n^2 + a_x\sum_{n=0}^{N}t_n - \sum_{n=0}^{N}x_n t_n \text{ and}$$

$$0 = \frac{d}{da_x}\sum_{n=0}^{N}\Delta_n^2 = 2\sum_{n=0}^{N}(v_x t_n + a_x - x_n) \rightarrow 0 = v_x\sum_{n=0}^{N}t_n + Na_x - \sum_{n=0}^{N}x_n$$

The second equation can be solved for $a_x$ to get $a_x = \frac{1}{N}\sum_{n=0}^{N}x_n - \frac{1}{N}v_x\sum_{n=0}^{N}t_n$. Plugging this result into the first equation leads to $0 = v_x\sum_{n=0}^{N}t_n^2 + \frac{1}{N}\sum_{n=0}^{N}x_n\sum_{n=0}^{N}t_n - \frac{1}{N}v_x\left(\sum_{n=0}^{N}t_n\right)^2 - \sum_{n=0}^{N}x_n t_n$, which gives in return $v_x = \frac{\frac{1}{N}\sum_{n=0}^{N}x_n\sum_{n=0}^{N}t_n - \sum_{n=0}^{N}x_n t_n}{\frac{1}{N}\left(\sum_{n=0}^{N}t_n\right)^2 - \sum_{n=0}^{N}t_n^2}$. The same can be done for the other two coordinates. Finally the speed can be determined by $v = \sqrt{v_x^2 + v_y^2 + v_z^2}$. The zenith and azimuth angles under which the track goes through the detector are $\vartheta = \arccos\frac{v_z}{v}$ and $\varphi = \arctan\frac{v_y}{v_x}$. This method does not take the time into account that it takes for the Cherenkov light to reach the OM after it was emitted by the muon.

Other first-guess results can be achieved by the direct walk method,[99] the dipole fit method,[99] and the JAMS algorithm.[100]

## 6.5 Reconstructions – Maximum Likelihood method

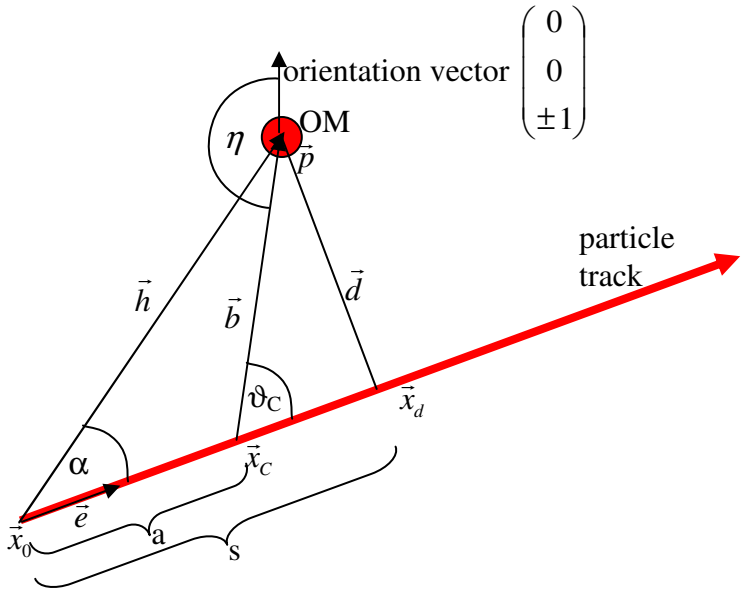


*Figure 24 Schematic for the calculation of the time residual*

The results of the first guess methods can be used as starting point for the much more sophisticated maximum likelihood reconstruction. Before this method can be explained, its most important quantity – the time residual – needs to be discussed (see Figure 24).

The time residual is the difference between the time $t_{hit}$ when a hit was recorded and the time $t_{expected}$ when the hit was expected if one tests a specific particle track hypothesis:

(82) $$t_{res} = t_{hit} - t_{expected}\,.$$

Assume an OM at a position $\vec{p}$ and a particle track hypothesis with a vertex $(\vec{x}_0, t_0)$ traveling in a direction with $\vartheta$ and $\varphi$ (the definition of the angles used by AMANDA is explained in Figure 25). These two angles give the unit vector $\vec{e}$ of the direction of track $\vec{e} = \begin{pmatrix} \sin\vartheta\cos\varphi \\ \sin\vartheta\sin\varphi \\ \cos\vartheta \end{pmatrix}$. If one also defines a vector $\vec{h} = \vec{p} - \vec{x}_0$, then $\vec{h}\vec{e} = |\vec{h}||\vec{e}|\cos\alpha = h\cos\alpha = s$ is the distance between the vertex $\vec{x}_0$ and the point of closest

approach $\vec{x}_d$ (see Figure 24). From there one can get $\vec{x}_d = \vec{x}_0 + s\vec{e}$, $\vec{d} = \vec{p} - \vec{x}_d$ and the closest approach distance $d = |\vec{d}|$. The particle traveling along this track emits Cherenkov light under an angle $\vartheta_C$. In order for the Cherenkov light to hit the OM it has to leave the track at the Cherenkov point $\vec{x}_C$. With this information one can calculate the two distances $a = s - \frac{|\vec{d}|}{\tan\vartheta_C}$ and $b = |\vec{b}| = \frac{|\vec{d}|}{\sin\vartheta_C}$. The particle speed can be approximated with $c$, and for the light traveling through the ice one takes $\frac{c}{n_G}$, so that the light reaches the OM at

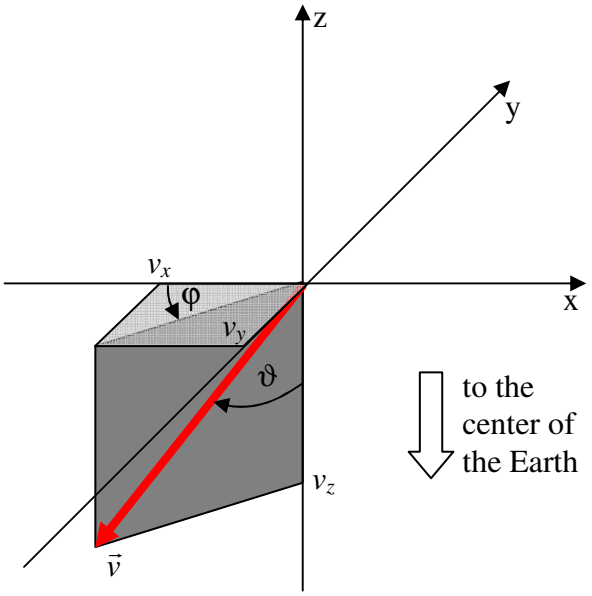


*Figure 25 Definition of the angles used by AMANDA*

(83) $$t_{expected} = t_0 + \frac{a}{c} + \frac{bn_G}{c}.$$

This value is used in (82).

If there wouldn't be any other effects, the time residual (82) would be zero, i.e. one would measure the hit at exactly at the time calculated with (83). There are two major causes of non-zero time residuals: the scattering of the Cherenkov light and the resolution of the OM. Both effects can be expressed in terms of a probability density function.

The AMANDA experiment uses the so-called Pandel function[101] as probability density function for scattering:

$$p_{Pandel}\left(t_{res(Pandel)}\right) = \frac{\alpha^{\beta} t_{res(Pandel)}^{\beta-1}}{\Gamma(\beta)} e^{-t_{res(Pandel)}\alpha} \tag{84}$$

with $\alpha = \frac{1}{\tau} + \frac{c}{n_G \lambda_a}$, $\beta = \frac{d_{eff}}{\lambda}$, $\tau = 557ns$, $\lambda = 33.3m$, the absorption length $\lambda_a = 98m$ and the effective closest approach distance $d_{eff} = 3.1m - 3.9m\cos\eta + 4.6m\cos^2\eta + 0.48d$. By using $d_{eff}$ instead of $d$ or $b$, one takes the geometry of the OM into account and the path which the light has to take around the OM. The angle $\eta$ is calculated by $\eta = \arccos\frac{(0 \quad 0 \quad \pm 1)\vec{b}}{|\vec{b}|} = \arccos\frac{\pm b_z}{|\vec{b}|}$, with $\vec{b} = \vec{h} - a\vec{e}$. The $\pm$ sign indicates the orientation of the OM, which is either up or down (out of the 680 OMs only 14 are oriented upward).

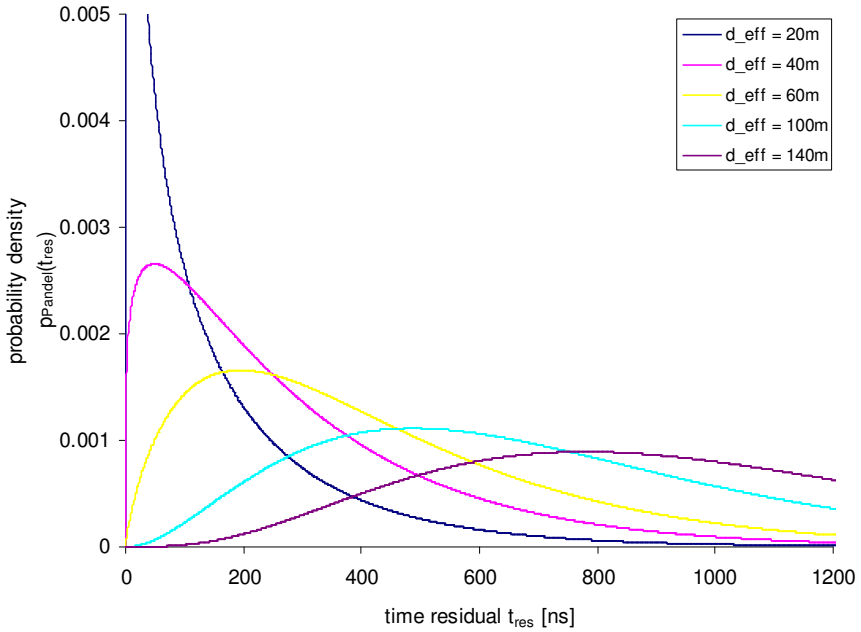


*Figure 26 Probability densities of the hit arrival as a function of the time residual for different effective distances*
These functions are not defined for negative time residuals, and have a pole at zero for effective distances smaller than 33.3m.

The probability density function of the OM resolution can be described by a Gaussian function: $p_{OM}\left(t_{res(OM)}\right)=\frac{1}{\sqrt{2\pi}\sigma}e^{-\frac{t_{res(OM)}^2}{2\sigma^2}}$, where $\sigma$ is the resolution of the OM. For the reconstruction, one has to use the total probability density function of the total time residual $t_{res}$, which has contributions from the two independent variables $t_{res(Pandel)}$ and $t_{res(OM)}$. Therefore the total probability density function is a convolution of their probability density functions: $p(t_{res})=(p_{Pandel}*p_{OM})(t_{res})=\int_0^{+\infty}p_{Pandel}(t')p_{OM}(t_{res}-t')dt'$.

The lower limit of the integral is set to zero, since a time residual smaller than zero has no meaning for the "pure" Pandel function (it would violate causality). However, the convoluted Pandel function is also defined for negative time residuals, since the limited resolution of the OM smears the arrival times. This convolution leads to a parabolic cylinder function, which can be described in terms of hypergeometric functions. The evaluation of these functions is very time consuming so that one uses either an approximation – the so-called patched Pandel function – or one solves this convolution integral numerically. The problem with a numeric solution is the pole of the Pandel function that comes from $t_{res}^{\beta-1}$ for $\beta<1$. In order to remove it, one can start with an integration by parts

$$
\begin{aligned}
p(t_{res}) &= \frac{\alpha^\beta}{\Gamma(\beta)\sqrt{2\pi}\sigma}\int_0^{+\infty}t'^{\beta-1}e^{-t'\alpha-\frac{(t_{res}-t')^2}{2\sigma^2}}dt' \\
&= \frac{\alpha^\beta}{\beta\Gamma(\beta)\sqrt{2\pi}\sigma}\left[t'^{\beta}e^{-t'\alpha-\frac{(t_{res}-t')^2}{2\sigma^2}}\Big|_0^{\infty}-\int_0^{+\infty}t'^{\beta}e^{-t'\alpha-\frac{(t_{res}-t')^2}{2\sigma^2}}\left(-\alpha+\tfrac{1}{\sigma^2}(t_{res}-t')\right)dt'\right] \\
&= \frac{\alpha^\beta}{\Gamma(\beta+1)\sqrt{2\pi}\sigma}\int_0^{+\infty}t'^{\beta}e^{-t'\alpha-\frac{(t_{res}-t')^2}{2\sigma^2}}\left(\alpha+\tfrac{1}{\sigma^2}(t'-t_{res})\right)dt'
\end{aligned}
$$

This integral does not have a pole anymore, so that it can easily be integrated numerically.

It turns out that there is almost no difference between the results obtained with the patched Pandel function and results obtained with the numerical solution of the convoluted Pandel function. The biggest differences can be found for low energy events if they are almost vertical upward going. Some results for the mean difference between the simulated and the reconstructed zenith angle for simulated atmospheric neutrinos are shown in Table 7.

| applied filter* for the analysis of … neutralinos with a (… annihilation channel) | mean zenith angle difference between the original simulated track and the reconstructed track using the … | |
|---|---|---|
| | patched Pandel function | convoluted Pandel function |
| 50GeV (soft) | 2.5 (3.8 ) | 2.3 (2.5) |
| 50GeV (hard) | 2.4 (3.7) | 2.3 (2.5) |
| 100GeV (soft) | 2.1 (3.3 ) | 2.0 (2.7) |
| 100GeV (hard) | 1.9 (2.1) | 1.9 (1.6) |
| 250GeV (soft) | 1.5 (1.7) | 1.5 (2.0) |
| 250GeV (hard) | 1.3 (1.5) | 1.2 (1.6) |
| 1000GeV (soft) | 1.2 (1.4) | 1.2 (1.5) |
| 1000GeV (hard) | 1.0 (1.3) | 1.0 (1.2) |
| 5000GeV (soft) | 1.0 (1.3) | 1.0 (1.1) |
| 5000GeV (hard) | 0.9 (1.1) | 0.9 (1.0) |

*Table 7 Mean zenith angle differences between the original simulated track and the reconstructed track using the patched Pandel function and the convoluted Pandel function.*
The numbers in parenthesis are the values found if only simulated tracks between 175° and 180° are considered; the numbers outside of the parenthesis are the values found for simulated tracks between 150° and 180°.
*The different filters will be explained in the next chapter.

There is another component of the probability density, which has not been considered yet: Noise, which is produced by the OMs. The noise rate for AMANDA is approximately $\lambda = 5 \cdot 10^{-7}\,\mathrm{ns}^{-1}$. The (Poisson) probability to get at least one noise hit

within a time $T$ is $P(n \geq 1) = 1 - P(0) = 1 - e^{-\lambda T} \approx \lambda T$. The probability density is therefore $p(n \geq 1) = \frac{dP}{dT} = \lambda$, which is added to the probability density of the time residual.

The idea behind the maximum likelihood method is to find a track for which the measured hit times have the highest likelihood (or highest probability density). There are six free parameters (3 – vertex position, 1 – time, 2 – direction) that can be adjusted, however, only 5 of them are independent, so that one parameter can always kept constant. The SIMPLEX algorithm (which is an optimization method used by the reconstruction program) scans this 5-dimensional parameter space to find a parameter combination with the highest likelihood. This is usually done by starting with a hypothesis which comes from a first guess method. Afterwards, the track hypothesis parameters are slightly varied in different directions of the parameter space. The SIMPLEX algorithm compares the different likelihoods and uses this information to "decide" which region of the parameter space should be scanned next in order to find the maximum of the likelihood. This procedure can be done either for a fixed number of steps or until the set of track parameters converges, i.e. does not change much anymore even with additional steps.

A more advanced method repeats the previous step multiple times.[99] It does it by testing a fixed number of combinations of the two angles. If one iteration gives a higher probability than the previous one, the result of this iteration is used as basis for the next iteration with a new angle combination. While the track vertex is shifted along the new track to a point which is closest to the center of gravity of the hit, the time (at the track vertex) is adjusted so that it is consistent with the hit times (by taking into account that

the Cherenkov light needs some time from the vertex to reach the OMs). The parameter combination which achieves the highest probability is used as final result.

As one can see, the goal of these procedures is finding an extremum of the probability density. For practical purposes this is usually the minimum of the negative of the logarithm of the probability density. There is, however, a strong possibility that these procedures do not find the (desired) global minimum, but get caught in some local minimum. This is one of the reasons that there is always the danger of getting misreconstructed tracks. An even stronger reason for misreconstruction comes from the scattering of the Cherenkov light. Even though the scattering probability can be calculated, scattering is the biggest source of misreconstructed events. Since the probability distributions do not have strong peaks in most cases, there is a strong uncertainty about the expected time residual. Another reason for getting misreconstructed tracks is a bad quality of hits (e.g. too few hits, insufficient hit cleaning). Events which consist of two particle tracks can also lead to a misreconstruction. In order to remove these misreconstructed events, one can analyze the so-called quality parameters, which are discussed in the next chapter.

This analysis has to focus on events which go almost vertically upward along the string. The reconstruction of these events is more difficult, because there is usually almost no lever from other strings to help to determine the right zenith angle (and it is even more difficult – if not impossible – to reconstruct the azimuth angle, which is not needed for this analysis). The reconstruction tends to push these kinds of tracks too close to the

vertical. While this problem leads to inaccuracies in the determination of the zenith angle, the impact on the anaysis should be small, since the experimental and simulated events are affected in the same way (and only an excess of measured events over the expected [i.e. simulated] number of events may indicate a signal).

# Chapter 7: The initial analysis

For any data analysis there is always the danger that one introduces a bias towards a particular result. Therefore it is desirable to do all steps of the analysis without seeing the final result, i.e. being blind to the outcome of the analysis. This is a way to ensure that actions taken in the course of the analysis are not done (consciously or unconsciously) in order to achieve a particular result. This causes a problem in this particular analysis, since some of the steps are done to check whether all misreconstructed atmospheric muons are gone. Since the simulated atmospheric muons are not a reliable tool (they can only be used as a guide), there is no other option than looking at the "real" data. However, in order to have at least some sort of blindness, only a small fraction (20%) of the entire data set is used for this initial analysis. The results are collected and presented to the IceCube collaboration with the request to open the remaining data. Once everything is satisfactory, this request is granted and the remaining fraction (80%) of the data can be used for the final analysis. This last step is called "unblinding". At this point the setup of the analysis cannot be changed anymore, since this would violate the goal of being blind to the final outcome.

## 7.1 Data Sets

### 7.1.1 Experimental Data

This analysis uses data collected with the AMANDA neutrino telescope for the years 2001 to 2003. This data is stored in about a 100,000 files, and each file contains about 30,000 events. Only "good" files – i.e. files which were generated at a time for which we know that the hardware and software was working within acceptable parameters – were used. The detector is constantly monitored from the northern hemisphere, so that anomalous behaviors of the hardware/software will be recorded and may cause some files to be discarded.

The total live time of the entire available data set is 638 days. The data set which is selected for the unblinding proposal consists of all runs with the run numbers ending with 5 or 0, so that one gets about 20% of the total data set. This 20% of the data correspond to a live time of 120 days; the still blind 80% have a live time of 518 days (see Table 8).

| | 20% of the data | | | | 80% of the data | | | |
|---|---|---|---|---|---|---|---|---|
| | number of runs | number of files | number of events (at trigger level) | live time | number of runs | number of files | number of events (at trigger level) | live time |
| 2001 | 45 | 7634 | 362 072 753 | 3816511.7s (44.2d) | 187 | 30 631 | 1 456 377 895 | 15447088.8s (178.8d) |
| 2002 | 40 | 5219 | 259 372 458 | 2935527.9s (34.0d) | 184 | 22 784 | 1 129 001 018 | 12825775.3s (148.4d) |
| 2003 | 56 | 6120 | 312 270 092 | 3632908.6s (42.0d) | 239 | 27 760 | 1 418 169 065 | 16500221.8s (191.0d) |

*Table 8 Life time and data sets used for 2001-2003*

### 7.1.2 Simulated Data[102]

Naturally, reconstructing an experimental track does not reveal the nature of the particle (i.e. whether it is a muon caused by an atmospheric neutrino, or perhaps a muon caused by a neutrino that comes from a neutralino annihilation), nor does it give a hint whether it has been misreconstructed. The only way to learn more about the particles of a given experimental data set is to compare the distributions of certain parameters of these particles with the parameter distributions of particles of simulated data sets for which the "origin" is known. Also, the parameter distributions and the overall number of events depend on the particular cuts which are applied. Without the use of simulated data sets (to which the same cuts are applied), it would be impossible to predict how particular parameter distributions change with different cut settings or whether the total number of events is consistent with the number of expected events.

The background simulation consists of two parts: atmospheric muons (done with dCorsika version 6.020 – a program developed for AMANDA which generates air shower)[103] and atmospheric neutrinos (done with ANIS version 1.8.1 – an "All Neutrino Interaction Generator" written for AMANDA).[89] ANIS is also responsible for the simulation of the muons coming from the interaction of the atmospheric neutrinos with the nuclei near the detector.

Each dCorsika file contains $1 \cdot 10^6$ events (at generator level) which corresponds to 66.1682s. The total live-time simulated with dCorsika is therefore 66.1682s times the number of files. ANIS files have a weight attached to each event, so that the sum of all (weighted) events in one file corresponds to the total number of atmospheric neutrinos

per year. In order to bring them to the real live-time provided above, one has to scale each event by a factor, which is given in Table 9.

| | dCorsika files | | | ANIS files | | |
|---|---|---|---|---|---|---|
| | number of files | time they correspond to | factor each event has to be weighted with | number of files | time they correspond to | factor each event has to be weighted with |
| 2001 | 6007 | 397 472.377s (4.6d) | 9.6020 | 500 | 500yrs | 2.4204158e-4 |
| 2002 | 6010 | 397 670.882s (4.6d) | 7.3818 | 500 | 500yrs | 1.8616996e-4 |
| 2003 | 6010 | 397 670.882s (4.6d) | 9.1355 | 500 | 500yrs | 2.3039755e-4 |

*Table 9 Simulated data sets (dCorsika and ANIS)*

The signal was simulated with WimpSimp (version 1.2),[104] which generates neutrinos from neutralino annihilation (after the annihilation products decay). Of course, the neutralino properties (mass, composition, annihilation channels, etc.) are not known yet. Therefore seven different neutralino energies (50GeV, 100GeV, 250GeV, 500GeV, 1000GeV, 3000GeV, 5000GeV) with two annihilation channels each (soft: $b\bar{b}$, hard: $W^+W^-$ [$\tau^+\tau^-$ for 50GeV]) were simulated. The annihilation products decay further; and a fraction of the decay products are neutrinos. Their interactions with nucleons near the detector were simulated with Genniup.[105]

Muons that have been created by the above-mentioned procedures are propagated through the ice by MMC (version 1.2).[106] This program takes care of all their interactions with the surrounding ice such as ionization, bremsstrahlung, direct pair-production, photo-nuclear reactions and decay. MMC also simulates the electromagnetic and hadronic showers that are created by these interactions.

The detector response to these muons (and its associated particles from its propagation through the ice) is simulated by AMASIM (version 2.76.02 grapefruit-fix3 St 08/14).[107] The first step that needs to be simulated is the propagation of the Cherenkov light through the ice.

Since it would be too time consuming to do this for every single photon, tables were created which contain the mean amplitude and the arrival time distribution depending on the distance between the photomultipliers and the position where the photon was emitted.[107] These tables were generated by the Photon Transportation and Detection Program (PTD), which simulates the scattering and absorption of the photons in the ice.[108] The mean amplitude on each PMT is used to get a random discrete number of photoelectrons (where a Poisson distribution is used). For each photoelectron a random arrival time is calculated based on the probability distribution function given by the PTD table.

For an accurate simulation of the photon propagation, the ice properties need to be taken into account. It was found that the ice at the glacier consists of several layers with different optical properties such as absorption length and scattering length. The differences come especially from varying concentrations of bubbles and dust deposited into the ice millennia ago (the ice of the detector is up to 100,000 years old). The tables which were used for the simulations of this analysis are based on the Modified Absorption Model (MAM) with four different ice layers.

The next step in the detector simulation is the hardware response: AMASIM simulates the pulse readouts for each optical module, and it also including the effects arising from

the cable length. Furthermore it simulates pulses arising from the dark noise of the photomultipliers.

## 7.2 Overview of the analysis

The goal of this analysis is the search for muons coming from neutrinos caused by WIMP annihilations inside Earth. An essential part of the analysis is finding cuts that optimize the sensitivity by removing as much simulated background as possible while keeping as many simulated signals as possible. These cuts are also applied to 20% of the data of 2001 to 2003, and the remaining events are compared with the expected (simulated) background.

Both data and MC samples have been subjected to the filter steps mentioned in the previous section, such as hit cleaning, retriggering, flare checking (see 7.3.3), various reconstruction steps, and a zenith angle cut at 150°. This zenith angle of 150° has been chosen to remove a big fraction of the background while keeping a significant portion of the off-signal region. The signal region starts at an angle of about 170° depending on the WIMP mass. The off-signal region is of importance since it increases the background statistics and makes it possible to check for consistency between data and predicted background and to ensure that all atmospheric muons are gone.

The remaining background events (atm. neutrinos and misreconstructed atm. muons) and WIMP signals are subjected to cuts using 7 different cut variables, including an

additional zenith angle cut to separate the signal region from the off-signal region. The cuts are chosen to remove all misreconstructed atmospheric muons, and to find the best sensitivity. A multidimensional analysis was attempted, i.e. all cuts are done simultaneously for all cut variables. However, differences between simulated and experimental atmospheric muons put strong restrictions on this method, so that only two of these variables were optimized automatically. The remaining five cutvariables had to be adjusted by hand to counteract the contamination by misreconstructed atmospheric muons. Further explanations to this issue can be found below. The cuts have been optimized for seven different WIMP masses with two annihilation channels each.

## 7.3 Data Filtering

### 7.3.1 L1/L2[109]

The first steps of most AMANDA analysis chains include the so-called Level 1 and Level 2 filtering (L1/L2), which take care of calibration, "bad OM cleaning", hit cleaning (noise, cross talk) and reconstructions (first guess methods and muon likelihood fit [32 iterations]). These two steps were done with Sieglinde, which is a software package designed for processing of AMANDA data. L1 uses the Sieglinde version 1.5.1p5-rc2 together with ROOT 3.10.2 (ROOT is another software package which is used for data analysis and is provided by CERN), while L2 uses a Sieglinde version with the time stamp of Nov 11, 2005 together with ROOT 4.00.08f. Additionally, a retriggering was

performed with the new multiplicities calculated in L1/L2. All these procedures were discussed in detail in the section about the AMANDA detector.

### 7.3.2 Initial zenith angle cut

A cut on the zenith angle of 150° (based on the muon likelihood fit with 32 iterations) was applied to reduce the amount of data. This zenith angle of 150° is far away from the signal region, so that a significant portion of the off-signal region remains. This off-signal region is useful since it provides an extended zenith region outside the signal region to check whether data and predicted background matches (and all misreconstructed atmospheric muons were removed).

### 7.3.3 Flare checking

The goal of this step is the removal of events which were not caused by particles, but were triggered by other reasons which are in general unknown. These events are called "flares". The procedure to remove them is done as suggested by Arvid Pohl.[110] There are 9 different so-called flare indicators which are calculated from the number of hits with specific properties, e.g. hits which are shorter than a particular value, hits with missing edges, or hits that were recorded on channels with twisted pair and coaxial cables. All flare indicators are put into a logarithmic histogram. The distribution should be exponential (i. e. linear in a logarithmic plot), while the non-exponential tail comes from non-particle events.[110] An exponential fit is done on each plot. At the intercept of this function with 1 a cut-off for this flare indicator is set. All fits are done simultaneously.

After applying all cut-offs to the data, only the exponential parts of the histograms are left, and all non-particle events should (hopefully) be gone. These cuts are also applied to the MC samples. The flare indicators #3, #4 and #7 were not used for this analysis because their histograms were too diffuse, but the remaining cuts were sufficient to remove all non-exponential tails from the flare indicator histograms.

| | flare indicator #5 | flare indicator #8 |
|---|---|---|
| before | 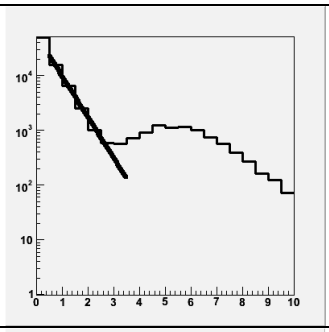 | 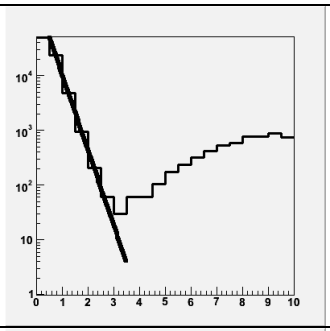 |
| after | 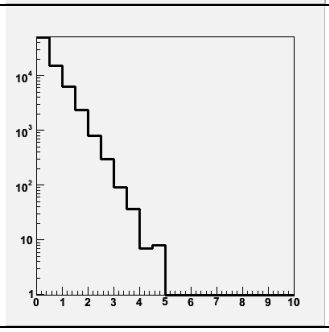 | 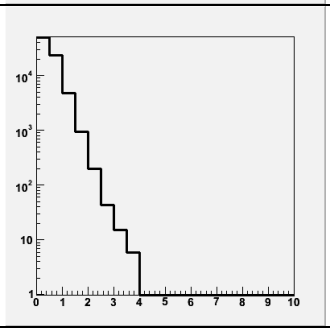 |

*Table 10 Example of two flare indicators before and after flare checking*

## 7.4 Analysis

### 7.4.1 Cut Parameters

A total of 20 cut parameters were considered:

| # | Name | lower limit | upper limit |
|---|---|---|---|
| 0 | Ndir (Number of direct hits) | fixed at 9 (13 for 250GeV and higher) | (N) |
| 1 | Nall (Number of all hits/Number of hit channels) | (O) | (O) |
| 2 | Nstr (Number of hit strings) | (N) | (N) |
| 3 | Ndir/Nall | fixed at<br>0.55 for 50GeV(soft)<br>0.5 for 50GeV(hard), 100GeV<br>0.45 for 250GeV, 500GeV(soft), 1000GeV(soft)<br>0.3 for 500GeV(hard), 1000GeV(hard) and higher | fixed at 1.0 |
| 4 | Sall (Smoothness with respect to all hits) | (N) | (N) |
| 5 | Sdir (Smoothness with respect to direct hits) | (N) | (N) |
| 6 | Ldir (Direct length) | (O) | (O) |
| 7 | Steepness of the Minimum of MuonLLH fit (32 iterations) | (N) | (N) |
| 8 | Reduced Likelihood of the MuonLLH fit (32 iterations) | (N) | (N) |
| 9 | Number of hits on string w/ highest Nhit | fixed at 10 (9 for 50GeV, 100GeV(soft)) | (N) |
| 10 | Space angle difference (MuonLLH fit (32 iterations) compared to MuonLLH (simple fit)) | (N) | (N) |
| 11 | Reduced Likelihood difference between MuonLLH (32 iterations) and zenith weighted MuonLLH | (N) | (N) |
| 12 | Reduced Likelihood difference between MuonLLH (32 iterations) and CascadeLLH | (N) | (N) |
| 13 | Center of Gravity - z component | fixed at -100 | (N) |
| 14 | Linifit velocity | (N) | (N) |
| 15 | Reduced Chi2 of z direction for Linefit | (N) | (N) |
| 16 | String with highest Nhit: dz/dt (z-position and hit time) for strings with 8 or less hit channels | (N) | (N) |
| 17 | String with highest Nhit: error of dz/dt | (N) | (N) |
| 18 | String with highest Nhit: sum of time differences (t_(i) - t_(i-1)) for hits (i) which are in 'wrong' order | (N) | (N) |
| 19 | String with highest Nhit: number of hits which are in 'wrong' order / number of hits on string | fixed at 0.0 | fixed at<br>0.2 for 50GeV, 100GeV<br>0.4 for 250GeV(soft) 500GeV(soft)<br>0.5 for 250GeV(hard), 500GeV(hard) and higher |

*Table 11 Cutparameters considered for this analysis*
(O) These cuts are optimized, i.e. the cuts are determined by the minimizer.
(N) No cuts.

7.4.1.1 Explanation for parameters #1, #3, #5, #6 (parameters related to direct hits)

These parameters make use of the direct hits. Direct hits are hits which are assumed to arrive at the OM without scattering, so that a high number of direct hits (i.e. only negligible scattering) can be seen as an indication for a high quality reconstruction. For this analysis a hit is considered to be a direct hit if its time residual (with respect to the track of the maximum likelihood reconstruction) is between -25ns and +75ns. The window -25ns/+75ns was chosen to get a high enough number of eligible hits, but not too high to lose the distinction to the regular hits.

While #1 Ndir is the number of direct hits, #3 Ndir/Nall stands for the number of direct hits divided by the number of all hits. #5 Sdir stands for the smoothness (see below) with respect to direct hits. In order to calculate the direct length (#6 Ldir), all direct hits are projected on to the track. The direct length is the biggest distance between two such projections of the direct hits on the track. The direct hits which are used for Ldir are chosen from a smaller window for the time residual (-25ns/+25ns), which turned out to make it easier to distinguish the Ldir distribution of the background from the signal distribution.

7.4.1.2 Explanation for parameters #4, #5 (parameters related to smoothness)

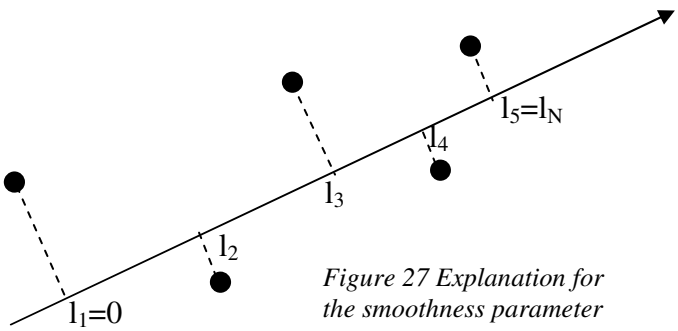


*Figure 27 Explanation for the smoothness parameter*

Smoothness S is a measure on the distribution of hits along the track. It is defined as $S = \max(S_i)$ with $S_i = \frac{i-1}{N-1} - \frac{l_i}{l_N}$, where $i$ is the $i$-th

hit along the track, $N$ is the total number of hits, and $l_i$ is the distance along the track between the projection of the first hit OM on the track and the projection of the $i$-th hit OM on the track.[94]

#### 7.4.1.3 Explanation for parameter #7 (steepness of the minimum of the LLH reconstruction)

The track was reconstructed by the maximum likelihood method. As explained before, the reconstructed track was selected based on its probability with respect to the time residuals and the noise rate, i.e. the track with the lowest $L$: the negative of the logarithm of the probability density is selected. In other words: the track in question lies in a minimum of $L$, which is a function of track parameters such as the direction. An interesting quality parameter can be derived when the neighborhood of this minimum is scanned. The region surrounding this minimum of $L$ can be fitted with an elliptical paraboloid (done by the I3MuonLLH fitter) to learn something about its properties. In order to do this, a three dimensional coordinate system is considered, with the x and y axis being the two angles of the particle track direction and the z axis the likelihood. The minimum of the likelihood is at $x = y = 0$. The equation which describes the minimum has the form $L(r,\varepsilon) = L_{\min} + a(r\cos(\varepsilon - \varepsilon_0))^2 + b(r\sin(\varepsilon - \varepsilon_0))^2$, where $r$ and $\varepsilon$ are the distance and the angle measured from the minimum (in the x-y plane); $a$, $b$ and $\varepsilon_0$ are the parameters that are fitted.

The paraboloid is checked at a distance $\Delta L = 1$ above its minimum. At this height the cross section describes an ellipse with the equation $1 = a \cdot x^2 + b \cdot y^2$, where x and y are the coordinates of the original plane after a rotation about $\varepsilon_0$. The area of this ellipse is

$\pi/\sqrt{a \cdot b}$ . The area provides a measure of the steepness of the minimum. The smaller the area (at a distance of 1 above the minimum), the steeper the "walls" of the minimum are, the better the minimum is localized.

7.4.1.4 Explanation for parameter #8 (reduced likelihood)

The reduced likelihood is calculated by $L_{reduced} = \frac{L}{n-5}$, where $L$ is the negative of the logarithm of the probability density calculated for this track during the reconstruction process, and $n$ is the number of hits. 5 represent the number of independent track parameters (direction, vertex position, time), so that *n-5* stands for the degree of freedom.

7.4.1.5 Explanation for parameters #16 - #19 (hit distribution on the string with the highest number of hits)

For the parameters #16 - #19 one looks at hits on the string with the highest number of hits, and considers only the first hits (if one OM is hit more than once). Parameter #16 represents the slope of the (fitted) function hit time vs. z-position of the OM. Parameter #17 is the error of this slope. Going upwards on the string one checks, whether every subsequent hit has a larger hit time than the previous hit. The number of hits for which this is not the case is represented by the parameter #19. Furthermore all time differences between the hit times of these 'wrong' hits and the hit times of the hits before them are added (#18).

| *#1 Nall* | *#3 Ndir/Nall* | *#6 Ldir* |
|---|---|---|
| 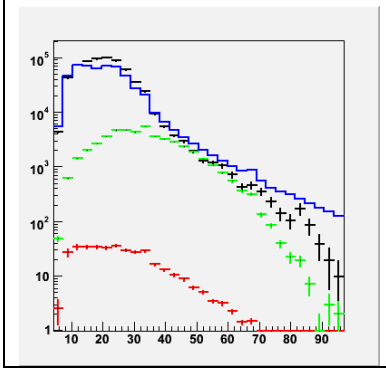 | 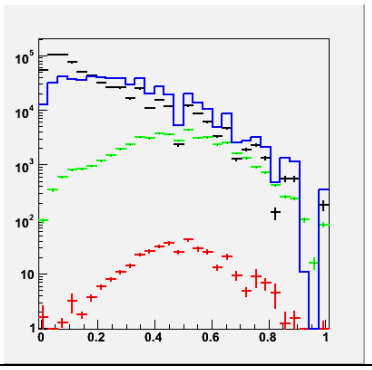 | 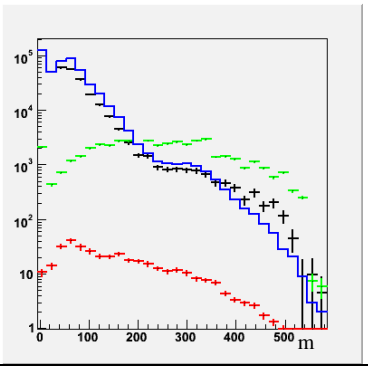 |

*Table 12 Examples of cut parameter distributions before cuts for1000GeV (soft)*
atmospheric muons, atmospheric neutrinos, neutralino signals, data

Unfortunately, there are some variables which have some known problems, i.e. the simulation does not seem to agree with reality. This can be revealed by making a comparison of the distribution of this cut parameter (before cuts) between the simulated atmospheric muons and the experimental data. Before any further cut besides L1/L2 is applied, most of the experimental data should consist of misreconstructed atmospheric muons, so that both distributions should match. However, this is not the case for the variable concerning the z-component of the center of gravity of all the hits. This problem arises most likely from the effects of the ice model (dust layers, etc.), which are still not well understood. For the particular case of the center of gravity, a hard cut at $z$ = -100m (see Figure 19 for AMANDA's coordinate system) has been used, since the effect seems to worsen for lower depths. It is interesting to note, that after all cuts were applied, there seems to be an agreement for this parameter between simulated atmospheric neutrinos and data, which should consist only of atmospheric neutrinos (see next chapter for more details).

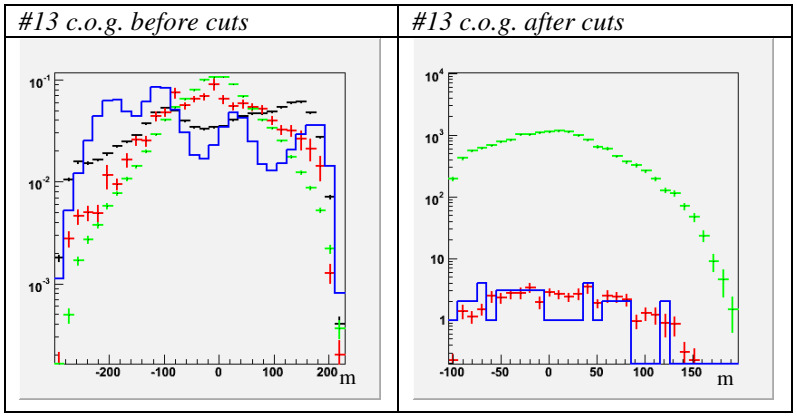


*Table 13 Center of gravity cut parameter distributions before and after cuts for1000GeV (soft)*
atmospheric muons, atmospheric neutrinos, neutralino signals, data
All distributions of the first histogram have been normalized to 1 in order make the differences between data and simulated atmospheric muons more visible.

Another problematic variable is the number of direct hits. Since this is one of the most powerful cut parameters, it was not possible to avoid using it. As in the case before, the simulated atmospheric neutrinos matched the distribution of the experimental data after all cuts were applied; the cuts may have simply removed all artifacts which led to the disagreements between data and simulation.

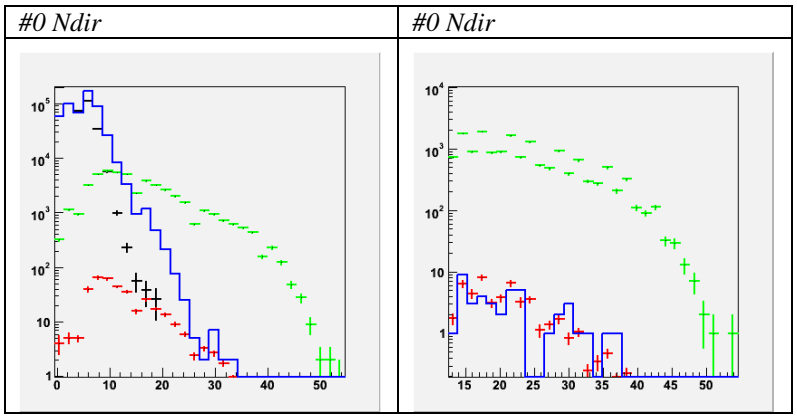


*Table 14 Ndir cut parameter distributions before and after cuts for1000GeV (soft)*
atmospheric muons, atmospheric neutrinos, neutralino signals, data

### 7.4.2 Upper Limit

Consider a known mean background $b$ and an observed number of events $n$. This information can be used to find an upper limit on the (unknown) signal mean $N_{90}(b,n)$ for a confidence level of 90%. The method by Feldman and Cousins was used for this analysis.[111]

One starts with the construction of an acceptance interval ($n_1$,$n_2$) for the number of measured events $n$ provided one has a known background $b$, and some signal mean $s$. For this analysis a confidence level of 90% is used. This implies that the acceptance interval ($n_1$,$n_2$) needs to be constructed in such a way that there is a 90% probability that $n_1 \le n \le n_2$. Theoretically, there are many ways to construct such an interval. The only requirement is that $\sum_{n=n_1}^{n_2} p(n) = 90\%$, i.e. the sum of the probabilities of all possible numbers of events occurring within $n_1$ and $n_2$ needs to be 90%.

The approach of Feldman and Cousins involves an ordering scheme which determines in which order the acceptance interval is built with different values of $n$ (see Figure 28). The Poisson probability to measure $n$ events for a mean background $b$ and a signal mean $s$ is $p(n,b,s) = (b+s)^n \frac{e^{-(b+s)}}{n!}$. This is repeated for other signal means to find an $s_{best}$ for which $p(n,b,s_{best})$ has the highest value. This is of course $s_{best}$=$n$-$b$ (or 0 if this difference becomes negative). Finally one calculates the ratio $R=p(n,b,s)/p(n,b,s_{best})$. This step is repeated for a range of different $n$ for the same particular $s$ and $b$. Each time one

calculates $p(n,b,s)$ and $R$. Now the acceptance interval for this particular signal mean $s$ and mean background $b$ can be built. One starts with the $n$ which achieved the highest $R$, then one goes to the second highest $R$, third highest $R$, and so on. This is done until the sum of all used $p(n,b,s)$ equals the confidence level (in this case 90%). The values of $n$ found by this procedure fill one horizontal line in Figure 28.

Such an acceptance interval must be constructed for a wide range of different signal means $s$ (and a constant mean background $b$). This procedure creates a confidence belt in the n-s plane with a lower and upper limit on the signal $s$ (see Figure 28). Once this is done, one can take a particular number of observed events $n$ to get the upper limit on the signal mean $s$ for this particular $n$. The upper limit of the signal mean is the highest value of $s$ which is still covered by an acceptance interval for this value of $n$. The upper limit of the signal mean for this mean background $b$ and the number of observed events $n$ will be denoted as $N_{90}(b,n)$.

| $n$ | $p(n,b,s)$ for $b$=3 and $s$=2 | $s_{best}$ for $b$=3 | $p(n,b,s_{best})$ for $b$=3 | $R$ | order |
|---|---|---|---|---|---|
| 0 | 0.0067 | 0 | 0.0498 | 0.14 | |
| 1 | 0.0337 | 0 | 0.1494 | 0.23 | |
| 2 | 0.0842 | 0 | 0.2240 | 0.38 | 7 |
| 3 | 0.1404 | 0 | 0.2240 | 0.63 | 5 |
| 4 | 0.1754 | 1 | 0.1954 | 0.90 | 3 |
| 5 | 0.1754 | 2 | 0.1755 | 1.00 | 1 |
| 6 | 0.1462 | 3 | 0.1606 | 0.91 | 2 |
| 7 | 0.1044 | 4 | 0.1490 | 0.70 | 4 |
| 8 | 0.0653 | 5 | 0.1396 | 0.47 | 6 |
| 9 | 0.0363 | 6 | 0.1318 | 0.28 | 8 |
| 10 | 0.0181 | 7 | 0.1251 | 0.14 | |

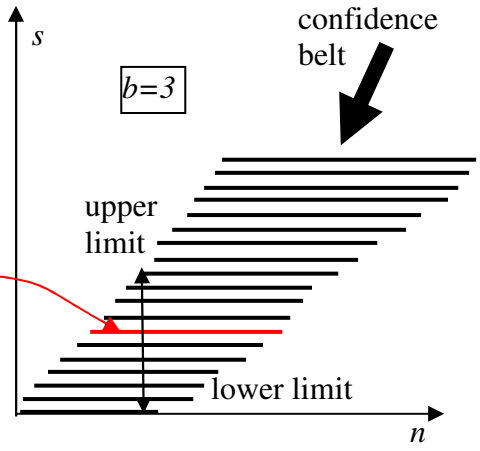


*Figure 28 Construction of the confidence belt with the Feldman-Cousins method*

Summing up all $p(n,b,s)$ for $n$=2...9 gives a total probability of 0.9 for the fixed background mean $b$=3 and the chosen signal mean $s$=2. This means that the acceptance interval for this particular signal mean and background goes from 2 to 9. The acceptance intervals for other signal means are not calculated here, they are drawn only illustrate the principle. While the number of observed events $n$ can only be positive integers (and zero), the signal mean $s$ and the mean background $b$ can be any positive real number (and zero).

### 7.4.3 Model rejection factor

Let's assume an arbitrary number of signals $s_{gen}$ originating from WIMP annihilation. It will become clear later that the final result does not depend on the actual number of $s_{gen}$ (and one would not know it anyway). These signals are put through all steps of the detector simulation and all filter steps and cuts are applied (the same cuts which are also applied on the simulated background and the experimental data). The resulting number $s$ stands for the number of signals that could have been observed provided $s_{gen}$ signals were indeed produced. The values $b$ and $n$ stand for the number of expected background events and the number of experimental observed events. These two numbers $b$ and $n$ give an upper limit on the signal mean $N_{90}(b,n)$ for a 90% confidence level as explained in the previous paragraph.

The ratio between the upper limit on the signal $N_{90}(b,n)$ that *may* have been detected and the number of signals *s* which *should* have been detected and survived all cuts (if $s_{gen}$ signals were produced) is used to limit the number of hypothetical signals which *may* have actually been produced $s_{90}$: $s_{90} = s_{gen} \cdot N_{90} / s$. In other words, not more than the fraction $N_{90} / s$ of the generated signal $s_{gen}$ could have been produced in reality with the given numbers of the background and the observed events. One can see that this ratio $N_{90} / s$ puts constraints on the model of the signal production.

For instance one can generate $s_{gen}=1000$ signals; $s=100$ signals survive the detector response simulation and all cuts. The expected background is $b=3.2$ and the number of observed events is $n=5$. This leads to an upper limit on the signal of $N_{90}(b,n) = 6.79$ – not more than 6.79 signals *could* have been detected. However, 100 signals *should* have been observed (if 1000 signals were produced). That means that not more than a small percentage ($N_{90} / s$ = 6.79 / 100 = 6.79%) of the generated signals *could* have been produced, i.e. $s_{90}$=67.9 signals.

Now it should also be clear that it does not matter which value is chosen for the number of generated events $s_{gen}$: If one uses a *c* times higher value, the number of signals *s* that survive all cuts will also be higher by a factor of *c*. In the calculation of $s_{90}$ this factor *c* gets cancelled: $s_{90} = cs_{gen} \cdot N_{90} / cs = s_{gen} \cdot N_{90} / s$.

In order to put the strongest constraints on $s_{90}$, one has to find a cut selection that minimizes the ratio $N_{90}(b,n) / s$. However, $N_{90}(b,n)$ depends on the number of observed

events, which is not known before unblinding. Therefore one uses an average upper limit (Feldman and Cousins call it sensitivity),[112] where one uses the upper limits of all possible numbers of observed events weighted by their Poisson probabilities under the assumption that there is no signal (*s=0*). $\overline{N}_{90}(b) = \sum_{n=0}^{\infty} N_{90}(n,b) \cdot b^n \frac{e^{-b}}{n!}$. This average upper limit $\overline{N}_{90}(b)$ replaces $N_{90}(b,n)$, so that the new ratio that should be minimized is now $\overline{N}_{90}(b)/s$. This ratio is called model rejection factor.

### 7.4.4 Finding the cut settings

The SIMPLEX algorithm and the TMinuit class of the ROOT software package were used to minimize the model rejection factor (MRF). This is used to determine a combination of cut parameters, that leaves the best combination of simulated background and signals to achieve the lowest MRF. This procedure is performed with respect to each individual WIMP mass/channel.

The minimizer uses only the MC samples (signals, atm. neutrinos, atm. muons) to find the minimum. The data sets of all three years were combined to get a higher number of events for the consistency check between simulated and experimental data, which done after the cuts are applied (see also 7.4.5). Since the MRF has to be minimized in such a way that it gives the best results for the still blind sample (remaining 80%) of the experimental data, each simulated event is reweighted with respect to the live time of the 80% of the data separately for each year. For instance, an atmospheric neutrino of 2001

has a weight of 0.1 for the live time of 20% of the data (which corresponds to 42 days), while the 80% had a live time of 191 days. This gives a factor of 4.5, so that a neutrino weight of 0.45 is used for the minimization. A similar calculation is done for atm. muons. The situation for the WIMP signals is different, since their weight is arbitrarily (the flux is unknown). The numbers of WIMPs are weighted according to the length of the live time (of the 80% data set) of each year, i.e. each signal is multiplied by the live time of this particular year divided by the average live time. The live time of the 80% data sample of 2003 is 191 days while the average live time is 172.7 so that this factor is 1.1 for 2003.

The minimizer works in the following way: It starts with a set of upper and lower boundaries (i.e. the seed) of the used cut parameters. For this set it counts the remaining background $b$ and signal events $s$ after applying all cut parameters on the atmospheric muons, atmospheric neutrinos and WIMP signals at the same time (global optimization). From this information it calculates the MRF. With the help of the SIMPLEX algorithm, other combinations of upper and lower boundaries of the cut parameters are tested until the maximum number of iterations has been reached or until the MRF converges. The combination of upper and lower boundaries which achieves the lowest MRF is kept, and the remaining events after applying these cuts are recorded.

The zenith angle is used as an additional cut parameter to separate the signal region from the off-signal region, but both results – with and without zenith angle cut – are recorded. This is done to get a comparison between expected background and data in the off-signal region, and to increase the statistics of background events.

Finally these cuts are applied to the (20% of the) data and compared to the MC samples (with the original scaling with respect to the live time of 20% of the data).

After the cuts are applied, the remaining MC background consists only of atmospheric neutrinos. That means, that the remaining experimental data sample is supposed to contain only atmospheric neutrinos (if no signal is present). There are, however, two problems: The first problem comes from the limited statistics on the MC atmospheric muons. Each simulated event carries a weight of about 7 to 10 (depending on the year), which reduces the accuracy of any prediction with regard to the remaining number of atmospheric muons. The other problem comes from the fact that certain aspects of the MC atmospheric muons are not simulated accurately enough, so that there are differences between MC and data. The minimizer is able to eliminate all MC atmospheric muons, but it does not know that there are in fact some misreconstructed atmospheric muons with (cut) parameters which are not represented by MC muons. These atmospheric muons survive. In other words, the remaining data is still contaminated by misreconstructed downward going muons, even though there are no MC atmospheric muons left. In order to remove these muons, one has to find cut variables where one can identify regions in the data distributions which differ from those of the simulated atmospheric neutrinos. If these are regions which are most likely caused by misreconstructed atm. muons (such as low numbers of Ndir), they are removed by setting certain cuts manually (see table above). Afterwards, the MRF minimization procedure is repeated.

It turned out that setting cuts manually to eliminate misreconstructed atmospheric muons is not an easy task, especially since differences between MC and data show up in a number of cut parameter distributions, and all these parameters have very complex relationships. Only a few variables were chosen for manual cuts; variables which turned out to be strong indicators whether a track may have been misreconstructed. These variables are for instance Ndir and Ndir/Nall, since a high number of direct hits means that many of the recorded hits may have been caused by photons coming directly from the track without scattering. Such an event increases the success of a reconstruction. Other examples are the number of hits on a string and the order in which these hits occur on the string. Since we are only looking for upward going events (the signal region tracks shouldn't be tilted more than 10° with respect to the strings), it seems plausible to expect at least one string with a high number of hits (the string closest to the track). Also, the hits on this string should occur in an upward going order. If one has a high number of hits "out of order", one can regard such an event as most likely misreconstructed.

After these cuts were adjusted to values that lead to data distributions which are consistent with the expected atmospheric neutrinos, it became clear that most of the variables which were considered before are not necessary anymore. They have no or only little impact on the results. Most of them were supposed to remove misrecontructed events, which are now eliminated by variables such as Ndir. Therefore they were not used as cut variables anymore. This had the side effect of reducing the complexity of the relationships between different cut variables, which in turn made it easier to find the "right" cut settings. Five variables remained, which needed to be set by hand since the

| #1Nall | #3 Ndir/Nall | #6 Ldir |
|---|---|---|
| 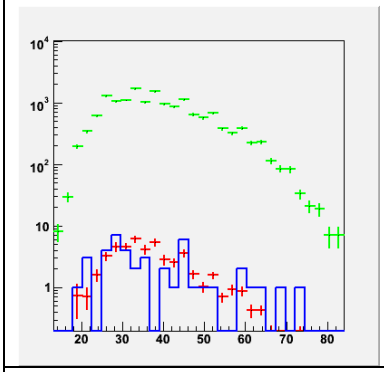 | 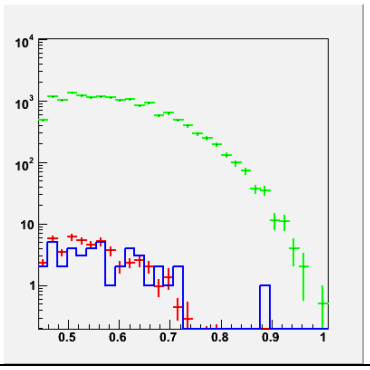 | 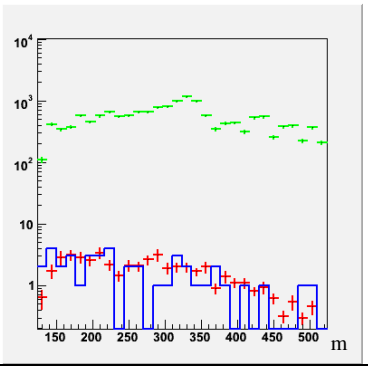 |
| cut range: 14 … 83 | cut range: 0.45 … 1.00 | cut range: 128.282 … 517.822 |

*Table 15 Examples of cut parameter distributions after cuts for1000GeV (soft)*

atmospheric muons (no atmospheric muons survived the cuts), atmospheric neutrinos, signals, data

The zenith angle cut has not been applied here, so that the entire angular region between 150° and 180° is present.

| zenith angle distribution of background | zenith angle distribution of signals |
|---|---|
| 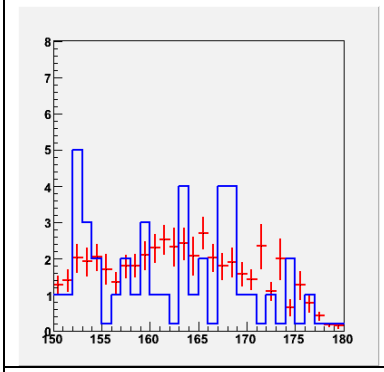 | 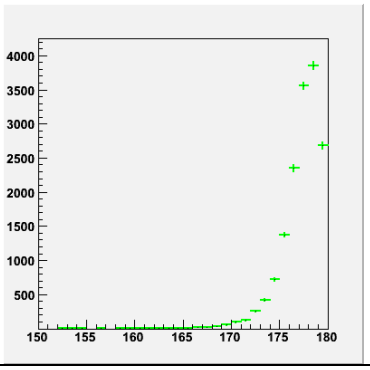 |
| atmospheric muons: 0<br>atmospheric neutrinos: 48.94<br>(for the live time of ca. 20% of the data – without weight: 11439)<br>(0.96 after zenith cut)<br>data: 42<br>(for the live time of ca. 20% of the data)<br>(1 after zenith cut) | signals: 15536.3<br>(11356.5 after zenith cut) |

*Table 16 Zenith angle distributions after cuts for1000GeV (soft)*

For 1000 GeV (soft) the minimizer found a zenith angle cut of 176.5° for the combined data set. The atmospheric neutrinos which remain after the zenith angle cut (0.96) are scaled to the live time of the remaining about 80% of the data, resulting in a combined number of 4.13 predicted background events. For a background of 4.13 events one gets an average upper limit on the signal mean $\overline{N}_{90}$=4.87. Combining all three years of signals which survived all cuts (incl. zenith cut) requires that the numbers of surviving signals are weighted according to the length of the live time (of the 80% data set) of each year, i.e. each signal is multiplied by the live time of this particular year divided by the average live time. This gives a number of s=11356.5. The same needs to be done for the generated signals. This case is easier, since the same number of signals was generated for each year (941549), so that one gets a total value of $s_{gen}$ = 941549 · 3 = 2824647.

minimizer was unable to fulfill this task due to the shortcoming of the simulated atmospheric muons. Two variables (and the zenith angle) were still automatically chosen by the minimizer.

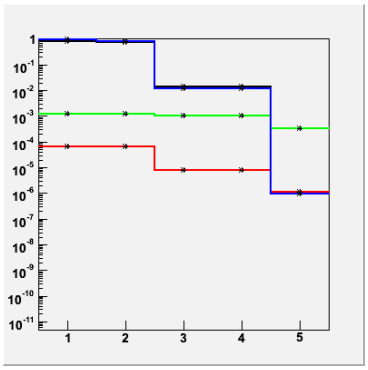

*Figure 29 Number of events (relative to the number of experimental events after L1/L2) for different filter steps*
atmospheric muons, atmospheric neutrinos, signals, data
1 after L1/L2
2 after retriggering
3 after zenith cut at 150°
4 after flare checking
5 after cut optimization

Before one starts with applying all filters and cuts, one can expect that the experimental data is dominated by (misreconstructed) atmospheric muons. While the first filter steps already reduce the number of data, the atmospheric muons still dominate. Only after the final cuts are applied and the fraction of atmospheric muons becomes smaller do the atmospheric neutrinos become the dominant part of the data, until the experimental data is entirely made up of atmospheric neutrinos (if there are no other neutrino sources).

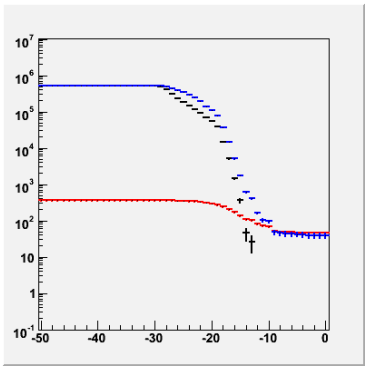

*Figure 30 Number of events for different cut strengths (of the final cut settings)*
atmospheric muons, atmospheric neutrinos, signals, data
Cut strength 0 is used for the analysis and corresponds to #5 in Figure 29. Smaller cut strengths widen the cut range for all parameters. Cut strength -50 is essentially equal to #4 in Figure 29.
For each cut strength, the cut parameter range is widened on both sides by a margin which is calculated by (upper cut value - lower cut value)·|cut strength|$^3$/30000.
The number of simulated atmospheric muons is scaled to the number of experimental events at cut strength -50.

| neutralino mass | Nall | | Ldir | | zenith angle | |
|---|---|---|---|---|---|---|
| | soft | hard | soft | hard | soft | hard |
| 50 GeV | 9/21 | 9/36 | 56.720/125.939 | 59.661/155.105 | 166.0 | 171.5 |
| 100 GeV | 9/31 | 13/52 | 77.365/192.248 | 83.340/266.091 | 172.5 | 175.0 |
| 250 GeV | 13/63 | 13/76 | 84.947/351.805 | 120.056/478.310 | 174.0 | 176.0 |
| 500 GeV | 13/71 | 21/87 | 95.997/455.916 | 172.409/517.842 | 176.5 | 176.0 |
| 1000 GeV | 14/83 | 17/102 | 128.282/517.822 | 195.214/531.180 | 176.5 | 176.0 |
| 3000 GeV | 15/128 | 16/174 | 185.549/526.977 | 226.615/535.749 | 177.5 | 177.5 |
| 5000 GeV | 16/116 | 21/178 | 190.768/530.079 | 238.713/541.383 | 177.5 | 177.5 |

*Table 17 Cut values of parameters which have been found automatically.*
All other cuts which were set manually can be found in the cut parameter table above:

After applying all cuts on the MC samples and the data, all atmospheric muons were gone within the chosen zenith range of 150º and 180º, and no excess of data over atmospheric neutrinos could be observed – the numbers of the remaining experimental events was consistent with the predicted background.

### 7.4.5 Some comments regarding previous unblinding proposals

Before this unblinding request, there were already two unsuccessful unblindings. The failure of the first attempt was originally explained with two different versions of Sieglinde (AMANDA's data processing software package) that were used for the L2 filtering (incl. reconstruction) for MC, the 20% sample, and the 80% sample. The second unblinding failed because there was a strong contamination by misreconstructed downward going muons. There are several key factors that contributed to this.

One of the cut variables (the space angle difference between the reconstruction results obtained by the maximum likelihood method and the direct walk method), which was intended to remove misreconstructed atmospheric muons, had a very strange behavior: It cut much stronger on events with zenith angles between 150° and 170°, while it cut only weakly on events with zenith angles between 170° and 180° – which is approximately the signal region. So it left a "bump" in the signal region containing many misreconstructed atmospheric muons. Because of low statistics, it was not possible to notice this in the 20% sample of the experimental data which was used for the unblinding proposal. Since the imulated atmospheric muons were gone after the cuts, this effect was not observed

before unblinding. After the unblinding results indicated a problem, the simulated atmospheric muons were tested with widened cut ranges of all cut parameters to increase the statistics. With the help of these loosened cuts, the anomalous behaviour of this particular cut variable was found.

An even more serious issue is the fact that certain aspects of the MC atmospheric muons are not simulated accurately enough (e.g. the number of hits, the z-component of the center of gravity of the hits), so that there are differences between MC and data. This prevented the problem mentioned above from being detected. After the cuts, there were no MC atmospheric muons left, even though they were not completely removed from the (80%) data set. Again, due to the low statistics it was impossible to notice any problem by checking the 20% data sample.

It is most likely that the problem of the insufficient quality of MC atmospheric muons combined with the low statistics of the 20% data sample was a major reason – if not the main reason – for the failure of the first unblinding. At that time, however, the thought was that these are separate samples which cannot be compared to each other due to the different filtering methods. In hindsight this was a mistake.

The disagreements between MC misreconstructed muons and the data is something that could not be solved – writing a new simulation was not practical. The only way to remove misreconstructed downward going events is comparing expected distributions of atmospheric neutrinos with the actual data. This step turned out to be the major obstacle

in the entire analysis. Many manual cuts were already made to remove misreconstructed atmospheric muons for the previous unblinding proposals (by comparing the distributions of the remaining data and atmospheric neutrinos after all cuts, and looking for regions which showed disagreements). Apparently it was not the right method.

After each unsuccessful unblinding, time was spent to investigate what went wrong. This included also comparing 20% of the data and the (then unblinded) 80% of the data. The question was, how a contamination by misreconstructed downward going muons can be prevented, if they do not show up in the MC sample, and the 20% data set does not give any indication of a problem. Different variables were analyzed or even new ones introduced (variable #9) to find an explanation for the discrepancies. For instance, it was found that the excess events from the 80% data set came mostly from events with Sdir>0.3, low Ndir, c.o.g.<-100, low numbers of hits on the string with the highest number of hits, etc. However, such events were not significantly enough present in the 20% sample to give a hint that there could be a problem. Again, this is due to the low statistics.

Eventually, it was decided to combine all three years into one single analysis. This leads to the advantages that excess events are easier to track back to particular regions of the cutparameter space (due to the combined statistics), and one has the same cuts for all three years. Also, the analysis was restricted to a much smaller number of cut parameters for manual cuts (to remove misreconstructed events). Both things reduced the chances of "carving out" certain events, which would make the 20% sample agree "accidentally"

with the simulation (which can easily happen for the low statistics that is used). This makes an important difference: For the previous attempts, the cut parameters were checked for each individual year to find differences between MC atmospheric neutrinos and the 20% data sample to remove misreconstructed downward going events, and a much higher number of cut parameters was used. Also, the minimizer was allowed to find different cuts for each year, which distorted the real situation. For this new unblinding attempt, it turned out that some stronger cuts had to be made on some variables (e.g. Ndir) to remove misreconstructed atmospheric muons. The new cut settings needed to be much more robust, since there was not the option anymore of setting cuts individually for each year. The price which had to be paid for this new approach was a loss of sensitivity.

Some of the properties of the excess events were learned after the first and second unblinding (e.g. c.o.g.), and some decisions were partially based on them for the third unblinding request. Unfortunately, this introduced an unwanted bias, since the analysis is not absolutely blind to the 80% sample anymore, even though the exact outcome of the unblinding is unknown. However, the seriousness of bias for the third unblinding request was reduced, since a new setup was used (combined data set without individual cuts for each year, and a much smaller number of variables).

# Chapter 8: Unblinding

After the unblinding proposal was accepted by the IceCube collaboration, the cut settings were applied to the remaining 80% of the data. It turned out that the year 2003 showed a very strange behavior of the strings 5 and 14, which could not be explained by any known issue: An analysis of all recorded vertical upward going events, showed that both strings were far more active than any other string, and also more active than in 2001-2002. It is possible that these vertical upward going events on these strings are not particle events, but that they were caused by some EM activities. This could explain why the number of events in the signal region in 2003 is in general higher than in 2001 and 2002 combined. Since no conclusive answer about these events can be given at this time, it was decided to exclude the year 2003 from further consideration.

| neutralino mass/channel | number of events in the signal region (between 150° and 180°) | |
|---|---|---|
| | 2001+2002<br>live time: 327.2 days | 2003<br>live time: 191.0 days |
| 50s | 7 (21) | 7 (17) |
| 50h | 5 (59) | 6 (48) |
| 100s | 5 (53) | 7 (37) |
| 100h | 1 (61) | 5 (34) |
| 250s | 9 (142) | 15 (113) |
| 250h | 9 (153) | 9 (100) |
| 500s | 6 (153) | 7 (111) |
| 500h | 9 (179) | 11 (117) |
| 1000s | 6 (146) | 8 (97) |
| 1000h | 10 (152) | 8 (97) |
| 3000s | 2 (162) | 5 (103) |
| 3000h | 2 (118) | 3 (76) |
| 5000s | 2 (157) | 3 (99) |
| 5000h | 2 (98) | 3 (70) |

*Table 18 Number of observed events after unblinding*
The numbers in bracket stand for events found in the total angular region between 150° and 180°; the numbers without bracket are the events within the signal region (i.e. after the zenith angle cut)

| 2001 | 2002 | 2003 |
|---|---|---|
| 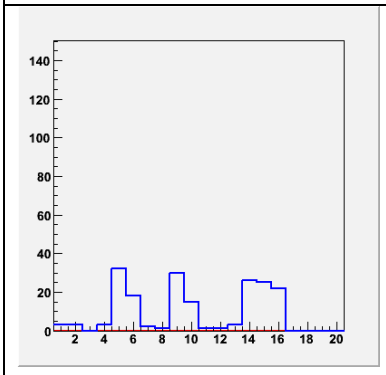 | 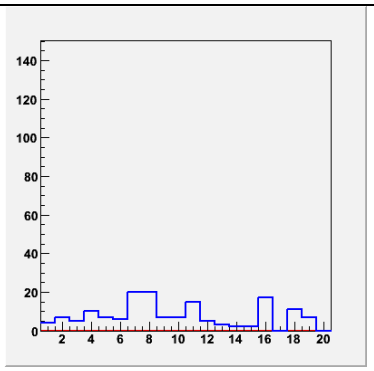 | 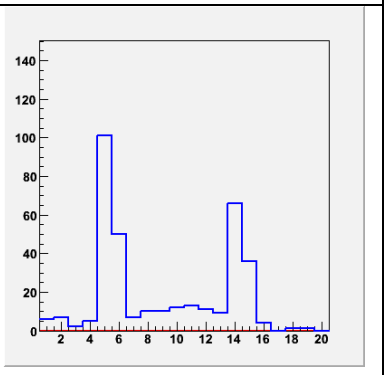 |

*Table 19 String occupancy for 2001, 2002, and 2003*

In order to interpret the results of the remaining live time (2001+2002), the data needs to be compared to the expected number of events, i.e. the simulated atmospheric neutrinos. This must also include an error analysis of these simulated events, which is done in the following sections.

Since the (simulated) OM efficiency is one of the error sources, new MC samples with different OM settings were produced. This new simulation was run independently from (and about two years after) the simulation which was used for the unblinding proposal. It turned out that a much smaller number of the newly simulated atmospheric neutrinos survived the cuts. It was not possible to find the reasons for this behavior, but it can be assumed that there could have been some settings for the original simulations which cannot be reproduced anymore. Also, it is not unlikely that there were some minor differences in the simulation code itself or different versions of some external libraries were used. It needs to be noted that this "phenomenon" was only observed for zenith regions outside the signal region, so that the impact on this analysis is small. This may also explain why it wasn't observed for the WIMP samples. In order to get consistent

results, all MC samples that were used for the final analysis came from this new simulation.

## 8.1 Error Calculations

### 8.1.1 Systematic uncertainties of the background

None of the misreconstructed simulated atmospheric muons survived, not only in the signal region, but also in the extended zenith region between 150° and 180°. Using the Feldman-Cousins method, one gets an upper limit on the (simulated) atmospheric muons of 2.44 (1.28) at a confidence level of 90% (68%). This can be done by treating the simulated atmospheric muons as signals, using zero for the background, and setting the number of "observed" events (i.e. simulated events which survived all cuts) to zero as well. The simulated lifetime of the atmospheric muons for 2001+2002 is 9.2 days while the actual lifetime for the 80% data sample is 327 days. This means that the upper limit on the atmospheric muons needs to be scaled to 86.7 (45.5) events for the extended zenith region. The upper limits for the much smaller signal region are shown in Table 20.

| neutralino mass/channel | zenith cut | upper limit on atm. muons in the signal region for a 90% (68%) confidence level |
|---|---|---|
| 50s | 166.0 | 19.2 (10.1) |
| 50h | 171.5 | 7.1 (3.7) |
| 100s | 172.5 | 5.5 (2.9) |
| 100h | 175.0 | 2.5 (1.3) |
| 250s | 174.0 | 3.5 (1.8) |
| 250h | 176.0 | 1.6 (0.8) |
| 500s | 176.5 | 1.2 (0.6) |
| 500h | 176.0 | 1.6 (0.8) |
| 1000s | 176.5 | 1.2 (0.6) |
| 1000h | 176.0 | 1.6 (0.8) |
| 3000s/h, 5000s/h | 177.5 | 0.6 (0.3) |

*Table 20 Upper limit on the atmospheric muons for a 90% and 68% confidence level in the signal region.*

Another study showed that widening the cut range (shifting the cuts to the outside) by only 5% to 10% on each side (if applicable) brings the first simulated atmospheric muon back. In general many more muons follow by increasing the range by one or two percent more. This shows that the upper limit of 2.44 (1.28) muons is a reasonable estimation, i.e. it is not too high.

The simulated atmospheric neutrinos are associated with a number of systematic uncertainties. A big error source is the overall flux of the atmospheric neutrinos. The tracks which survive all cuts originate from atmospheric neutrinos with energy mainly around the order of $10^2$ GeV to $10^3$ GeV. An error of 25% can be assumed for these neutrinos[113]. The systematic uncertainty in the charged current neutrino-nucleon scattering cross-section is less than 5% (see below).[115] Uncertainties in the cross-sections of the muon interactions (for the muon propagation through the ice) can be neglected.[114]

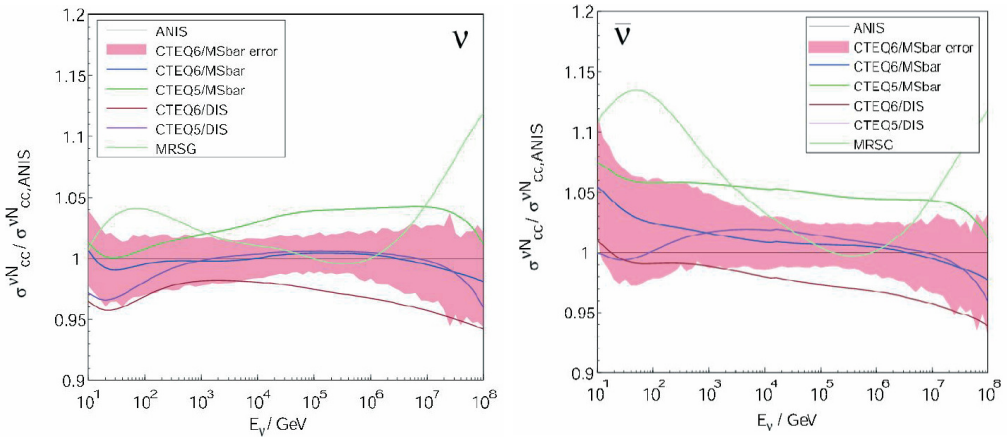


*Figure 31 Cross-section of the charged current neutrino-nucleon interaction for different models compared to ANIS.*[115]

Another uncertainty arises from the OM efficiencies. A simulation with an OM sensitivity of +10% and -10% has been performed, and the results for the neutrinos of the zenith region between 150° and 180° are shown in Figure 32. For WIMP masses/channels of 50GeV (soft/hard) and 100GeV (soft) a systematic error (on the

number of atmospheric neutrinos) of 60% is used. For all other masses/channels one can assume an error of 20%. The same numbers are used for the signal regions, since a similar study for the signal regions could not be used because the results were dominated by statistical fluctuations due to the low number of events in the signal region.

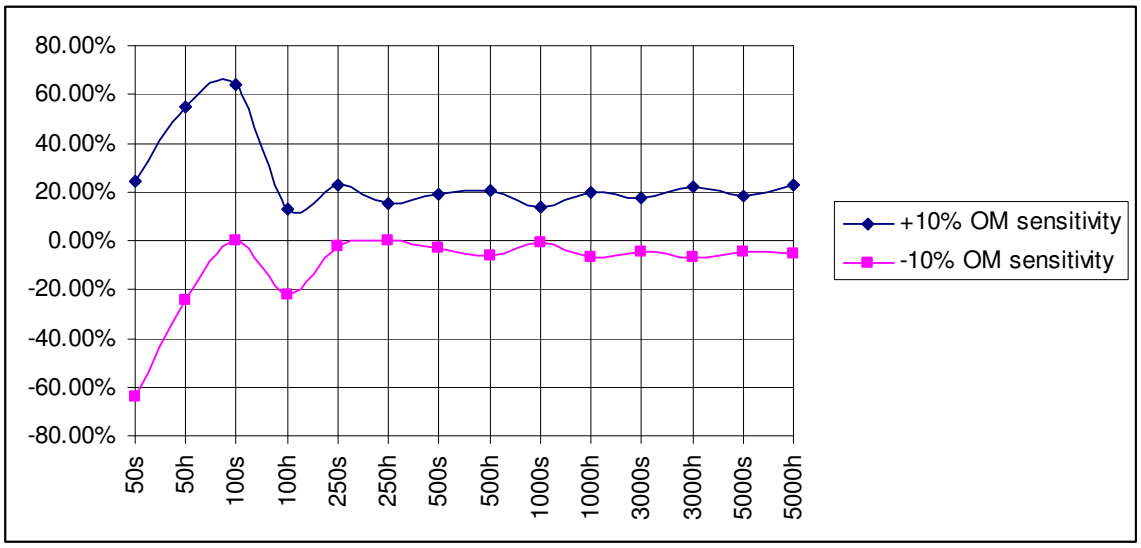


*Figure 32 Impact of variations of the OM sensitivity on the number of atmospheric neutrinos (after cuts)*

Reconstruction uncertainties originating from time calibration errors do not seem to lead to significant systematic errors.[116]

### 8.1.2 Statistical uncertainties of the background

The number of the (simulated) events is calculated with $N = \sum_i w_i \cdot e_i$, where $w_i$ is the weight of each simulated single event $e_i = 1$. The statistical uncertainties of the atmospheric neutrino background can be calculated through error propagation $\Delta N = \sqrt{\sum_i \left( \frac{\partial N}{\partial e_i} \Delta e_i \right)^2} = \sqrt{\sum_i (w_i \Delta e_i)^2}$. Assuming that each single event $e_i$ is Poisson

distributed with the mean $\lambda = e_i = 1$, then its variance is $\Delta e_i^2 = \lambda = 1$, so that $\Delta N = \sqrt{\sum_i w_i^2}$. The systematic uncertainties on the atm. neutrinos are shown in Table 21.

| neutralino mass/channel | statistical uncertainty for the zenith region between 150° and 180° | statistical uncertainty for the signal region |
|---|---|---|
| 50s | 6.4 | 4.8 |
| 50h | 8.0 | 4.8 |
| 100s | 8.1 | 4.3 |
| 100h | 6.3 | 1.3 |
| 250s | 7.3 | 1.8 |
| 250h | 6.6 | 1.1 |
| 500s | 7.4 | 0.5 |
| 500h | 6.5 | 0.9 |
| 1000s | 6.6 | 0.6 |
| 1000h | 6.0 | 0.7 |
| 3000s | 6.1 | 0.4 |
| 3000h | 5.2 | 0.3 |
| 5000s | 6.1 | 0.4 |
| 5000h | 4.9 | 0.3 |

*Table 21 Statistical uncertainties of the atmospheric neutrino background*

The total error of the background is calculated by adding the squares of all single errors for the zenith region between 150° and 180° as shown in Table 22.

| neutralino mass/ channel | error from misreconstr. atm. muons* | neutrino-nucleon scattering cross section | atm. neutrino flux | OM sensitivity | statistical uncertainty | total error* |
|---|---|---|---|---|---|---|
| 50s | -0% / +761% (399%) | 5% | 25% | 60% | 31% | -72% / +764% (405%) |
| 50h | -0% / +423% (222%) | 5% | 25% | 60% | 18% | -68% / +428% (232%) |
| 100s | -0% / +407% (214%) | 5% | 25% | 60% | 16% | -67% / +412% (224%) |
| 100h | -0% / +234% (123%) | 5% | 25% | 20% | 12% | -35% / +237% (128%) |
| 250s | -0% / +114% (60%) | 5% | 25% | 20% | 6% | -33% / +119% (68%) |
| 250h | -0% / +103% (54%) | 5% | 25% | 20% | 5% | -33% / +108% (63%) |
| 500s | -0% / +101% (53%) | 5% | 25% | 20% | 6% | -33% / +106% (62%) |
| 500h | -0% / +83% (44%) | 5% | 25% | 20% | 4% | -33% / +89% (55%) |
| 1000s | -0% / +107% (56%) | 5% | 25% | 20% | 5% | -33% / +112% (65%) |
| 1000h | -0% / +93% (48%) | 5% | 25% | 20% | 4% | -33% / +99% (58%) |
| 3000s | -0% / +87% (46%) | 5% | 25% | 20% | 4% | -33% / +93% (56%) |
| 3000h | -0% / +117% (61%) | 5% | 25% | 20% | 4% | -33% / +121% (69%) |
| 5000s | -0% / +90% (47%) | 5% | 25% | 20% | 4% | -33% / +96% (57%) |
| 5000h | -0% / +130% (68%) | 5% | 25% | 20% | 4% | -33% / +134% (75%) |

*Table 22 Total error for the entire angular region between 150° and 180°*

*The value outside the parenthesis use a 90% confidence level for the error of the misreconstructed muons; the values inside the parenthesis use a 68% confidence level.

The same was done for the signal region as shown in Table 23.

| neutralino mass/ channel | error from misreconstr. atm. muons* | neutrino-nucleon scattering cross section | atm. neutrino flux | OM sensitivity | statistical uncertainty | total error* |
|---|---|---|---|---|---|---|
| 50s | -0% / +202% (106%) | 5% | 25% | 60% | 51% | -83% / +218% (134%) |
| 50h | -0% / +134% (70%) | 5% | 25% | 60% | 56% | -86% / +159% (111%) |
| 100s | -0% / +112% (59%) | 5% | 25% | 60% | 51% | -83% / +139% (102%) |
| 100h | -0% / +46% (24%) | 5% | 25% | 20% | 38% | -50% / +68% (55%) |
| 250s | -0% / +34% (18%) | 5% | 25% | 20% | 24% | -40% / +53% (44%) |
| 250h | -0% / +33% (17%) | 5% | 25% | 20% | 27% | -42% / +54% (45%) |
| 500s | -0% / +27% (14%) | 5% | 25% | 20% | 23% | -40% / +48% (42%) |
| 500h | -0% / +42% (22%) | 5% | 25% | 20% | 20% | -38% / +57% (44%) |
| 1000s | -0% / +27% (14%) | 5% | 25% | 20% | 23% | -40% / +48% (42%) |
| 1000h | -0% / +42% (22%) | 5% | 25% | 20% | 18% | -37% / +56% (43%) |
| 3000s | -0% / +32% (17%) | 5% | 25% | 20% | 25% | -41% / +52% (44%) |
| 3000h | -0% / +35% (18%) | 5% | 25% | 20% | 20% | -38% / +52% (42%) |
| 5000s | -0% / +33% (17%) | 5% | 25% | 20% | 25% | -41% / +53% (44%) |
| 5000h | -0% / +46% (24%) | 5% | 25% | 20% | 21% | -39% / +60% (45%) |

*Table 23 Total error for the signal region*

*The value outside the parenthesis use a 90% confidence level for the error of the misreconstructed muons; the values inside the parenthesis use a 68% confidence level.

### 8.1.3 Uncertainties of the signal efficiency

There are only two significant sources contributing to the systematic uncertainty of the signal efficiency. As for the atmospheric neutrinos, there is again an uncertainty in the charged current neutrino-nucleon scattering cross-section of 5%. The systematic error from the uncertainty of the OM sensitivity is approximately 10% for WIMP masses/channels of 50GeV (soft/hard) and 100GeV (soft). For all other masses/channels one can use an error of 5% (see Figure 33). The statistical uncertainty is very small due to the large number of (simulated) events, and can be neglected.

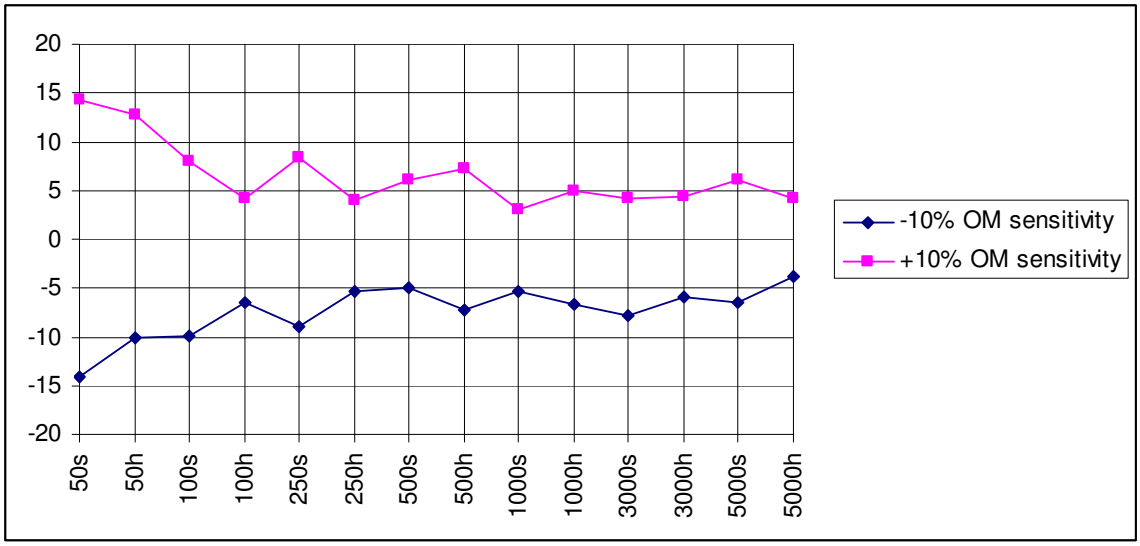


*Figure 33 Impact of variations of the OM sensitivity on the number of signals (after cuts)*

Therefore the total error of the signal efficiency is 11% for 50GeV (soft/hard) and 100Gev (soft), and 7% for all other WIMP masses/channels.

## 8.2 Unblinding Results

The results of the error analysis can be used for a comparison between the experimental data and the simulated atmospheric neutrinos. This comparison is shown in the histograms of Table 24 over the next three pages. The zenith region between cos(150°) and cos(180°) was divided into 30 bins for this comparison. For each bin of the histograms of Table 24, the error due to misreconstructed atmospheric muons is calculated separately based on the space angle covered by the particular bin. The red band uses a confidence level of 68% for the uncertainty of the misreconstructed atmospheric muons, while the orange band (combined with the red band) uses a confidence level of 90% for this particular error. All other errors are calculated based on

the number of events in each bin, while for the statistical error the weights of each single event needed to be considered.

| neutralino mass | soft channel | hard channel |
|---|---|---|
| 50GeV | 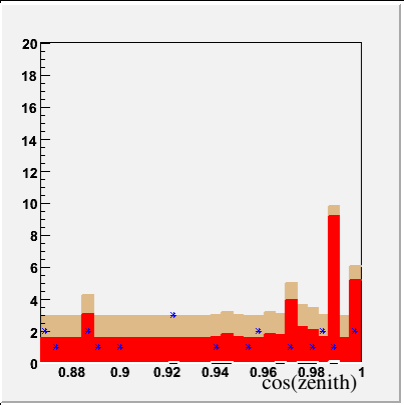 | 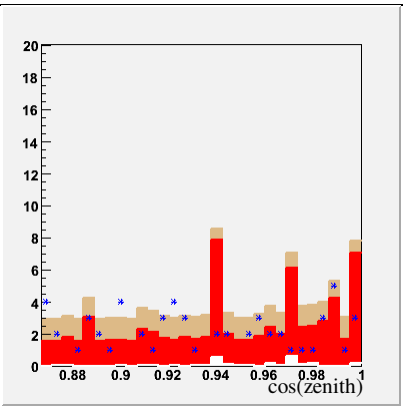 |
| 100GeV | 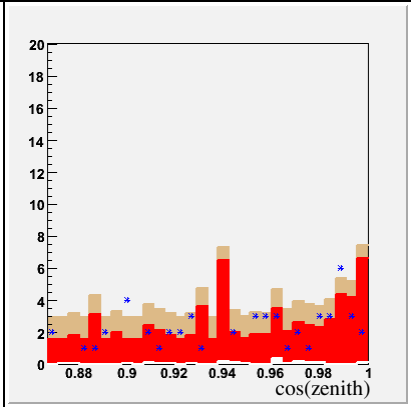 | 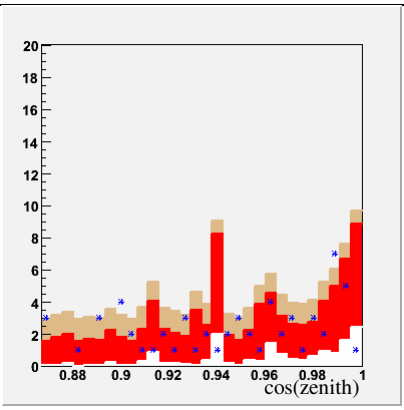 |
| 250GeV | 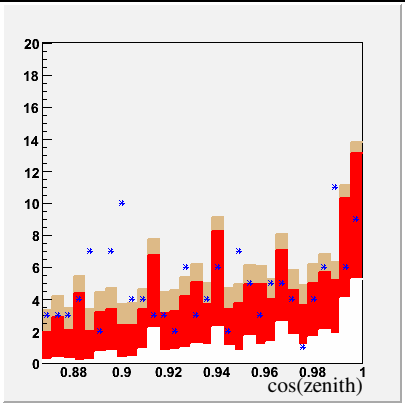 | 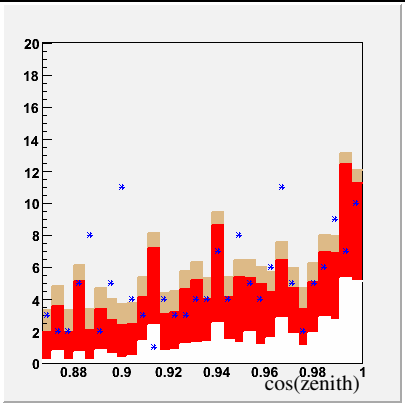 |



*Table 24 Zenith angle distribution for the observed events and the expected atmospheric neutrino background including systematic and statistical errors for each bin.*
Description see page 137

| | | |
|---|---|---|
| 500GeV | 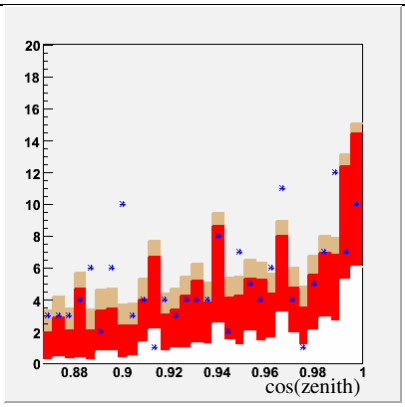 | 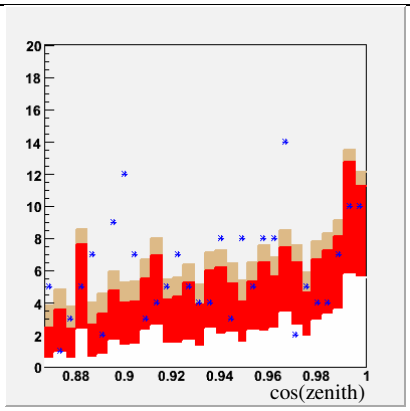 |
| 1000GeV | 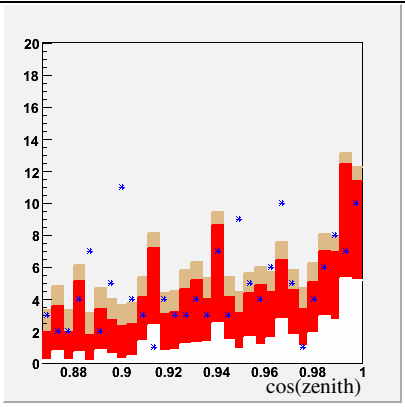 | 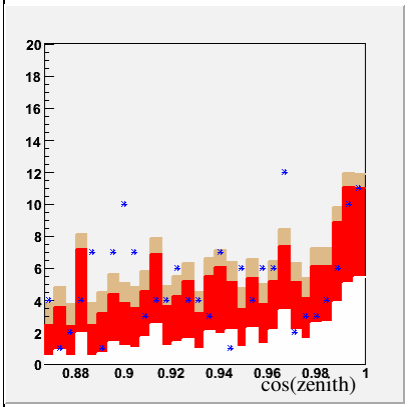 |
| 3000GeV | 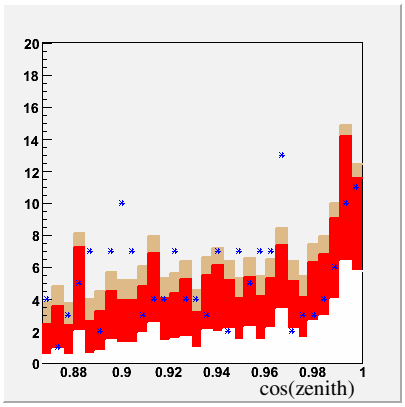 | 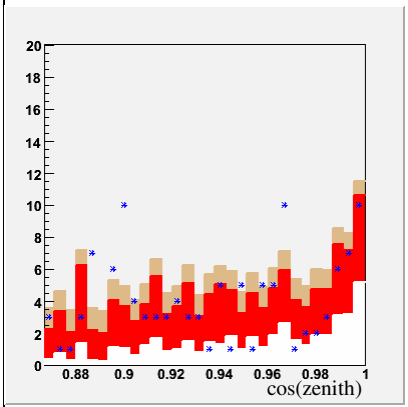 |

*Table 24 Zenith angle distribution for the observed events and the expected atmospheric neutrino background including systematic and statistical errors for each bin.*

Description see page 137

| | | |
|---|---|---|
| 5000GeV | 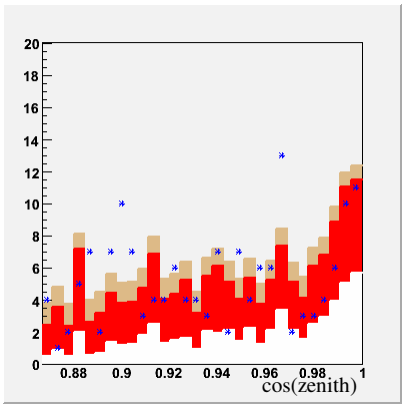 | 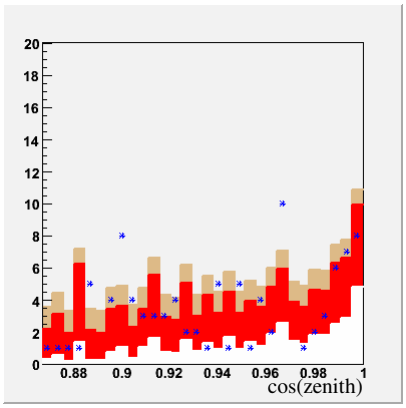 |

*Table 24 Zenith angle distribution for the observed events and the expected atmospheric neutrino background including systematic and statistical errors for each bin.*
The Zenith region is between cos(150°) and cos (180°).
The red band uses a confidence level of 68% for the uncertainty of the misreconstructed atmospheric muons, while the orange band (combined with the red band) uses a confidence level of 90% for this particular error. The blue markers represent the experimental data.
Some systematic errors are relative to the number of events, and the statistical error also becomes bigger with a higher number of events. Therefore the error bars grow larger in zenith regions with a higher number of atmospheric neutrinos which is the case near the vertical.

The expected number of atmospheric neutrinos (including the total error) in the signal region compared to the number of experimental events are shown below in Table 25.

| neutralino mass/channel | simulated atm. neutrinos | | data |
|---|---|---|---|
| | without error | with error and a confidence level of 90% (68%) for the uncertainty of the misreconstructed atmospheric muons | |
| 50s | 9.5 | 1.8 – 30.2 (22.2) | 7 |
| 50h | 5.3 | 0.8 – 13.7 (11.1) | 5 |
| 100s | 4.9 | 0.9 – 11.7 (9.8) | 5 |
| 100h | 5.4 | 2.8 – 9.0 (8.3) | 1 |
| 250s | 10.3 | 6.5 – 15.6 (14.6) | 9 |
| 250h | 4.9 | 3.0 – 7.4 (7.0) | 9 |
| 500s | 4.4 | 2.8 – 6.4 (6.1) | 6 |
| 500h | 3.8 | 2.5 – 5.9 (5.4) | 9 |
| 1000s | 4.4 | 2.8 – 6.4 (6.1) | 6 |
| 1000h | 3.8 | 2.5 – 5.9 (5.3) | 10 |
| 3000s | 1.9 | 1.2 – 2.9 (2.7) | 2 |
| 3000h | 1.7 | 1.1 – 2.6 (2.4) | 2 |
| 5000s | 1.8 | 1.1 – 2.7 (2.6) | 2 |
| 5000h | 1.3 | 0.8 – 2.1 (1.9) | 2 |

*Table 25 Expected atmospheric neutrino background with and without error compared to the observed number of events in the signal region.*

In general the experimentally observed number of events in the signal region lies within the range of the expected number of atmospheric neutrinos. In the three cases (250h, 500h, 1000h) where the observed number is outside this range, the excess is not significant enough to claim a discovery of a signal. This argument is further supported by the fact that disagreements between data and simulation occur also over an extended zenith region outside the signal region (see histograms in Table 24 for 150° … 180° and the three "special cases" for 168.5° … 180° in Table 26 below).

| 250h | 500h | 1000h |
|---|---|---|
| 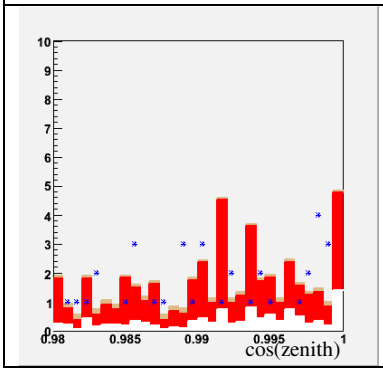 | 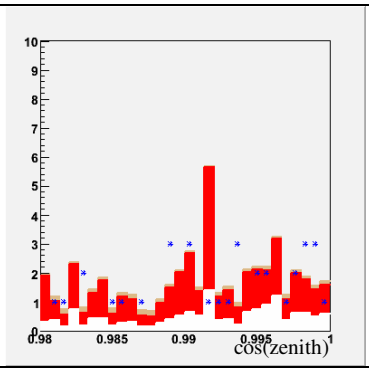 | 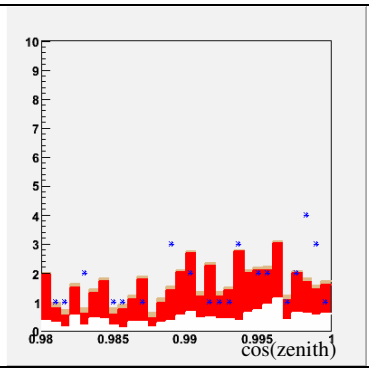 |



*Table 26 Zenith angle distribution for the observed events and the expected atmospheric neutrino background including systematic and statistical errors for each bin.*
The Zenith region is between cos(168.5°) and cos (180°).
The red band uses a confidence level of 68% for the uncertainty of the misreconstructed atmospheric muons, while the orange band (combined with the red band) uses a confidence level of 90% for this particular error. The blue markers represent the experimental data.
These plots are the "magnified" parts of the plots from the previous table for three particular cases (250h, 500h, 1000h) where a small disagreement between data and expected background was visible.

With the results from above one can now calculate the upper limit on the signal mean $N_{90}(b,n)$ including the error on the background and the error on signal efficiency. The procedure is again the Feldman-Cousins method; however the probability density function gets modified in the following way.[117] The original Poisson distribution gets convoluted with the probability distribution of the error (for the background and the signal efficiency), where a Gaussian is used for this calculation:

$$p_e(b+s,n) = \frac{1}{2\pi\sigma_b\sigma_s}\int_0^\infty\int_0^\infty db'ds'p(b'+s',n)e^{-\frac{(b-b')^2}{2\sigma_b^2}}e^{-\frac{(s-s')^2}{2\sigma_s^2}} \quad (85)$$

Since the error of the background is not symmetric the Gaussian is split into two parts. Another problem arises from the fact that these integrals are restricted to positive values. Therefore the result is reweighed depending on the fraction of the Gaussian that is lost by the cut-off at zero. The upper limits on the signal mean $N_{90}(b,n)$ under consideration of the error on the background and the error on signal efficiency is shown in Table 27.

| neutralino mass/channel | expected atm. neutrinos | observed events | total error on the background* | total error on the signal efficiency* | upper limit on the signal mean (90% confidence level) |
|---|---|---|---|---|---|
| 50s | 9.5 | 7 | -83% +134% | 11% | 8.91 |
| 50h | 5.3 | 5 | -86% +111% | 11% | 7.13 |
| 100s | 4.9 | 5 | -83% +102% | 11% | 7.32 |
| 100h | 5.4 | 1 | -50% +55% | 7% | 1.77 |
| 250s | 10.3 | 9 | -40% +44% | 7% | 8.09 |
| 250h | 4.9 | 9 | -42% +45% | 7% | 11.46 |
| 500s | 4.4 | 6 | -40% +42% | 7% | 8.00 |
| 500h | 3.8 | 9 | -38% +44% | 7% | 12.05 |
| 1000s | 4.4 | 6 | -40% +42% | 7% | 8.00 |
| 1000h | 3.8 | 10 | -37% +43% | 7% | 13.08 |
| 3000s | 1.9 | 2 | -41% +44% | 7% | 4.05 |
| 3000h | 1.7 | 2 | -38% +42% | 7% | 4.23 |
| 5000s | 1.8 | 2 | -41% +44% | 7% | 4.14 |
| 5000h | 1.3 | 2 | -39% +45% | 7% | 4.60 |

*Table 27 Expected and observed number of events, errors, and upper limits on the signal mean in the signal region*

*The errors with a 68% confidence level for the uncertainty of the misreconstructed atmospheric muons are quoted here, since equation (85) requires the values of 1σ.

The value of $s_{90}$ – the upper limit of hypothetical generated signal muons $s_{90} = s_{gen} \cdot N_{90} / s$ – is equal to the upper limit of the number of signal muon-neutrinos that were "converted" into muons via a charged current interaction with a nucleon in the ice of the detector. Therefore one can calculate the upper limit on the neutrino muon conversion rate $\Gamma_{\nu\mu} = s_{90} / (V_{gen} t) = N_{90} (V_{eff} t)$, where $t$ is the live time of the data (the 80%

of the data for 2001+2002 have a live time of 327.2 days), $V_{gen}$ is the volume in which the hypothetical signal muons are produced, and $V_{eff} = V_{gen} s / s_{gen}$ is the effective volume (see Table 29). Small effective volumes indicate either that the detector is not very sensitive to a particular signal and/or that the chosen cuts removed a large fraction of the signals. The number of generated signals and the generation volume for different neutralino masses are shown in Table 28.

| neutralino mass | $s_{gen}$ (soft channel)* | $s_{gen}$ (hard channel)* | generation volume | |
|---|---|---|---|---|
| | | | height / m | radius / m |
| 50 GeV | 519889 | 676868 | 800 | 170 |
| 100 GeV | 688385 | 880507 | 950 | 190 |
| 250 GeV | 833964 | 955805 | 1550 | 230 |
| 500 GeV | 902485 | 978039 | 2350 | 270 |
| 1000 GeV | 941549 | 989173 | 3500 | 290 |
| 3000 GeV | 972783 | 996620 | 6150 | 320 |
| 5000 GeV | 980617 | 998178 | 7600 | 410 |

*Table 28 Generated signals and generation volume for different simulated neutralino masses*
*The number of generated signals represents the annual values for 2001 and 2002.

This conversion rate $\Gamma_{\nu\mu}$ is a function of the neutralino annihilation rate $\Gamma_A$. This function depends on the branching ratios of the different annihilation channels with different annihilation products (not all of them result in muon-neutrinos), the energy spectra of the neutrinos produced by different annihilation channels, the cross-section for the charged current interaction between muon-neutrinos and nuclei, and the nucleon density in the effective volume surrounding the detector. A lower cutoff at 10GeV must be used for this calculation, since it must be taken into account that the detector was simulated with an energy threshold of 10GeV. With the help of the neutralino annihilation rate, one can also calculate the expected muon flux $\Phi_\mu$ at the detector. The muon flux has a similar dependency on the annihilation rate as the neutrino-muon conversion rate mentioned. The muon flux can be estimated for any detector energy

threshold. Here an energy threshold of 1GeV has been used in order to be able to compare it with other experiments.

The calculation of both numbers – the neutralino annihilation rate and the muon flux – is not straight forward. The upper limits on $\Gamma_A$ and $\Phi_\mu$ can be calculated with a script by Joakim Edsjö.[118] The input parameters are the conversion rate $\Gamma_{\nu\mu}$, the annihilation channel, and the energy threshold. The results can be seen in Table 29 and Figure 34. The muon flux limit for the lower neutralino masses is much higher than for more massive neutralinos. This can be explained by the fact that the lower neutralino masses lead to neutrinos/muons with smaller energies, which in turn leads to lower signal efficiencies and shorter muon ranges. Both effects reduce the effective volume, and the muon flux. The fluctuations in the limit on the muon flux for the lower neutralino masses (of the hard channel) are due to the fluctuations in the background.

| neutralino mass/channel | signals* | effective volume | upper limit (90% confidence level) | | |
|---|---|---|---|---|---|
| | | | neutrino-muon conversion rate | neutralino annihilation rate | muon flux for a detector threshold of 1 GeV |
| | | $m^3$ | $km^{-3}\ yr^{-1}$ | $s^{-1}$ | $km^{-2}\ yr^{-1}$ |
| 50s | 700 | $4.89 \cdot 10^4$ | 203245 | $3.63 \cdot 10^{16}$ | 26819 |
| 50h | 2460 | $1.32 \cdot 10^5$ | 60254 | $1.45 \cdot 10^{15}$ | 5321 |
| 100s | 2343 | $1.83 \cdot 10^5$ | 44530 | $1.40 \cdot 10^{15}$ | 4346 |
| 100h | 7582 | $4.64 \cdot 10^5$ | 4256 | $2.60 \cdot 10^{13}$ | 575 |
| 250s | 4189 | $6.47 \cdot 10^5$ | 13948 | $1.11 \cdot 10^{14}$ | 2007 |
| 250h | 19616 | $2.64 \cdot 10^6$ | 4836 | $1.05 \cdot 10^{13}$ | 1684 |
| 500s | 4408 | $1.31 \cdot 10^6$ | 6789 | $2.51 \cdot 10^{13}$ | 1573 |
| 500h | 28744 | $7.91 \cdot 10^6$ | 1699 | $1.78 \cdot 10^{12}$ | 1101 |
| 1000s | 6557 | $3.22 \cdot 10^6$ | 2771 | $5.34 \cdot 10^{12}$ | 1069 |
| 1000h | 30316 | $1.42 \cdot 10^7$ | 1030 | $5.30 \cdot 10^{11}$ | 1187 |
| 3000s | 7295 | $7.42 \cdot 10^6$ | 609 | $4.88 \cdot 10^{11}$ | 496 |
| 3000h | 20751 | $2.06 \cdot 10^7$ | 229 | $3.89 \cdot 10^{10}$ | 580 |
| 5000s | 4786 | $9.79 \cdot 10^6$ | 471 | $2.67 \cdot 10^{11}$ | 521 |
| 5000h | 13343 | $2.68 \cdot 10^7$ | 191 | $1.95 \cdot 10^{10}$ | 660 |

*Table 29 Upper limits of the neutrino-muon conversion rate, the neutralino annihilation rate, and the muon flux*

*Numbers of signals are weighted according to the length of the live time (of the 80% data set) of each year, i.e. each signal is multiplied by the live time of this particular year divided by the average live time.

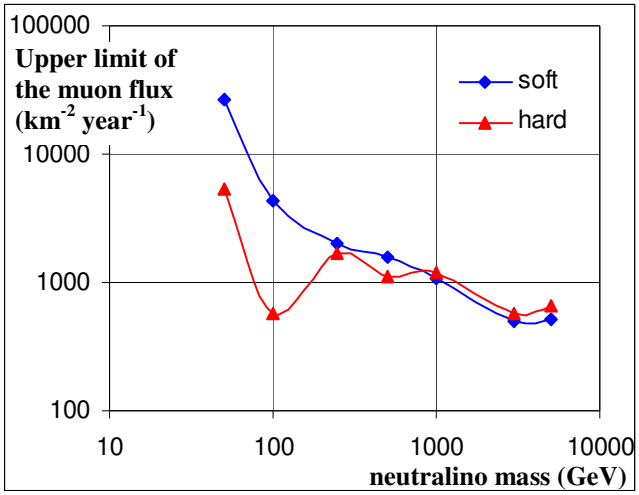


*Figure 34 Upper limits of the muon flux coming from neutralino annihilations for the soft and hard channel*
These results were obtained from observation in 2001-2002 with a combined live time of 327 days.
The fluctuations in the limits have their origin in the fluctuations of the background.

### 8.2.1 Comparison to other experiments

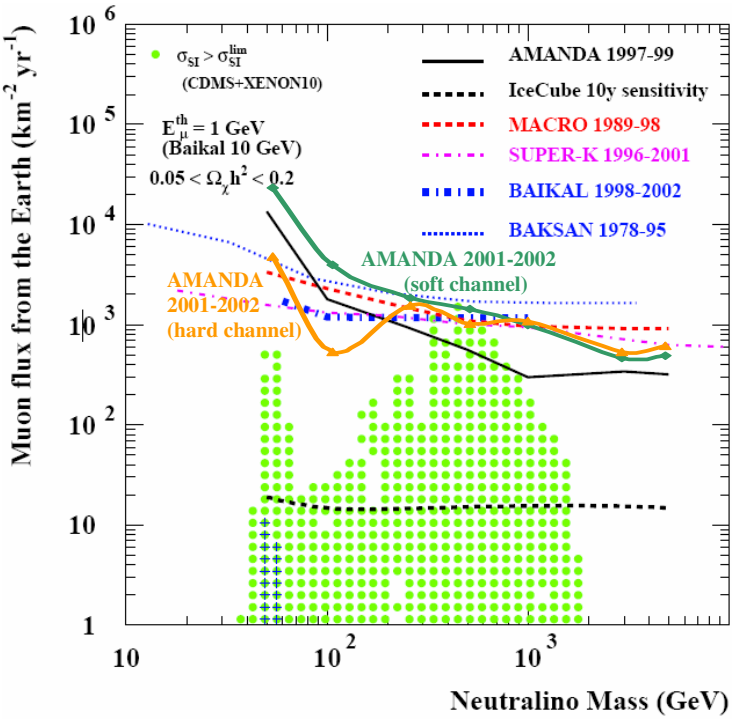


*Figure 35 Upper limits of muon fluxes from neutralino annihilations in the center of the Earth obtained by various experiments compared with predictions from a wide range of possible combinations of MSSM parameters for the neutralinos.*[119]
The green dots represent MSSM models with a predicted neutralino scattering cross-section that have already been probed by direct WIMP searches (with spin-independent scattering) with no signals detected, and therefore disfavored. The blue crosses stand for MSSM models which lead to scattering cross-sections smaller than the cross-section limits obtained by direct detection experiments, i.e. MSSM models which were not probed yet. Regions which have no dots or crosses cannot be constructed by any combination of MSSM parameters.

As one can see from Figure 35, the limits obtained by this analysis are in the same order of magnitude as other indirect detection experiments, however a previous analysis done with AMANDA data for 1997-1999 gives generally better limits. The main reason for these differences comes from the fact that the final data sample is still contaminated by misreconstructed muons. Other difficulties described in 7.4.5 also lead to higher flux limits. The estimated sensitivity for the IceCube experiment after a ten year period of data collection will be about two orders of magnitude better than the current limits obtained by other indirect detection experiments.

Figure 35 also shows a "translation" of different MSSM models into muon fluxes from neutralino annihilation inside the Earth. For this plot, various combinations of the values of the undetermined parameters of the MSSM (such as $\mu$ and $\tan\beta$) were considered. The scattering and annihilation cross-sections were determined for each of these MSSM models. Some of these models were excluded, if they are either ruled out by constraints obtained from accelerators, or if they lead to a universe with a dark matter density which is not consistent with present observations. Otherwise, the neutralino capture rates in the Earth, annihilation rates, neutrino fluxes and muon fluxes were calculated with the help of these predicted cross-sections. The muon fluxes calculated for each MSSM model were put into Figure 35. Green dots are used, if the predicted neutralino scattering cross-section for a particular MSSM model is bigger than the limit on the cross-section obtained by direct detection experiments. That means that a neutralino with this MSSM parameter combination should have been detected by these experiments, but it was not. Therefore this region in the plot is already disfavored. MSSM models with scattering

cross-sections smaller than the direct detection limits are represented by blue crosses. These regions could not be probed yet by these experiments since their cross-section is too small; these regions in the plot are not disfavored yet.

Note, that only spin-independent scattering cross-sections of direct detection experiments were considered here. Spin-independent scattering is the relevant class of reactions for the indirect neutralino detection via neutralino annihilation inside the Earth, since the dominant nuclei in the Earth (such as $^{56}Fe$) are spinless. These nuclei are responsible for the spin-independent scattering of the neutralinos, which causes the neutralinos to lose energy and get trapped inside Earth.

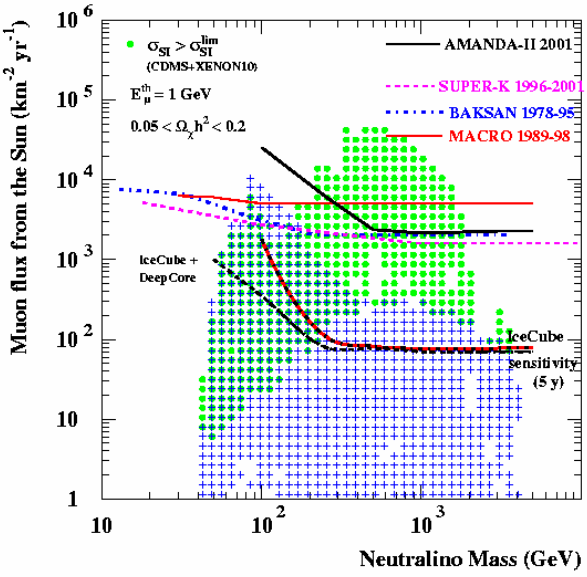


*Figure 36 Upper limits of muon fluxes from neutralino annihilations in the sun*[119]
For an explanation concerning the results from direct detection experiments see Figure 35. IceCube and Deep Core are discussed in 5.9.1

Over the past couple of years, huge progress has been made in lowering the cross-section limits for direct detection experiments. This is the reason why the current limits of indirect detection methods are deep inside the region which has already been disfavored. Also, the predicted limits of the IceCube experiment will not be able to enter the regions

which were not already probed by direct detection as one can see in Figure 35. For “solar WIMPs”, the picture looks a little bit better (see Figure 36) due to the facts explained in 4.4, e.g. higher escape velocity of the sun makes the much bigger fraction of the neutralino velocity distribution available, higher mass of the sun, additional spin-dependent neutralino scattering on the hydrogen nuclei in the sun. The planned Deep Core extension of IceCube (see 5.9.1) will improve the expected results with IceCube due to its better low energy behaviour.

Indirect detection experiments like AMANDA or IceCube are complementary ways to search for dark matter neutralinos since they provide an independent verification for the results of direct detection experiments. Therefore they serve a very valuable function.

# Chapter 9: Summary and Outlook

The goals of this analysis the search for dark matter, which is believed to make up about one quarter of the energy content of the universe. The analysis was done under the assumption that the dark matter consists of neutralinos, which accumulate inside the Earth, annihilate and create neutrinos through the decay of the annihilation products. A signal from this process would have manifested itself as an excess of neutrinos over a known background of atmospheric neutrinos traveling upward through the AMANDA detector at the South Pole. This analysis did not reveal such an excess. Therefore only an upper limit could be calculated. This limit is expressed in terms of a muon flux, since the neutrinos are not detected directly, and only the muons produced by a charged-current interaction of the signal neutrinos can be observed with the detector.

The data which was analyzed represent a live time of 518 days for the years 2001 to 2003. Since the data set of 2003 showed events which were most likely not caused by "real" events, this year needed to be dropped, so that the remaining live time used for this analysis is 327 days.

The main problem of the analysis came from the misreconstructed atmospheric muons which contaminated the final data set. Unfortunately it was not possible to remove all of them. This had a negative effect on the upper limit of the muon flux. However, the results support the limits found by other experiments for indirect neutralino dark matter detection. The new IceCube experiment (together with Deep Core), which is built around the AMANDA detector will be able to push the limit of the muon flux from neutrinos

caused by neutralino annihilation in the Earth to even smaller values, but it will not be more sensitive than direct detection experiments (however IceCube may achieve comparable results for neutralino detection via neutralino annihilation inside the sun). Even though the direct detection methods have a higher sensitivity, it is important to be able to verify (or to disprove) their results with another – independent – method. This is the reason why experiments such as AMANDA and IceCube are very useful for the search for neutralino dark matter.

# Appendices

## Appendix A: Conventions and useful relationships

- The Dirac vector is defined as $\psi = \begin{pmatrix} \xi_\alpha \\ \chi^{\dot{\alpha}\dagger} \end{pmatrix}$, where $\xi$ and $\chi$ are the left and right handed (two component) Weyl spinor fields.

- The following notation is used often:

$$\overline{\psi} = \psi^\dagger \begin{pmatrix} 0 & \delta_\beta^\alpha \\ \delta_{\dot{\alpha}}^{\dot{\beta}} & 0 \end{pmatrix} = \begin{pmatrix} \xi_{\dot{\alpha}}^\dagger & \chi^\alpha \end{pmatrix} \begin{pmatrix} 0 & \delta_{\dot{\beta}}^{\dot{\alpha}} \\ \delta_\alpha^\beta & 0 \end{pmatrix} = \begin{pmatrix} \chi^\beta & \xi_{\dot{\beta}}^\dagger \end{pmatrix}.$$

- The charge conjugated fields is $\psi^C = C\overline{\psi}^T = \begin{pmatrix} \varepsilon_{\alpha\beta} & 0 \\ 0 & \varepsilon^{\dot{\alpha}\dot{\beta}} \end{pmatrix} \begin{pmatrix} \chi^\beta \\ \xi_{\dot{\beta}}^\dagger \end{pmatrix} = \begin{pmatrix} \chi_\alpha \\ \xi^{\dot{\alpha}\dagger} \end{pmatrix}$ with $C = -C^{-1} = -C^T$. One can see that the charge conjugation of the right handed field $\chi^{\dot{\alpha}\dagger}$ turns it into a the left handed field $\chi_\alpha$.

- The Pauli matrices are defined as $\sigma_0 = \overline{\sigma}_0 = \begin{pmatrix} 1 & 0 \\ 0 & 1 \end{pmatrix}$, $\sigma_1 = -\overline{\sigma}_1 = \begin{pmatrix} 0 & 1 \\ 1 & 0 \end{pmatrix}$, $\sigma_2 = -\overline{\sigma}_2 = \begin{pmatrix} 0 & -i \\ i & 0 \end{pmatrix}$, and $\sigma_3 = -\overline{\sigma}_3 = \begin{pmatrix} 1 & 0 \\ 0 & -1 \end{pmatrix}$ or in general $\overline{\sigma}_\mu^{\dot{\alpha}\alpha} = \varepsilon^{\dot{\alpha}\dot{\beta}} \varepsilon^{\beta\beta} \sigma_{\mu\dot{\beta}\beta}$

- The gamma matrices are defined as $\gamma_\mu = \begin{pmatrix} 0 & \sigma_\mu \\ \overline{\sigma}_\mu & 0 \end{pmatrix}$, $\gamma_5 = \begin{pmatrix} -\mathbf{1} & 0 \\ 0 & \mathbf{1} \end{pmatrix}$. Some useful properties are $\gamma_\mu^2 = \begin{cases} \mathbf{1} & \text{for } \mu = 0,5 \\ -\mathbf{1} & \text{for } \mu = 1,2,3 \end{cases}$

- The projection operators, which project the left and right handed part of the Dirac vector are $P_L = \frac{\mathbf{1}-\gamma_5}{2} = \begin{pmatrix} \mathbf{1} & 0 \\ 0 & 0 \end{pmatrix}$ and $P_R = \frac{\mathbf{1}+\gamma_5}{2} = \begin{pmatrix} 0 & 0 \\ 0 & \mathbf{1} \end{pmatrix}$, which leads to $P_L\psi = \begin{pmatrix} \xi_\alpha \\ 0 \end{pmatrix} = \psi_L$ and $P_R\psi = \begin{pmatrix} 0 \\ \chi^{\dot\alpha\dagger} \end{pmatrix} = \psi_R$, so that $\psi = \psi_L + \psi_R$

They have the property $P_{L/R}^2 = \frac{1}{4}(\mathbf{1} \mp \gamma_5)^2 = \frac{1}{4}(\mathbf{1} \mp 2\gamma_5 + \mathbf{1}) = \frac{1}{2}(\mathbf{1} \mp \gamma_5) = P_{L/R}$

- Some useful relationships involving Dirac spinors:

$\overline{\psi}\psi = \begin{pmatrix} \chi^\alpha & \xi^\dagger_{\dot\alpha} \end{pmatrix} \begin{pmatrix} \xi_\alpha \\ \chi^{\dot\alpha\dagger} \end{pmatrix} = \chi^\alpha\xi_\alpha + \xi^\dagger_{\dot\alpha}\chi^{\dot\alpha\dagger} = \chi\xi + \chi^\dagger\xi^\dagger$ is the structure which is used for the Dirac mass term.

$\overline{\psi}\psi = \overline{\psi}P_R\psi + \overline{\psi}P_L\psi = \chi^\dagger\xi^\dagger + \chi\xi$ and $\overline{\psi}\psi = \overline{\psi}_L\psi_R + \overline{\psi}_R\psi_L = \chi^\dagger\xi^\dagger + \chi\xi$

$\overline{\psi}P_R\psi = \begin{pmatrix} \chi^\alpha & \xi^\dagger_{\dot\alpha} \end{pmatrix} \begin{pmatrix} 0 \\ \chi^{\dot\alpha\dagger} \end{pmatrix} = \xi^\dagger_{\dot\alpha}\chi^{\dot\alpha\dagger} = \chi^\dagger\xi^\dagger$ and $\overline{\psi}_L\psi_R = \begin{pmatrix} 0 & \xi^\dagger_{\dot\alpha} \end{pmatrix} \begin{pmatrix} 0 \\ \chi^{\dot\alpha\dagger} \end{pmatrix} = \xi^\dagger_{\dot\alpha}\chi^{\dot\alpha\dagger} = \chi^\dagger\xi^\dagger$

$\overline{\psi}P_L\psi = \begin{pmatrix} \chi^\alpha & \xi^\dagger_{\dot\alpha} \end{pmatrix} \begin{pmatrix} \xi_\alpha \\ 0 \end{pmatrix} = \chi^\alpha\xi_\alpha = \chi\xi$ and $\overline{\psi}_R\psi_L = \begin{pmatrix} \chi^\alpha & 0 \end{pmatrix} \begin{pmatrix} \xi_\alpha \\ 0 \end{pmatrix} = \chi^\alpha\xi_\alpha = \chi\xi$

$\overline{\psi}\gamma^\mu P_R\psi = \begin{pmatrix} \chi^\alpha & \xi^\dagger_{\dot\alpha} \end{pmatrix} \begin{pmatrix} 0 & \sigma^\mu \\ \overline{\sigma}^\mu & 0 \end{pmatrix} \begin{pmatrix} 0 \\ \chi^{\dot\alpha\dagger} \end{pmatrix} = \chi^\alpha\sigma^\mu\chi^{\dot\alpha\dagger}$

$\overline{\psi}\gamma^\mu P_L\psi = \begin{pmatrix} \chi^\alpha & \xi^\dagger_{\dot\alpha} \end{pmatrix} \begin{pmatrix} 0 & \sigma^\mu \\ \overline{\sigma}^\mu & 0 \end{pmatrix} \begin{pmatrix} \xi_\alpha \\ 0 \end{pmatrix} = \xi^\dagger_{\dot\alpha}\overline{\sigma}^\mu\xi_\alpha,$

- One has without proof $\xi\chi = \chi\xi$, $\xi\sigma^\mu\chi = -\chi\overline{\sigma}^\mu\xi$, $\xi\sigma^\mu\overline{\sigma}^\nu\chi = -\chi\sigma^\nu\overline{\sigma}^\mu\xi$

- The Majorana condition for a Dirac vector is $\psi_M = \psi_M^C$, which implies $\xi = \chi$ so that one gets $\psi_{ML} = \begin{pmatrix} \xi_\alpha \\ \xi^{\dot\alpha\dagger} \end{pmatrix} = \psi_L + (\psi^C)_R$ and $\overline{\psi}_{ML} = \begin{pmatrix} \xi^\beta & \xi^\dagger_{\dot\beta} \end{pmatrix}$. One can construct a Majorana

mass term with the help of these Majorana spinors:

$$\overline{\psi}_{M\,L}\psi_{M\,L} = \begin{pmatrix}\xi^{\alpha} & \xi^{\dagger}_{\dot{\alpha}}\end{pmatrix}\begin{pmatrix}\xi_{\alpha}\\ \xi^{\dot{\alpha}\dagger}\end{pmatrix} = \xi^{\alpha}\xi_{\alpha} + \xi^{\dagger}_{\dot{\alpha}}\xi^{\dot{\alpha}\dagger} = \xi\xi + \xi^{\dagger}\xi^{\dagger}\,.$$

- A Majorana mass term is only possible for Majorana fermions. Such a mass term would vanish for Dirac fermions: $\overline{\psi}_{R}\psi_{R} = \begin{pmatrix}\chi^{\alpha} & 0\end{pmatrix}\begin{pmatrix}0\\ \chi^{\dot{\alpha}\dagger}\end{pmatrix} = 0$. At the other hand, Dirac mass terms can be constructed with Majorana fermions:

$$\overline{\psi}_{M\,R}\psi_{M\,L} = \begin{pmatrix}\chi^{\alpha} & \chi^{\dagger}_{\dot{\alpha}}\end{pmatrix}\begin{pmatrix}\xi_{\alpha}\\ \xi^{\dot{\alpha}\dagger}\end{pmatrix} = \chi^{\alpha}\xi_{\alpha} + \xi^{\dagger}_{\dot{\alpha}}\chi^{\dot{\alpha}\dagger} = \chi\xi + \chi^{\dagger}\xi^{\dagger}\,.$$

- Physical units

Unless otherwise noted, natural units have been used, where $c = \hbar = k_B = 1$. All physical quantities are expressed in terms energy:[120]

| | |
|---|---|
| energy: | $1\text{GeV}$ |
| temperature | $1\text{GeV} = 1.1605\cdot 10^{13}\,\text{K}$ |
| mass: | $1\text{GeV} = 1.7827\cdot 10^{-24}\,\text{g}$ |
| length: | $1\text{GeV}^{-1} = 1.9733\cdot 10^{-14}\,\text{cm}$ |
| time: | $1\text{GeV}^{-1} = 6.5822\cdot 10^{-25}\,\text{s}$ |
| number density: | $1\text{GeV}^{3} = 1.3014\cdot 10^{41}\,\text{cm}^{-3}$ |
| mass density: | $1\text{GeV}^{4} = 2.2401\cdot 10^{17}\,\text{g}\cdot\text{cm}^{-3}$ |
| cross-section: | $1\text{barn} = 10^{3}\,\text{mbarn} = 10^{-24}\,\text{cm}^{2} = 2568.1\text{GeV}^{-2}$ |

# Appendix B: Gauge Fields

In order to introduce the gauge fields, which are responsible for the electro-weak and strong interactions, one requires that all fields are invariant under local gauge transformation:

$$\phi(x) \to \phi'(x) = U(\alpha)\phi(x) = e^{-i\alpha^a(x)T^a}\phi(x)$$
$$\xi(x) \to \xi'(x) = U(\alpha)\xi(x) = e^{-i\alpha^a(x)T^a}\xi(x)$$

Here $T^a$ are the generators of the gauge groups, which obey the relation $\left[T^a, T^b\right] = if^{abc}T^c$, where $f^{abc}$ are the structure constants.

| gauge group | | often used representation of the generators $T^a$ | gauge fields of this group couple to … |
|---|---|---|---|
| U(1) | $a = 1$ | $\frac{1}{2}Y$ (weak hypercharge) | all fermions, Higgs |
| $SU(2)_L$ | $a = 1,2,3$ | $\frac{1}{2}\sigma^a$ (Pauli matrices) | isospin-doublets (all left-handed fermions, Higgs) |
| SU(3) | $a = 1,\ldots,8$ | $\frac{1}{2}\lambda^a$ (Gell-Mann matrices) | color-triplets (all quarks) |

*Table 30 Gauge Groups*

The requirement of invariance under such a gauge transformation is achieved by replacing all derivatives in the Lagrangian by gauge-covariant derivatives, i.e. the derivatives transforms as $D_\mu\xi(x) \to \left[D_\mu\xi(x)\right]' = U(\alpha)D_\mu\xi(x)$. This leads to these gauge-covariant derivates:

$$D_\mu\phi(x) = \left(\partial_\mu - ig\sum_a A_\mu^a(x)T^a\right)\phi(x)$$
$$D_\mu\xi(x) = \left(\partial_\mu - ig\sum_a A_\mu^a(x)T^a\right)\xi(x)$$

where is the $A_\mu^a$ is the gauge field associated with a particular generator of the gauge group, $g$ is the coupling constant, and $a$ stands for the index of the generator of the gauge group. The gauge field itself transforms as

$$A_\mu^a(x)T^a \to A_\mu'^a(x)T^a = U(\alpha)A_\mu^a(x)T^aU^{-1}(\alpha) - \tfrac{i}{g}\partial_\mu U(\alpha)U^{-1}(\alpha)$$

Depending on the gauge group, the fields $\phi$ and $\xi$ have to be considered to be $n$-dimensional vectors, where $n$ equals the degree of the group. For instance, left-handed

quarks are singlets under U(1): $Q_{U(1)}$, doublets under SU(2)$_L$: $Q_{SU(2)_L} = \begin{pmatrix} u & d \end{pmatrix}^T$, and they form triplets under SU(3): $Q_{SU(3)} = \begin{pmatrix} q_{red} & q_{green} & q_{blue} \end{pmatrix}^T$. Putting everything together, the left-handed quarks become a direct product of all three vectors: $Q = Q_{U(1)} \otimes Q_{SU(2)_L} \otimes Q_{SU(3)}$. This has to be kept in mind when one works with these fields. A useful example is the gauge-covariant derivative for the left-handed quark with respect to the U(1)⊗SU(2)$_L$⊗SU(3) group:

$$D_\mu Q = \left( \partial_\mu - ig_1 B_\mu T_1 - ig_2 \sum_{a=1}^{3} W_\mu^a T_2^a - ig_3 \sum_{a=1}^{8} G_\mu^a T_3^a \right) Q ,$$

where $T_1 = \frac{1}{2} Y \otimes \mathbf{1}_2 \otimes \mathbf{1}_3$, $T_2^a = \mathbf{1}_1 \otimes \frac{1}{2}\sigma^a \otimes \mathbf{1}_3$ and $T_3^a = \mathbf{1}_1 \otimes \mathbf{1}_2 \otimes \frac{1}{2}\boldsymbol{\lambda}^a$, so that the hypercharge operator $Y$ acts on the $Q_{U(1)}$ singlet, the Pauli matrices act one the $Q_{SU(2)_L}$ doublet, and the Gell-Mann matrices act one the $Q_{SU(3)}$ triplet.

# Appendix C: Variation of the Lagrangian of the Wess-Zumino Model under supersymmetry transformation

The Lagrangian which will be considered consists of three parts:

$$\mathcal{L}_{free} = -\partial^\mu \phi^* \partial_\mu \phi - i\xi^\dagger \bar{\sigma}^\mu \partial_\mu \xi + F^* F ,$$

$$\mathcal{L}_{int} = -y\left[\tfrac{1}{2}\phi\xi\xi + \tfrac{1}{2}\phi^*\xi^\dagger\xi^\dagger - \tfrac{1}{2}\phi\phi F - \tfrac{1}{2}\phi^*\phi^* F^*\right], \text{ and}$$

$$\mathcal{L}_{mass} = -m\left[\tfrac{1}{2}\xi\xi + \tfrac{1}{2}\xi^\dagger\xi^\dagger - \phi F - \phi^* F^*\right].$$

The following transformation is going to be applied to all three parts:

$$\delta\phi = \varepsilon\xi \qquad\qquad \delta\phi^* = \varepsilon^\dagger\xi^\dagger$$
$$\delta(\xi)_\alpha = i\left(\sigma^\mu\varepsilon^\dagger\right)_\alpha\partial_\mu\phi + \varepsilon_\alpha F \quad \text{and} \quad \delta\left(\xi^\dagger\right)_{\dot\alpha} = -i\left(\varepsilon\sigma^\mu\right)_{\dot\alpha}\partial_\mu\phi^* + \left(\varepsilon^\dagger\right)_{\dot\alpha}F^*$$
$$\delta F = i\varepsilon^\dagger\bar\sigma^\mu\partial_\mu\xi \qquad\qquad \delta F^* = -i\partial_\mu\xi^\dagger\bar\sigma^\mu\varepsilon$$

In order to calculate the variation of the free Lagrangian it is useful to replace the fermion term by the following expression:

$$-i\xi^\dagger\bar\sigma^\mu\partial_\mu\xi = -\tfrac{1}{2}i\left(\xi^\dagger\bar\sigma^\mu\partial_\mu\xi + \xi^\dagger\bar\sigma^\mu\partial_\mu\xi\right) = -\tfrac{1}{2}i\left(\partial_\mu\left(\xi^\dagger\bar\sigma^\mu\xi\right) - \partial_\mu\xi^\dagger\bar\sigma^\mu\xi + \xi^\dagger\bar\sigma^\mu\partial_\mu\xi\right).$$

The first term is already a total derivative. Since the requirement is that the variation of the Lagrangian vanishes up to total derivatives, this term can be dropped. The variation of the free Lagrangian is:[38]

$$\begin{aligned}
\delta\mathcal{L}_{free} &= -\partial^\mu\delta\phi^*\partial_\mu\phi - \partial^\mu\phi^*\partial_\mu\delta\phi \\
&\quad + \tfrac{1}{2}i\partial_\mu\delta\xi^\dagger\bar\sigma^\mu\xi + \tfrac{1}{2}i\partial_\mu\xi^\dagger\bar\sigma^\mu\delta\xi \\
&\quad - \tfrac{1}{2}i\delta\xi^\dagger\bar\sigma^\mu\partial_\mu\xi - \tfrac{1}{2}i\xi^\dagger\bar\sigma^\mu\partial_\mu\delta\xi \\
&\quad + \delta F^*F + F^*\delta F \\
&= -\partial^\mu\left(\varepsilon^\dagger\xi^\dagger\right)\partial_\mu\phi - \partial^\mu\phi^*\partial_\mu\left(\varepsilon\xi\right) \\
&\quad + \tfrac{1}{2}i\partial_\mu\left(-i\varepsilon\sigma^\nu\partial_\nu\phi^* + \varepsilon^\dagger F^*\right)\bar\sigma^\mu\xi + \tfrac{1}{2}i\partial_\mu\xi^\dagger\bar\sigma^\mu\left(i\sigma^\nu\varepsilon^\dagger\partial_\nu\phi + \varepsilon F\right) \\
&\quad - \tfrac{1}{2}i\left(-i\varepsilon\sigma^\nu\partial_\nu\phi^* + \varepsilon^\dagger F^*\right)\bar\sigma^\mu\partial_\mu\xi - \tfrac{1}{2}i\xi^\dagger\bar\sigma^\mu\partial_\mu\left(i\sigma^\nu\varepsilon^\dagger\partial_\nu\phi + \varepsilon F\right) \\
&\quad + \left(-i\partial_\mu\xi^\dagger\bar\sigma^\mu\varepsilon\right)F + F^*\left(i\varepsilon^\dagger\bar\sigma^\mu\partial_\mu\xi\right)
\end{aligned}$$

Rearranging the terms with $\varepsilon F$ and $\varepsilon^\dagger F^*$ leads to:

$$\begin{aligned}
\delta\mathcal{L}_{free} &= -\partial^\mu\left(\varepsilon^\dagger\xi^\dagger\right)\partial_\mu\phi - \partial^\mu\phi^*\partial_\mu\left(\varepsilon\xi\right) \\
&\quad + \tfrac{1}{2}\partial_\mu\left(\varepsilon\sigma^\nu\partial_\nu\phi^*\right)\bar\sigma^\mu\xi - \tfrac{1}{2}\partial_\mu\xi^\dagger\bar\sigma^\mu\sigma^\nu\varepsilon^\dagger\partial_\nu\phi \\
&\quad - \tfrac{1}{2}\varepsilon\sigma^\nu\partial_\nu\phi^*\bar\sigma^\mu\partial_\mu\xi + \tfrac{1}{2}\xi^\dagger\bar\sigma^\mu\partial_\mu\left(\sigma^\nu\varepsilon^\dagger\partial_\nu\phi\right) \\
&\quad + \tfrac{1}{2}i\partial_\mu\left(\varepsilon^\dagger F^*\right)\bar\sigma^\mu\xi - \tfrac{1}{2}i\partial_\mu\xi^\dagger\bar\sigma^\mu\varepsilon F + \tfrac{1}{2}i\varepsilon^\dagger F^*\bar\sigma^\mu\partial_\mu\xi - \tfrac{1}{2}i\xi^\dagger\bar\sigma^\mu\partial_\mu\left(\varepsilon F\right)
\end{aligned}$$

The last line is as a total derivative:

$$\begin{aligned}\delta\mathcal{L}_{free} &= -\partial^\mu\left(\varepsilon^\dagger\xi^\dagger\right)\partial_\mu\phi - \partial^\mu\phi^*\partial_\mu(\varepsilon\xi)\\ &+\tfrac{1}{2}\partial_\mu\left(\varepsilon\sigma^\nu\partial_\nu\phi^*\right)\bar\sigma^\mu\xi - \tfrac{1}{2}\partial_\mu\xi^\dagger\bar\sigma^\mu\sigma^\nu\varepsilon^\dagger\partial_\nu\phi\\ &-\tfrac{1}{2}\varepsilon\sigma^\nu\partial_\nu\phi^*\bar\sigma^\mu\partial_\mu\xi + \tfrac{1}{2}\xi^\dagger\bar\sigma^\mu\partial_\mu\left(\sigma^\nu\varepsilon^\dagger\partial_\nu\phi\right)\\ &+\tfrac{1}{2}i\partial_\mu\left[\left(\varepsilon^\dagger F^*\right)\bar\sigma^\mu\xi\right] - \tfrac{1}{2}i\partial_\mu\left[\xi^\dagger\bar\sigma^\mu\varepsilon F\right]\end{aligned}$$

Rearranging:

$$\begin{aligned}\delta\mathcal{L}_{free} &= -\partial^\mu\left(\varepsilon^\dagger\xi^\dagger\right)\partial_\mu\phi - \tfrac{1}{2}\partial_\mu\xi^\dagger\bar\sigma^\mu\sigma^\nu\varepsilon^\dagger\partial_\nu\phi + \tfrac{1}{2}\xi^\dagger\bar\sigma^\mu\partial_\mu\left(\sigma^\nu\varepsilon^\dagger\partial_\nu\phi\right)\\ &-\partial^\mu\phi^*\partial_\mu(\varepsilon\xi) - \tfrac{1}{2}\varepsilon\sigma^\nu\partial_\nu\phi^*\bar\sigma^\mu\partial_\mu\xi + \tfrac{1}{2}\partial_\mu\left(\varepsilon\sigma^\nu\partial_\nu\phi^*\right)\bar\sigma^\mu\xi\\ &+\tfrac{1}{2}i\partial_\mu\left[\left(\theta^\dagger F^*\right)\bar\sigma^\mu\xi\right] - \tfrac{1}{2}i\partial_\mu\left[\xi^\dagger\bar\sigma^\mu\theta F\right]\\ &= -\partial_\mu\phi\varepsilon^\dagger\partial^\mu\xi^\dagger - \tfrac{1}{2}\partial_\nu\phi\partial_\mu\xi^\dagger\bar\sigma^\mu\sigma^\nu\varepsilon^\dagger + \tfrac{1}{2}\partial_\mu\partial_\nu\phi\xi^\dagger\bar\sigma^\mu\sigma^\nu\varepsilon^\dagger\\ &-\varepsilon\partial_\mu\xi\partial^\mu\phi^* - \tfrac{1}{2}\varepsilon\sigma^\nu\bar\sigma^\mu\partial_\mu\xi\partial_\nu\phi^* + \tfrac{1}{2}\varepsilon\sigma^\nu\bar\sigma^\mu\xi\partial_\mu\partial_\nu\phi^*\\ &+\tfrac{1}{2}i\partial_\mu\left[\left(\varepsilon^\dagger F^*\right)\bar\sigma^\mu\xi\right] - \tfrac{1}{2}i\partial_\mu\left[\xi^\dagger\bar\sigma^\mu\varepsilon F\right]\end{aligned}$$

With the commutator relations $\sigma^\mu\bar\sigma^\nu + \sigma^\nu\bar\sigma^\mu = -2g^{\mu\nu}\mathbf{1}$ and the fact that the indices can be interchanged within a term, one gets:

$$\begin{aligned}\delta\mathcal{L}_{free} &= -\partial_\mu\phi\varepsilon^\dagger\partial^\mu\xi^\dagger - \tfrac{1}{2}\partial_\nu\phi\partial_\mu\xi^\dagger\bar\sigma^\mu\sigma^\nu\varepsilon^\dagger + \tfrac{1}{2}\partial_\mu\partial_\nu\phi\xi^\dagger\left(-\bar\sigma^\nu\sigma^\mu - 2g^{\mu\nu}\mathbf{1}\right)\varepsilon^\dagger\\ &-\varepsilon\partial_\mu\xi\partial^\mu\phi^* - \tfrac{1}{2}\varepsilon\sigma^\nu\bar\sigma^\mu\partial_\mu\xi\partial_\nu\phi^* + \tfrac{1}{2}\varepsilon\left(-\sigma^\mu\bar\sigma^\nu - 2g^{\mu\nu}\mathbf{1}\right)\xi\partial_\mu\partial_\nu\phi^*\\ &+\tfrac{1}{2}i\partial_\mu\left[\left(\varepsilon^\dagger F^*\right)\bar\sigma^\mu\xi\right] - \tfrac{1}{2}i\partial_\mu\left[\xi^\dagger\bar\sigma^\mu\varepsilon F\right]\\ &= -\partial^\mu\phi\varepsilon^\dagger\partial_\mu\xi^\dagger - \tfrac{1}{2}\partial_\nu\phi\partial_\mu\xi^\dagger\bar\sigma^\mu\sigma^\nu\varepsilon^\dagger - \tfrac{1}{2}\partial_\nu\partial_\mu\phi\xi^\dagger\bar\sigma^\mu\sigma^\nu\varepsilon^\dagger - \partial_\mu\partial^\mu\phi\xi^\dagger\varepsilon^\dagger\\ &-\varepsilon\partial_\mu\xi\partial^\mu\phi^* - \tfrac{1}{2}\varepsilon\sigma^\nu\bar\sigma^\mu\partial_\mu\xi\partial_\nu\phi^* - \tfrac{1}{2}\varepsilon\sigma^\nu\bar\sigma^\mu\xi\partial_\nu\partial_\mu\phi^* - \varepsilon\xi\partial_\mu\partial^\mu\phi^*\\ &+\tfrac{1}{2}i\partial_\mu\left[\left(\theta^\dagger F^*\right)\bar\sigma^\mu\xi\right] - \tfrac{1}{2}i\partial_\mu\left[\xi^\dagger\bar\sigma^\mu\theta F\right]\\ &= -\partial_\mu\left[\partial^\mu\phi\varepsilon^\dagger\xi^\dagger + \tfrac{1}{2}\partial_\nu\phi\xi^\dagger\bar\sigma^\mu\sigma^\nu\varepsilon^\dagger\right]\\ &-\partial_\mu\left[\varepsilon\xi\partial^\mu\phi^* + \tfrac{1}{2}\varepsilon\sigma^\nu\bar\sigma^\mu\xi\partial_\nu\phi^*\right]\\ &+\tfrac{1}{2}i\partial_\mu\left[\left(\varepsilon^\dagger F^*\right)\bar\sigma^\mu\xi\right] - \tfrac{1}{2}i\partial_\mu\left[\xi^\dagger\bar\sigma^\mu\varepsilon F\right]\end{aligned}$$

The mass term gives the following result:

$$
\begin{aligned}
\delta\mathcal{L}_{mass} &= -m\left[\tfrac{1}{2}\delta\xi\xi + \tfrac{1}{2}\xi\delta\xi + \tfrac{1}{2}\delta\xi^{\dagger}\xi^{\dagger} + \tfrac{1}{2}\xi^{\dagger}\delta\xi^{\dagger} - \delta\phi F - \phi\delta F - \delta\phi^{*}F^{*} - \phi^{*}\delta F^{*}\right] \\
&= -m\left[\tfrac{1}{2}i\sigma^{\mu}\varepsilon^{\dagger}\partial_{\mu}\phi\xi + \tfrac{1}{2}\varepsilon F\xi + \tfrac{1}{2}i\xi\sigma^{\mu}\varepsilon^{\dagger}\partial_{\mu}\phi + \tfrac{1}{2}\xi\varepsilon F\right] \\
&\quad + m\left[\tfrac{1}{2}i\varepsilon\sigma^{\mu}\partial_{\mu}\phi^{*}\xi^{\dagger} - \tfrac{1}{2}\varepsilon^{\dagger}F^{*}\xi^{\dagger} + \tfrac{1}{2}i\xi^{\dagger}\varepsilon\sigma^{\mu}\partial_{\mu}\phi^{*} - \tfrac{1}{2}\xi^{\dagger}\varepsilon^{\dagger}F^{*}\right] \\
&\quad + m\left[\varepsilon\xi F + i\phi\varepsilon^{\dagger}\overline{\sigma}^{\mu}\partial_{\mu}\xi + \varepsilon^{\dagger}\xi^{\dagger}F^{*} - i\phi^{*}\partial_{\mu}\xi^{\dagger}\overline{\sigma}^{\mu}\varepsilon\right]
\end{aligned}
$$

Here one makes use of $\varepsilon\xi = \xi\varepsilon$ and $\varepsilon^{\dagger}\xi^{\dagger} = \xi^{\dagger}\varepsilon^{\dagger}$ to eliminate all terms containing the auxiliary field

$$
\begin{aligned}
\delta\mathcal{L}_{mass} &= -m\left[\tfrac{1}{2}i\sigma^{\mu}\varepsilon^{\dagger}\partial_{\mu}\phi\xi + \tfrac{1}{2}i\xi\sigma^{\mu}\varepsilon^{\dagger}\partial_{\mu}\phi\right] \\
&\quad + m\left[\tfrac{1}{2}i\varepsilon\sigma^{\mu}\partial_{\mu}\phi^{*}\xi^{\dagger} + \tfrac{1}{2}i\xi^{\dagger}\varepsilon\sigma^{\mu}\partial_{\mu}\phi^{*}\right] \\
&\quad + m\left[i\phi\varepsilon^{\dagger}\overline{\sigma}^{\mu}\partial_{\mu}\xi - i\phi^{*}\partial_{\mu}\xi^{\dagger}\overline{\sigma}^{\mu}\varepsilon\right]
\end{aligned}
$$

Furthermore one can use[121] $\varepsilon^{\dagger}\overline{\sigma}^{\mu}\xi = -\xi\sigma^{\mu}\varepsilon^{\dagger}$ and $\sigma^{\mu}\varepsilon^{\dagger} = -\varepsilon^{\dagger}\overline{\sigma}^{\mu}$ and rearrange terms to get again a total derivative:

$$
\begin{aligned}
\delta\mathcal{L}_{mass} &= -m\left[\tfrac{1}{2}i\xi\sigma^{\mu}\varepsilon^{\dagger}\partial_{\mu}\phi + \tfrac{1}{2}i\xi\sigma^{\mu}\varepsilon^{\dagger}\partial_{\mu}\phi + i\phi\partial_{\mu}\xi\sigma^{\mu}\varepsilon^{\dagger}\right] \\
&\quad + m\left[\tfrac{1}{2}i\varepsilon\sigma^{\mu}\partial_{\mu}\phi^{*}\xi^{\dagger} + \tfrac{1}{2}i\varepsilon\sigma^{\mu}\partial_{\mu}\phi^{*}\xi^{\dagger} + i\phi^{*}\varepsilon\sigma^{\mu}\partial_{\mu}\xi^{\dagger}\right] \\
&= -m\left[i\xi\sigma^{\mu}\varepsilon^{\dagger}\partial_{\mu}\phi + i\phi\partial_{\mu}\xi\sigma^{\mu}\varepsilon^{\dagger}\right] \\
&\quad + m\left[i\varepsilon\sigma^{\mu}\partial_{\mu}\phi^{*}\xi^{\dagger} + i\phi^{*}\varepsilon\sigma^{\mu}\partial_{\mu}\xi^{\dagger}\right] \\
&= -m\partial_{\mu}\left[i\xi\sigma^{\mu}\varepsilon^{\dagger}\phi\right] + m\partial_{\mu}\left[i\varepsilon\sigma^{\mu}\xi^{\dagger}\phi^{*}\right]
\end{aligned}
$$

The variation of the interaction part of the Lagrangian is

$$
\begin{aligned}
\delta\mathcal{L}_{int} &= -\tfrac{1}{2}y\left[\delta\phi\xi\xi + \phi\delta\xi\xi + \phi\xi\delta\xi\right] \\
&\quad -\tfrac{1}{2}y\left[\delta\phi^{*}\xi^{\dagger}\xi^{\dagger} + \phi^{*}\delta\xi^{\dagger}\xi^{\dagger} + \phi^{*}\xi^{\dagger}\delta\xi^{\dagger}\right] \\
&\quad +\tfrac{1}{2}y\left[\delta\phi\phi F + \phi\delta\phi F + \phi\phi\delta F\right] \\
&\quad +\tfrac{1}{2}y\left[\delta\phi^{*}\phi^{*}F^{*} + \phi^{*}\delta\phi^{*}F^{*} + \phi^{*}\phi^{*}\delta F^{*}\right] \\
&= -\tfrac{1}{2}y\left[\varepsilon\xi\xi\xi + i\phi\sigma^{\mu}\varepsilon^{\dagger}\partial_{\mu}\phi\xi + \phi\varepsilon F\xi + i\phi\xi\sigma^{\mu}\varepsilon^{\dagger}\partial_{\mu}\phi + \phi\xi\varepsilon F\right] \\
&\quad -\tfrac{1}{2}y\left[\varepsilon^{\dagger}\xi^{\dagger}\xi^{\dagger}\xi^{\dagger} - i\phi^{*}\varepsilon\sigma^{\mu}\partial_{\mu}\phi^{*}\xi^{\dagger} + \phi^{*}\varepsilon^{\dagger}F^{*}\xi^{\dagger} - i\phi^{*}\xi^{\dagger}\varepsilon\sigma^{\mu}\partial_{\mu}\phi^{*} + \phi^{*}\xi^{\dagger}\varepsilon^{\dagger}F^{*}\right] \\
&\quad +\tfrac{1}{2}y\left[\varepsilon\xi\phi F + \phi\varepsilon\xi F + i\phi\phi\varepsilon^{\dagger}\overline{\sigma}^{\mu}\partial_{\mu}\xi\right] \\
&\quad +\tfrac{1}{2}y\left[\varepsilon^{\dagger}\xi^{\dagger}\phi^{*}F^{*} + \phi^{*}\varepsilon^{\dagger}\xi^{\dagger}F^{*} - i\phi^{*}\phi^{*}\partial_{\mu}\xi^{\dagger}\overline{\sigma}^{\mu}\varepsilon\right]
\end{aligned}
$$

From the Fierz identity $\chi_{\alpha}(\xi\eta) = -\xi_{\alpha}(\eta\chi) - \eta_{\alpha}(\chi\xi)$ one sees that

$\varepsilon\xi\xi\xi\xi = \varepsilon^{\alpha}\xi_{\alpha}(\xi\xi) = -\varepsilon^{\alpha}\xi_{\alpha}(\xi\xi) - \varepsilon^{\alpha}\xi_{\alpha}(\xi\xi)$ leads to $\varepsilon^{\alpha}\xi_{\alpha}(\xi\xi) = 0$.

The same holds true for $\varepsilon^{\dagger}{}_{\dot{\alpha}}\xi^{\dagger\dot{\alpha}}(\xi^{\dagger}\xi^{\dagger}) = 0$.

Employing again $\varepsilon\xi = \xi\varepsilon$, $\varepsilon^{\dagger}\xi^{\dagger} = \xi^{\dagger}\varepsilon^{\dagger}$, $\varepsilon^{\dagger}\overline{\sigma}^{\mu}\xi = -\xi\sigma^{\mu}\varepsilon^{\dagger}$ and $\sigma^{\mu}\varepsilon^{\dagger} = -\varepsilon^{\dagger}\overline{\sigma}^{\mu}$ and re-arrangement of the remaining terms gives

$$\begin{aligned}
\delta\mathcal{L}_{int} &= -\tfrac{1}{2}y\left[2i\phi\sigma^{\mu}\varepsilon^{\dagger}\partial_{\mu}\phi\xi + 2\phi\varepsilon F\xi\right] \\
&\quad + \tfrac{1}{2}y\left[2i\phi^{*}\varepsilon\sigma^{\mu}\partial_{\mu}\phi^{*}\xi^{\dagger} - 2\phi^{*}\varepsilon^{\dagger}F^{*}\xi^{\dagger}\right] \\
&\quad + \tfrac{1}{2}y\left[2\varepsilon\xi\phi F + i\phi\phi\varepsilon^{\dagger}\overline{\sigma}^{\mu}\partial_{\mu}\xi\right] \\
&\quad + \tfrac{1}{2}y\left[2\varepsilon^{\dagger}\xi^{\dagger}\phi^{*}F^{*} - i\phi^{*}\phi^{*}\partial_{\mu}\xi^{\dagger}\overline{\sigma}^{\mu}\varepsilon\right]
\end{aligned}$$

Simplifying and more rearranging leads to

$$\begin{aligned}
\delta\mathcal{L}_{int} &= \tfrac{1}{2}iy\left[2\phi\partial_{\mu}\phi\varepsilon^{\dagger}\overline{\sigma}^{\mu}\xi + \phi\phi\varepsilon^{\dagger}\overline{\sigma}^{\mu}\partial_{\mu}\xi\right] \\
&\quad + \tfrac{1}{2}iy\left[2\phi^{*}\partial_{\mu}\phi^{*}\varepsilon\sigma^{\mu}\xi^{\dagger} + \phi^{*}\phi^{*}\varepsilon\sigma^{\mu}\partial_{\mu}\xi^{\dagger}\right] \\
&= \tfrac{1}{2}iy\partial_{\mu}\left[\phi\phi\varepsilon^{\dagger}\overline{\sigma}^{\mu}\xi\right] \\
&\quad + \tfrac{1}{2}iy\partial_{\mu}\left[\phi^{*}\phi^{*}\varepsilon\sigma^{\mu}\xi^{\dagger}\right]
\end{aligned}$$

## Appendix D: Eliminating the auxiliary fields

Applying the Euler-Lagrange equations on the total Lagrangian (18) with respect to the auxiliary field $F$ and $F^{*}$ gives $F^{*} + m\phi + \tfrac{1}{2}y\phi\phi = 0$ and $F + m\phi^{*} + \tfrac{1}{2}y\phi^{*}\phi^{*} = 0$ These equations can be plugged into the Lagrangian (18) to eliminate the auxiliary fields:

$$
\begin{aligned}
\mathsf{L} &= -\partial^{\mu}\phi^{*}\partial_{\mu}\phi + \tfrac{1}{2}i\partial_{\mu}\xi^{\dagger}\bar{\sigma}^{\mu}\xi - \tfrac{1}{2}i\xi^{\dagger}\bar{\sigma}^{\mu}\partial_{\mu}\xi + \left(m\phi + \tfrac{1}{2}y\phi\phi\right)\left(m\phi^{*} + \tfrac{1}{2}y\phi^{*}\phi^{*}\right) \\
&\quad - m\left[\tfrac{1}{2}\xi\xi + \tfrac{1}{2}\xi^{\dagger}\xi^{\dagger} + \phi\left(m\phi^{*} + \tfrac{1}{2}y\phi^{*}\phi^{*}\right) + \phi^{*}\left(m\phi + \tfrac{1}{2}y\phi\phi\right)\right] \\
&\quad - y\left[\tfrac{1}{2}\phi\xi\xi + \tfrac{1}{2}\phi^{*}\xi^{\dagger}\xi^{\dagger} + \tfrac{1}{2}\phi\phi\left(m\phi^{*} + \tfrac{1}{2}y\phi^{*}\phi^{*}\right) + \tfrac{1}{2}\phi^{*}\phi^{*}\left(m\phi + \tfrac{1}{2}y\phi\phi\right)\right] \\
&= -\partial^{\mu}\phi^{*}\partial_{\mu}\phi + \tfrac{1}{2}i\partial_{\mu}\xi^{\dagger}\bar{\sigma}^{\mu}\xi - \tfrac{1}{2}i\xi^{\dagger}\bar{\sigma}^{\mu}\partial_{\mu}\xi + m^{2}\phi\phi^{*} + \tfrac{1}{4}y^{2}\phi\phi\phi^{*}\phi^{*} + \tfrac{1}{2}my\phi\phi^{*}\phi^{*} + \tfrac{1}{2}my\phi\phi\phi^{*} \\
&\quad - m\left[\tfrac{1}{2}\xi\xi + \tfrac{1}{2}\xi^{\dagger}\xi^{\dagger}\right] - m^{2}\phi\phi^{*} - \tfrac{1}{2}my\phi\phi^{*}\phi^{*} - m^{2}\phi\phi^{*} - \tfrac{1}{2}my\phi\phi\phi^{*} \\
&\quad - y\left[\tfrac{1}{2}\phi\xi\xi + \tfrac{1}{2}\phi^{*}\xi^{\dagger}\xi^{\dagger}\right] - \tfrac{1}{2}my\phi\phi\phi^{*} - \tfrac{1}{4}y^{2}\phi\phi\phi^{*}\phi^{*} - \tfrac{1}{2}my\phi\phi^{*}\phi^{*} - \tfrac{1}{4}y^{2}\phi\phi\phi^{*}\phi^{*} \\
&= -\partial^{\mu}\phi^{*}\partial_{\mu}\phi + \tfrac{1}{2}i\partial_{\mu}\xi^{\dagger}\bar{\sigma}^{\mu}\xi - \tfrac{1}{2}i\xi^{\dagger}\bar{\sigma}^{\mu}\partial_{\mu}\xi - m\left[\tfrac{1}{2}\xi\xi + \tfrac{1}{2}\xi^{\dagger}\xi^{\dagger}\right] - y\left[\tfrac{1}{2}\phi\xi\xi + \tfrac{1}{2}\phi^{*}\xi^{\dagger}\xi^{\dagger}\right] \\
&\quad - m^{2}\phi\phi^{*} - \tfrac{1}{2}my\phi\phi^{*}\phi^{*} - \tfrac{1}{2}my\phi\phi\phi^{*} - \tfrac{1}{4}y^{2}\phi\phi\phi^{*}\phi^{*}
\end{aligned}
$$

## Appendix E: Replacing the Weyl Spinors by Majorana Spinors

The Weyl spinors $\xi$ of the Lagrangian below can be replaced by Majorana spinors $\psi_M$.

$$
\begin{aligned}
\mathsf{L} &= -\partial^{\mu}\phi^{*}\partial_{\mu}\phi - i\xi^{\dagger}\bar{\sigma}^{\mu}\partial_{\mu}\xi - m\left[\tfrac{1}{2}\xi\xi + \tfrac{1}{2}\xi^{\dagger}\xi^{\dagger}\right] - y\left[\tfrac{1}{2}\phi\xi\xi + \tfrac{1}{2}\phi^{*}\xi^{\dagger}\xi^{\dagger}\right] \\
&\quad - m^{2}\phi\phi^{*} - \tfrac{1}{2}my\phi\phi^{*}\phi^{*} - \tfrac{1}{2}my\phi\phi\phi^{*} - \tfrac{1}{4}y^{2}\phi\phi\phi^{*}\phi^{*}
\end{aligned}
$$

In the first step, the kinetic term for the spinor field in the Lagrangian ($-i\xi^{\dagger}\bar{\sigma}^{\mu}\partial_{\mu}\xi$) can be rewritten in the following way:

$$
\begin{aligned}
-i\xi^{\dagger}\bar{\sigma}^{\mu}\partial_{\mu}\xi &= -\tfrac{1}{2}i\left(\xi^{\dagger}\bar{\sigma}^{\mu}\partial_{\mu}\xi + \xi^{\dagger}\bar{\sigma}^{\mu}\partial_{\mu}\xi\right) = -\tfrac{1}{2}i\left(\partial_{\mu}\left(\xi^{\dagger}\bar{\sigma}^{\mu}\xi\right) - \partial_{\mu}\xi^{\dagger}\bar{\sigma}^{\mu}\xi + \xi^{\dagger}\bar{\sigma}^{\mu}\partial_{\mu}\xi\right) \\
&= -\tfrac{1}{2}i\left(\partial_{\mu}\left(\xi^{\dagger}\bar{\sigma}^{\mu}\xi\right) + \xi\sigma^{\mu}\partial_{\mu}\xi^{\dagger} + \xi^{\dagger}\bar{\sigma}^{\mu}\partial_{\mu}\xi\right) \\
&= -\tfrac{1}{2}i\left(\partial_{\mu}\left(\bar{\psi}_M\gamma^{\mu}P_L\psi\right) + \bar{\psi}_M\gamma^{\mu}P_R\partial_{\mu}\psi_M + \bar{\psi}_M\gamma^{\mu}P_L\partial_{\mu}\psi_M\right) \\
&= -\tfrac{1}{2}i\left(\partial_{\mu}\left(\bar{\psi}_M\gamma^{\mu}P_L\psi_M\right) + \bar{\psi}_M\gamma^{\mu}\partial_{\mu}\psi_M\right)
\end{aligned}
$$

The $\psi_M$ fields are Majorana spinor fields, so that the Majorana condition $\xi = \chi$ was applied in the second to last line. The last line contains a total derivative which can be dropped in the Langrangian since it does not affect the action. Now the entire Lagrangian can be rewritten:

$$
\begin{aligned}
\mathsf{L} &= -\partial^\mu \phi^* \partial_\mu \phi - i\xi^\dagger \bar{\sigma}^\mu \partial_\mu \xi - m\left[\tfrac{1}{2}\xi\xi + \tfrac{1}{2}\xi^\dagger\xi^\dagger\right] - y\left[\tfrac{1}{2}\phi\xi\xi + \tfrac{1}{2}\phi^*\xi^\dagger\xi^\dagger\right] \\
&\quad - m^2\phi\phi^* - \tfrac{1}{2}my\phi\phi^*\phi^* - \tfrac{1}{2}my\phi\phi\phi^* - \tfrac{1}{4}y^2\phi\phi\phi^*\phi^* \\
&= -\partial^\mu \phi^* \partial_\mu \phi - \tfrac{1}{2} i\overline{\psi}_M \gamma^\mu \partial_\mu \psi_M - \tfrac{1}{2} m\left(\overline{\psi}_M P_L \psi_M + \overline{\psi}_M P_R \psi_M\right) - \tfrac{1}{2} y\left[\phi\overline{\psi}_M P_L \psi_M + \phi^*\overline{\psi}_M P_R \psi_M\right] \\
&\quad - m^2\phi\phi^* - \tfrac{1}{2}my\phi\phi^*\phi^* - \tfrac{1}{2}my\phi\phi\phi^* - \tfrac{1}{4}y^2\phi\phi\phi^*\phi^* \\
&= -\partial^\mu \phi^* \partial_\mu \phi - \tfrac{1}{2} i\overline{\psi}_M \gamma^\mu \partial_\mu \psi_M - \tfrac{1}{2} m\overline{\psi}_M \psi_M - \tfrac{1}{4} y\left[\phi\overline{\psi}_M (1-\gamma_5)\psi_M + \phi^*\overline{\psi}_M (1+\gamma_5)\psi_M\right] \\
&\quad - m^2\phi\phi^* - \tfrac{1}{2}my\phi\phi^*\phi^* - \tfrac{1}{2}my\phi\phi\phi^* - \tfrac{1}{4}y^2\phi\phi\phi^*\phi^*
\end{aligned}
$$

Furthermore one can split the complex scalar into its components so that $\phi = \dfrac{A+iB}{\sqrt{2}}$.

$$
\begin{aligned}
\mathsf{L} &= -\tfrac{1}{2}\partial^\mu A\partial_\mu A - \tfrac{1}{2}\partial^\mu B\partial_\mu B - \tfrac{1}{2} i\overline{\psi}_M \gamma^\mu \partial_\mu \psi_M - \tfrac{1}{2} m\overline{\psi}_M \psi_M - \tfrac{1}{4\sqrt{2}} y\left[(A+iB)\overline{\psi}_M (1-\gamma_5)\psi_M + (A-iB)\overline{\psi}_M (1+\gamma_5)\psi_M\right] \\
&\quad - \tfrac{1}{2}m^2\left(A^2+B^2\right) - \tfrac{1}{2\cdot 2\sqrt{2}} my\left[(A+iB)(A-iB)^2 + (A+iB)^2(A-iB)\right] - \tfrac{1}{4\cdot 4} y^2\left(A^2+B^2\right)^2 \\
&= -\tfrac{1}{2}\partial^\mu A\partial_\mu A - \tfrac{1}{2}\partial^\mu B\partial_\mu B - \tfrac{1}{2} i\overline{\psi}_M \gamma^\mu \partial_\mu \psi_M - \tfrac{1}{2} m\overline{\psi}_M \psi_M \\
&\quad - \tfrac{1}{4\sqrt{2}} y\left[A\overline{\psi}_M \psi_M - A\overline{\psi}_M \gamma^5 \psi_M + iB\overline{\psi}_M \psi_M - iB\overline{\psi}_M \gamma^5 \psi_M + A\overline{\psi}_M \psi_M + A\overline{\psi}_M \gamma^5 \psi_M - iB\overline{\psi}_M \psi_M - iB\overline{\psi}_M \gamma^5 \psi_M\right] \\
&\quad - \tfrac{1}{2}m^2\left(A^2+B^2\right) - \tfrac{1}{2\cdot 2\sqrt{2}} my\left[(A+iB)\left(A^2 - 2iAB - B^2\right) + \left(A^2 + 2iAB - B^2\right)(A-iB)\right] - \tfrac{1}{4\cdot 4} y^2\left(A^4 + 2A^2B^2 + B^4\right) \\
&= -\tfrac{1}{2}\partial^\mu A\partial_\mu A - \tfrac{1}{2}\partial^\mu B\partial_\mu B - \tfrac{1}{2} i\overline{\psi}_M \gamma^\mu \partial_\mu \psi_M - \tfrac{1}{2} m\overline{\psi}_M \psi_M - \tfrac{1}{4\sqrt{2}} y\left[2A\overline{\psi}_M \psi_M - i2B\overline{\psi}_M \gamma^5 \psi_M\right] \\
&\quad - \tfrac{1}{2}m^2\left(A^2+B^2\right) - \tfrac{1}{2\cdot 2\sqrt{2}} my\left[2A^3 - 2AB^2 + 4AB^2\right] - \tfrac{1}{4\cdot 4} y^2\left(A^4 + 2A^2B^2 + B^4\right) \\
&= -\tfrac{1}{2}\partial^\mu A\partial_\mu A - \tfrac{1}{2}\partial^\mu B\partial_\mu B - \tfrac{1}{2} i\overline{\psi}_M \gamma^\mu \partial_\mu \psi_M - \tfrac{1}{2} m\overline{\psi}_M \psi_M - \tfrac{1}{2\sqrt{2}} y\left[A\overline{\psi}_M \psi_M - iB\overline{\psi}_M \gamma^5 \psi_M\right] \\
&\quad - \tfrac{1}{2}m^2\left(A^2+B^2\right) - \tfrac{1}{2\sqrt{2}} my\left[A^3 + AB^2\right] - \tfrac{1}{4\cdot 4} y^2\left(A^4 + 2A^2B^2 + B^4\right)
\end{aligned}
$$

# Appendix F: First Order Loop corrections for the imaginary part of the scalar field of the Wess-Zumino Model

| | |
|---|---|
| 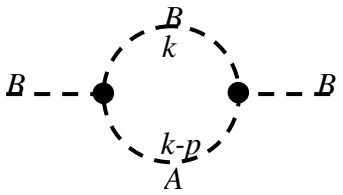 | $-iM_{(1)} = 2 \cdot 2 \cdot \left(-\frac{imy}{2\sqrt{2}}\right) \cdot \left(-\frac{imy}{2\sqrt{2}}\right) \cdot \int d^4k \frac{i^2}{\left[k^2 - m^2\right] \cdot \left[(k-p)^2 - m^2\right]}$ |
| 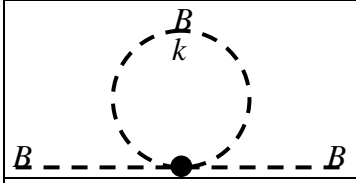 | $-iM_{(2)} = 4 \cdot 3 \cdot \frac{-iy^2}{16} \cdot \int d^4k \frac{i}{\left[k^2 - m^2\right]}$ |
| 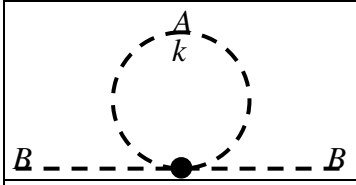 | $-iM_{(3)} = 2 \cdot \frac{-iy^2}{8} \cdot \int d^4k \frac{i}{\left[k^2 - m^2\right]}$ |
| 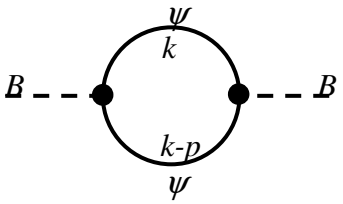 | $-iM_{(4)} = (-1) \cdot 2! \cdot \frac{+iiy}{2\sqrt{2}} \cdot \frac{+iiy}{2\sqrt{2}} \cdot \int d^4k \cdot \mathrm{Tr}\left[\gamma_5 \frac{i}{\not k - m} \gamma_5 \frac{i}{(\not k - \not p) - m}\right]$ |

*Table 31 First Order Loop corrections for the imaginary part of the scalar field of the Wess-Zumino Model*

$M_{(1)}$ is only logarithmic divergent, so one does not have to care about it. The remaining three diagrams lead to[43]

$$
\begin{aligned}
-iM_{(2)(3)(4)} &= \frac{12}{16} y^2 \int d^4k \frac{1}{k^2-m^2} + \frac{2}{8} y^2 \int d^4k \frac{1}{k^2-m^2} + \frac{1}{4} y^2 \int d^4k \cdot \mathrm{Tr} \frac{\gamma^5 [\not{k}+m] \cdot \gamma^5 [(\not{k}-\not{p})+m]}{[k^2-m^2] \cdot [(k-p)^2-m^2]} \\
&= y^2 \int d^4k \frac{1}{k^2-m^2} + \frac{1}{4} y^2 \int d^4k \cdot \mathrm{Tr} \frac{(\gamma^5)^2 [-\not{k}+m] \cdot [(\not{k}-\not{p})+m]}{[k^2-m^2] \cdot [(k-p)^2-m^2]} \\
&= y^2 \int d^4k \frac{1}{k^2-m^2} + \frac{1}{4} y^2 \int d^4k \frac{\mathrm{Tr}[-\not{k}\not{k} + \not{k}\not{p} - \not{p}m + m^2]}{[k^2-m^2] \cdot [(k-p)^2-m^2]} \\
&= y^2 \int d^4k \frac{1}{k^2-m^2} - \frac{1}{4} y^2 \int d^4k \frac{4k^2 - 4kp - 4m^2}{[k^2-m^2] \cdot [(k-p)^2-m^2]} \\
&= y^2 \int d^4k \frac{1}{k^2-m^2} - \frac{1}{4} y^2 \int d^4k \frac{2[(k^2-m^2) + ((k-p)^2-m^2) - p^2 - 4m^2]}{[k^2-m^2] \cdot [(k-p)^2-m^2]} \\
&= y^2 \int d^4k \frac{1}{k^2-m^2} - \frac{1}{2} y^2 \int d^4k \left[ \frac{1}{(k-p)^2-m^2} + \frac{1}{k^2-m^2} + \frac{-4m^2-p^2}{[k^2-m^2] \cdot [(k-p)^2-m^2]} \right]
\end{aligned}
$$

where the last term of the second integral is again only logarithmic divergent. The other parts cancel (using a change of variables for the first term of the second integral $k \to k' = k + p$ ), so that there are no quadratic divergences anymore:[43]

$$
\begin{aligned}
-iM_{(2)(3)(4)} &= y^2 \int d^4k \frac{1}{k^2-m^2} - \frac{1}{2} y^2 \int d^4k \cdot \frac{1}{(k-p)^2-m^2} - \frac{1}{2} y^2 \int d^4k \cdot \frac{1}{k^2-m^2} \\
&= y^2 \int d^4k \frac{1}{k^2-m^2} - \frac{1}{2} y^2 \int d^4k' \cdot \frac{1}{k'^2-m^2} - \frac{1}{2} y^2 \int d^4k \cdot \frac{1}{k^2-m^2} \\
&= 0
\end{aligned}
$$

# Appendix G: Recovering the original Lagrangian after the use of the Superpotential

If one uses the superpotential $W = \frac{1}{2} m\phi\phi + \frac{1}{6} y\phi\phi\phi$ with the Lagrangian $\mathsf{L} = -\partial^\mu \phi^{*i} \partial_\mu \phi_i - i\xi^{\dagger i} \bar{\sigma}^\mu \partial_\mu \xi_i - \frac{1}{2}\left(W^{ij}\xi_i\xi_j + W^{*ij}\xi^{\dagger i}\xi^{\dagger j}\right) - W^i W_i^*$, then one gets the original Lagrangian (24):

$$
\begin{aligned}
\mathcal{L} &= -\partial^\mu \phi^* \partial_\mu \phi + \tfrac{1}{2} i \partial_\mu \xi^\dagger \bar{\sigma}^\mu \xi - \tfrac{1}{2} i \xi^\dagger \bar{\sigma}^\mu \partial_\mu \xi - \tfrac{1}{2} \left( W'' \xi\xi + W^{*\prime\prime} \xi^\dagger \xi^\dagger \right) - W' W^{*\prime} \\
&= -\partial^\mu \phi^* \partial_\mu \phi + \tfrac{1}{2} i \partial_\mu \xi^\dagger \bar{\sigma}^\mu \xi - \tfrac{1}{2} i \xi^\dagger \bar{\sigma}^\mu \partial_\mu \xi - \tfrac{1}{2} \left( m\xi\xi + y\phi\xi\xi + m\xi^\dagger \xi^\dagger + y\phi^* \xi^\dagger \xi^\dagger \right) \\
&\quad - \left( m\phi + \tfrac{1}{2} y\phi\phi \right) \left( m\phi^* + \tfrac{1}{2} y\phi^* \phi^* \right) \\
&= -\partial^\mu \phi^* \partial_\mu \phi + \tfrac{1}{2} i \partial_\mu \xi^\dagger \bar{\sigma}^\mu \xi - \tfrac{1}{2} i \xi^\dagger \bar{\sigma}^\mu \partial_\mu \xi - m \left[ \tfrac{1}{2} \xi\xi + \tfrac{1}{2} \xi^\dagger \xi^\dagger \right] - y \left[ \tfrac{1}{2} \phi\xi\xi + \tfrac{1}{2} \phi^* \xi^\dagger \xi^\dagger \right] \\
&\quad - m^2 \phi\phi^* - \tfrac{1}{2} my\phi\phi^*\phi^* - \tfrac{1}{2} my\phi\phi\phi^* - \tfrac{1}{4} y^2 \phi\phi\phi^*\phi^*
\end{aligned}
$$

# Appendix H: An important property of the superpotential

The superpotential cannot contain the complex conjugate of the scalar field $\phi^*$, only the scalar field $\phi$ itself, otherwise the Lagrangian would not be SUSY invariant anymore. This can be seen by taking the variation of the relevant parts of the Lagrangian:[48]

$$
\begin{aligned}
\delta\mathcal{L} &= \sum_{i,j} \delta W^{ij} \xi_i \xi_j + \ldots = \sum_{i,j,k} \frac{\delta W^{ij}}{\delta \phi_k} \delta\phi_k \xi_i \xi_j + \sum_{i,j,k} \frac{\delta W^{ij}}{\delta \phi^{k*}} \delta\phi^{k*} \xi_i \xi_j + \ldots \\
&= \sum_{i,j,k} \frac{\delta W^{ij}}{\delta \phi_k} (\varepsilon\xi_k)(\xi_i \xi_j) + \sum_{i,j,k} \frac{\delta W^{ij}}{\delta \phi^{k*}} (\varepsilon^\dagger \xi^{k\dagger})(\xi_i \xi_j) + \ldots
\end{aligned}
$$

Let's take a look at the first sum.

$$
\frac{\delta W^{ij}}{\delta \phi_k} (\varepsilon\xi_k)(\xi_i \xi_j) + \frac{\delta W^{ik}}{\delta \phi_j} (\varepsilon\xi_j)(\xi_i \xi_k) + \frac{\delta W^{ji}}{\delta \phi_k} (\varepsilon\xi_k)(\xi_j \xi_i) + \frac{\delta W^{jk}}{\delta \phi_i} (\varepsilon\xi_i)(\xi_j \xi_k) + \frac{\delta W^{ki}}{\delta \phi_j} (\varepsilon\xi_j)(\xi_k \xi_i) + \frac{\delta W^{kj}}{\delta \phi_i} (\varepsilon\xi_i)(\xi_k \xi_j)
$$

The term $\dfrac{\delta W^{ij}}{\delta \phi_k}$ is of course totally symmetric under the exchange of the indices i,j,k, so that one gets $\dfrac{\delta W^{ij}}{\delta \phi_k} \left[ (\varepsilon\xi_k)(\xi_i \xi_j) + (\varepsilon\xi_j)(\xi_i \xi_k) + (\varepsilon\xi_k)(\xi_j \xi_i) + (\varepsilon\xi_i)(\xi_j \xi_k) + (\varepsilon\xi_j)(\xi_k \xi_i) + (\varepsilon\xi_i)(\xi_k \xi_j) \right]$.

With the help of the Fierz identity $\xi_{i\alpha} (\xi_j \xi_k) + \xi_{k\alpha} (\xi_i \xi_j) + \xi_{j\alpha} (\xi_k \xi_i) = 0$ one sees that the entire expression vanishes.

A similar relationship that contains one $\xi^{\dagger}$ does not exist. Therefore the second sum of $\delta\mathcal{L}$ from above cannot be cancelled, and $\delta\mathcal{L}$ would not vanish (i.e. such a Lagrangian is not SUSY invariant anymore). In order to avoid this, the superpotential cannot contain any complex conjugated fields $\phi^{*}$.[48]

## Appendix I: Neutrino oscillation and Neutrino mass

If one uses the mass term of the Standard Model Lagrangian (40), one gets $\mathcal{L}_{SM} = y_N^{ij}\left(L_i^{1\dagger}H_1^C + L_i^{2\dagger}H_2^C\right)\nu_{Rj}^{\dagger} + h.c.$ where the vacuum expectation values of the Higgs doublets are $\left\langle H_1^C\right\rangle = \frac{v}{\sqrt{2}}$ and $\left\langle H_2^C\right\rangle = 0$, so that mass term becomes $y_N^{ij}\nu_{Li}^{\dagger}\frac{v}{\sqrt{2}}\nu_{Rj}^{\dagger} + h.c.$,[122] where the $\nu$'s are two component Weyl spinors, and the indices *i, j* are in the family space. The Yukawa coupling matrix $y_N^{ij}$ can be multiplied with the vacuum expectation value of the Higgs to get a mass matrix $m^{ij} = y_N^{ij}\frac{v}{\sqrt{2}}$. Since this matrix contains off-diagonal elements, the neutrino states in $\nu_{Li}^{\dagger}m^{ij}\nu_{Rj}^{\dagger}$ cannot be mass-eigenstates (the states that can be physically detected). In order to find them, $m^{ij}$ needs to be diagonalized. The mass matrix can split up into a Hermitian matrix *H* and some unitary matrix *U*. The matrix *H* can be diagonalized into $M = C_L^{\dagger}HC_L$ by another unitary matrix $C_L$, so that $H = C_L M C_L^{\dagger}$ and finally $m = HU = C_L M C_L^{\dagger}U = C_L M C_R^{\dagger}$.[122] This leads to mixed eigenstates $\nu_L^{\dagger}m\nu_R^{\dagger} = \nu_L^{\dagger}C_L M C_R^{\dagger}\nu_R^{\dagger} = \left(C_L^{\dagger}\nu_L\right)^{\dagger}M\left(\nu_R C_R\right)^{\dagger} = \nu_L'^{\dagger}M\nu_R'^{\dagger}$, where the new mass-eigenstates are $\nu'_{L\alpha} = C_L^{\alpha i\dagger}\nu_{Li}$ and $\nu'_{R\alpha} = \nu_{Ri}C_R^{\alpha i}$.[122] The gauge-eigenstates can also be expressed in terms of mass-eigenstates: $\nu_{Li} = C_L^{i\alpha}\nu'_{L\alpha}$ and $\nu_{Ri} = C_R^{i\alpha\dagger}\nu'_{R\alpha}$.

One can consider a simplified case of just two states, with the gauge-eigenstates $|\nu_{e,\mu}\rangle$ and the mass-eigenstates $|\nu_{1,2}\rangle$ so that $\begin{pmatrix}|\nu_e\rangle\\|\nu_\mu\rangle\end{pmatrix}=\begin{pmatrix}\cos\delta & \sin\delta\\ -\sin\delta & \cos\delta\end{pmatrix}\begin{pmatrix}|\nu_1'\rangle\\|\nu_2'\rangle\end{pmatrix}$. If one considers an example where a neutrino is initially an electron-neutrino $|\nu_e(t_0=0)\rangle$, it will be in a state $|\nu_e(t)\rangle = e^{-iHt}|\nu_e(t_0=0)\rangle$ at a later time *t*, where $e^{-iHt}$ is the time evolution operator. The probability for this neutrino to be a muon-neutrino at time *t* is given by $P=\left|\langle \nu_\mu|\nu_e(t)\rangle\right|^2=\left|\langle\nu_\mu|e^{-iHt}|\nu_e(0)\rangle\right|^2$. The electron-neutrino gauge-eigenstate can be split into its two mass-eigenstates, and the eigenvalues of the Hamilton operator *H* can be used for each mass-eigenstate: $P=\left|e^{-iE_1t}\cos\delta\langle\nu_\mu|\nu_1'\rangle+e^{-iE_2t}\sin\delta\langle\nu_\mu|\nu_2'\rangle\right|^2$. The first matrix element can be evaluated by expanding the muon-neutrino state into its mass-eigenstates, and one gets $\langle\nu_\mu|\nu_1'\rangle=-\sin\delta\langle\nu_1'|\nu_1'\rangle+\cos\delta\langle\nu_2'|\nu_1'\rangle=-\sin\delta$. The second matrix elements becomes $\langle\nu_\mu|\nu_2'\rangle=\cos\delta$, so that the transition probability is

$$P=\left|-e^{-iE_1t}\cos\delta\sin\delta+e^{-iE_2t}\sin\delta\cos\delta\right|^2=\sin^2\delta\cos^2\delta\left(e^{-iE_2t}-e^{-iE_1t}\right)\left(e^{iE_2t}-e^{iE_1t}\right)$$
$$=\tfrac{1}{4}\sin^2 2\delta\left(1-e^{-i(E_2-E_1)t}-e^{i(E_2-E_1)t}+1\right)=\tfrac{1}{4}\sin^2 2\delta\left(2-2\cos((E_2-E)t)\right)=\sin^2 2\delta\sin^2\left(\tfrac{E_2-E_1}{2}t\right).$$

Since the neutrino is an ultra-relativistic particle for which $p>>m$, the neutrino energies can be approximated to $E=\sqrt{p^2+m^2}\approx p+\frac{m^2}{2p}$, so that $E_2-E_1\approx\frac{m_2^2-m_1^2}{2p}$, and the time can be replaced by the traveled distance $L=ct$.It follows the transition probability at a distance *L*: $P=\sin^2 2\delta\sin^2\left(\frac{m_2^2-m_1^2}{4p}L\right)$. [123]

Since such flavor changes (oscillations) have been observed, it is clear that there must be a mass difference between different types of neutrinos. This implies that at least one neutrino flavor has mass, which most likely means that all of them have mass.

The question of the nature of the neutrino has not been answered yet, i.e. it is not clear whether the neutrino is a Dirac or a Majorana fermion. In the latter case, the Lagrangian allows the neutrino to have a Majorana mass term, besides the usual Dirac mass term. A mixture of both mass terms leads to the so-called seesaw mechanism, which is described below.

The Dirac mass term is $\mathsf{L}_D = m_D \nu_L \nu_R + h.c.$, which can be contructed from Dirac or Majorana fermions (see appendix A). If the neutrino is a Majorana fermion, it is possible to add a Majorana mass term for the right-handed neutrino: $\mathsf{L}_M = \frac{1}{2} m_L \nu_R \nu_R + h.c.$ This is only possible for the right-handed neutrino, since it does not belong to any gauge group (unlike e.g. the left-handed neutrino, or the electron), so it does not break any gauge symmetry. If it did belong to a gauge group, then this term would leave a net value of the associated quantum numbers.

Combining both masses results in $\mathsf{L} = \frac{1}{2}\begin{pmatrix}\nu_L & \nu_R\end{pmatrix}\begin{pmatrix}0 & m_D \\ m_D & m_R\end{pmatrix}\begin{pmatrix}\nu_L \\ \nu_R\end{pmatrix} + h.c.$ Assuming that $m_R >> m_D$, the mass matrix gets the eigenvalues $\lambda_{1,2} = \frac{m_R}{2} \pm \sqrt{\frac{m_R^2}{4} + m_D^2} \approx \frac{m_R}{2} \pm \left(\frac{m_R}{2} + \frac{m_D^2}{m_R}\right)$, so that $\lambda_1 \approx -\frac{m_D^2}{m_R}$ and $\lambda_2 \approx m_R$. The eigenvectors are $a_1 \approx \begin{pmatrix}-\frac{m_R}{m_D} & 1\end{pmatrix}^T$ and $a_2 \approx \begin{pmatrix}\frac{m_D}{m_R} & 1\end{pmatrix}^T$, so that the rotation matrix is $C \approx \begin{pmatrix}-\frac{m_R}{m_D} & \frac{m_D}{m_R} \\ 1 & 1\end{pmatrix}$. The Lagrangian becomes

$$\mathsf{L} = \tfrac{1}{2}\begin{pmatrix}\nu_L & \nu_R\end{pmatrix}CC^{-1}\begin{pmatrix}0 & m_D\\ m_D & m_R\end{pmatrix}CC^{-1}\begin{pmatrix}\nu_L\\ \nu_R\end{pmatrix} + h.c. \approx \tfrac{1}{2}\begin{pmatrix}\nu_1 & \nu_2\end{pmatrix}\begin{pmatrix}-\frac{m_D^2}{m_R} & 0\\ 0 & m_R\end{pmatrix}\begin{pmatrix}\nu_1\\ \nu_2\end{pmatrix} + h.c.$$ with

$$\begin{pmatrix}\nu_1 & \nu_2\end{pmatrix} = \begin{pmatrix}\nu_L & \nu_R\end{pmatrix}C \approx \begin{pmatrix}\nu_L & \nu_R\end{pmatrix}\begin{pmatrix}-\frac{m_R}{m_D} & \frac{m_D}{m_R}\\ 1 & 1\end{pmatrix} = \begin{pmatrix}-\frac{m_R}{m_D}\nu_L + \nu_R & \frac{m_D}{m_R}\nu_L + \nu_R\end{pmatrix}.$$ One can see that, the mass-eigenstate $\nu_1$ is dominated by $\nu_L$, and the mass-eigenstate $\nu_2$ is dominated by $\nu_R$, if $m_R >> m_D$. Since the right-handed neutrino does not participate in any interaction (except gravity), the second mass-eigenstate $\nu_2$ becomes a so-called "sterile" neutrino.

This mechanism has the interesting feature, that the mass $\frac{m_D^2}{m_R}$ of $\nu_1$ becomes smaller, if the mass $m_R$ of $\nu_2$ becomes bigger (that is where the name "seesaw" mechanism comes from). It may explain why the observed neutrinos (which are the $\nu_1$ eigenstates) have such a small mass – a mass which is several orders of magnitude lower than other fermions.

## Appendix J: Gauge boson mass eigenstates and the Higgs

The gauge bosons gain their masses through the $D^\mu H^* D_\mu H$ term of the Langrangian, where $H = \begin{pmatrix}H^+\\ H^0\end{pmatrix}$ and the vacuum expectation value is $\langle H\rangle = \begin{pmatrix}0\\ \frac{v}{\sqrt{2}}\end{pmatrix}$. Here is the essential part of the gauge covariant derivative

$$\langle D_\mu H\rangle = \left(-ig_1 B_\mu \tfrac{1}{2}Y - ig_2\sum_{a=1}^{3} W_\mu^a \tfrac{1}{2}\sigma^a\right)\langle H\rangle = -\frac{i}{2}\begin{pmatrix}g_1 B_\mu + g_2 W_\mu^3 & g_2\left(W_\mu^1 - iW_\mu^2\right)\\ g_2\left(W_\mu^1 + iW_\mu^2\right) & g_1 B_\mu - g_2 W_\mu^3\end{pmatrix}\begin{pmatrix}0\\ \frac{v}{\sqrt{2}}\end{pmatrix},$$
$$= -\frac{iv}{2\sqrt{2}}\begin{pmatrix}\sqrt{2}g_2 W_\mu^+\\ g_1 B_\mu - g_2 W_\mu^3\end{pmatrix}$$

where the mass eigenstates $W_\mu^+ = \frac{1}{\sqrt{2}}\left(W_\mu^1 - iW_\mu^2\right)$ and $W_\mu^- = W_\mu^{+^*} = \frac{1}{\sqrt{2}}\left(W_\mu^1 + iW_\mu^2\right)$ were used for the last step. It follows that

$$\left\langle \left(D^\mu H\right)^* D_\mu H \right\rangle = \frac{v^2}{8}\left[2g_2^2 W^{+\mu^*} W_\mu^+ + \left(-ig_1 B^\mu + ig_2 W^{3\mu}\right)\left(ig_1 B_\mu - ig_2 W_\mu^3\right)\right]$$
$$= \frac{v^2}{8} g_2^2 \left[W^{+\mu^*} W_\mu^+ + W^{-\mu} W_\mu^{-^*}\right] + \frac{v^2}{8}\left[g_1^2 B^\mu B_\mu - g_1 g_2 B^\mu W_\mu^3 - g_1 g_2 B_\mu W^{3\mu} + g_2^2 W^{3\mu} W_\mu^3\right]$$

This means that the charged vector bosons acquire a mass of $\frac{1}{2} v g_2$. The other parts of the Langrangian include a mixture of $B_\mu$ and $W_\mu^3$ that can be put into a matrix $\frac{v^2}{8}\begin{pmatrix} B^\mu & W^{3\mu} \end{pmatrix}\begin{pmatrix} g_1^2 & -g_1 g_2 \\ -g_1 g_2 & g_2^2 \end{pmatrix}\begin{pmatrix} B_\mu \\ W_\mu^3 \end{pmatrix}$. In order to find the mass terms one has to diagonalize this matrix, which leads to a rotation in the gauge fields: The eigenvalues of the matrix are 0 and $g_1^2 + g_2^2$, and the eigenvectors are $\frac{1}{\sqrt{g_1^2 + g_2^2}}\begin{pmatrix} g_2 \\ g_1 \end{pmatrix}$ and $\frac{1}{\sqrt{g_1^2 + g_2^2}}\begin{pmatrix} g_1 \\ -g_2 \end{pmatrix}$, so that the rotation matrix is $U = \frac{1}{\sqrt{g_1^2 + g_2^2}}\begin{pmatrix} g_2 & g_1 \\ g_1 & -g_2 \end{pmatrix} = U^{-1}$. Therefore one gets with $\frac{v^2}{8}\begin{pmatrix} B^\mu & W^{3\mu} \end{pmatrix} U \cdot U^{-1}\begin{pmatrix} g_1^2 & -g_1 g_2 \\ -g_1 g_2 & g_2^2 \end{pmatrix} U \cdot U^{-1}\begin{pmatrix} B_\mu \\ W_\mu^3 \end{pmatrix}$ a new mass matrix $\begin{pmatrix} 0 & 0 \\ 0 & g_1^2 + g_2^2 \end{pmatrix}$ and mass eigenstates $U^{-1}\begin{pmatrix} B_\mu \\ W_\mu^3 \end{pmatrix} = \frac{1}{\sqrt{g_1^2 + g_2^2}}\begin{pmatrix} g_2 B_\mu + g_1 W_\mu^3 \\ g_1 B_\mu - g_2 W_\mu^3 \end{pmatrix} = \begin{pmatrix} A^\mu \\ Z^\mu \end{pmatrix}$, which can be identified as the photon and the neutral Z vector boson. The mass matrix also shows that the photon is indeed massless, and the Z gets a mass of $\frac{v}{2}\sqrt{g_1^2 + g_2^2}$. Note, that the rotation matrix is sometimes expressed in terms of the so-called Weinberg angle or weak angle: $U = \begin{pmatrix} \cos\vartheta_W & \sin\vartheta_W \\ \sin\vartheta_W & -\cos\vartheta_W \end{pmatrix}$

# Appendix K: Pion Decay

One can show in a short calculation that the decay channel of pions into electrons is indeed suppressed, even though one would expect this to be the dominant channel, since the electron has a much smaller mass than the muon. The calculation is an application of equation (39): The important term of the Lagrangian is $-i\xi^{\dagger i}\bar{\sigma}^{\mu}D_{\mu}\xi_i$, where the weak-interaction part of the gauge-covariant derivative is $-ig_2\sum_{a=1}^{3}W_{\mu}^{a}\frac{1}{2}\sigma^{a}$, which leads to the following term in the Lagrangian: $\frac{1}{2}g_2\xi^{\dagger i}\bar{\sigma}^{\mu}\sum_{a=1}^{3}W_{\mu}^{a}\sigma^{a}\xi_i$ (note that the indices have been reduced to a minimum, but one has to keep in mind that the first Pauli matrix acts in spinor space, while the second one exists in SU(2) space). Using only the relevant first two terms of the sum gives the following expression:

$$\begin{aligned}
\mathsf{L} &= \tfrac{1}{2}g_2\xi^{\dagger i}\bar{\sigma}^{\mu}\left(W_{\mu}^{1}\sigma^{1}+W_{\mu}^{2}\sigma^{2}\right)\xi_i = \tfrac{1}{2}g_2\begin{pmatrix}\nu_l^{\dagger} & l^{\dagger}\end{pmatrix}_L\bar{\sigma}^{\mu}\begin{pmatrix}0 & W_{\mu}^{1}-iW_{\mu}^{2}\\ W_{\mu}^{1}+iW_{\mu}^{2} & 0\end{pmatrix}\begin{pmatrix}\nu_l\\ l\end{pmatrix}_L \\
&= \tfrac{1}{\sqrt{2}}g_2\begin{pmatrix}\nu_l^{\dagger} & l^{\dagger}\end{pmatrix}_L\bar{\sigma}^{\mu}\begin{pmatrix}0 & W_{\mu}^{+}\\ W_{\mu}^{-} & 0\end{pmatrix}\begin{pmatrix}\nu_l\\ l\end{pmatrix}_L = \tfrac{1}{\sqrt{2}}g_2\left(\nu_{l\,L}^{\dagger}\bar{\sigma}^{\mu}W_{\mu}^{+}l_L+l^{\dagger}{}_L\bar{\sigma}^{\mu}W_{\mu}^{-}\nu_{l\,L}\right) \\
&= \tfrac{1}{\sqrt{2}}g_2\left(\overline{\psi}_{\nu_l}\gamma^{\mu}W_{\mu}^{+}P_L\psi_l+\overline{\psi}_l\gamma^{\mu}W_{\mu}^{-}P_L\psi_{\nu_l}\right)
\end{aligned}$$

where the last line uses Dirac spinors instead of Weyl spinors. This transition between Dirac and Weyl spinors was shown in Appendix A. The first part of the last line of the Lagrangian above can be interpreted, e.g. as an incoming muon interacting with a $W^{+}$ turning into a neutrino, while the second part can be seen as an incoming neutrino interacting with a $W^{-}$ turning into a muon, i.e. $\nu_{\mu}W^{-}\rightarrow\mu^{-}$. An important observation

can be made from the last couple of equations: Only left-handed (in the literature also referred to as left-chiral) particles participate in the weak interaction.

The pion is a spin 0 particle, therefore the total spin of its decay products must be zero as well. Let's consider the decay $\pi^- \to W^- \to \mu^- \bar{\nu}_\mu$. The last step (the decay of the $W^-$) is governed by the same Lagrangian as the reaction $\nu_\mu W^- \to \mu^-$, while the outgoing anti-neutrino $\bar{\nu}_\mu$ is right-handed, and the incoming neutrino $\nu_\mu$ is left-handed (as required by the Lagrangian). The relationship between left-handed neutrino and the right-handed anti-neutrino comes from the crossing symmetry.

From the rest frame of the pion one gets the following picture:

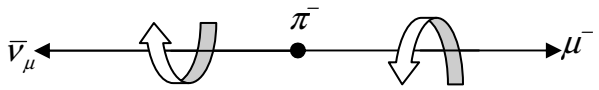


*Figure 37 Pion decay*

As mentioned above, this is a weak decay, so that the outgoing anti-neutrino must be right-handed. Also, the anti-neutrino is almost massless and travels with almost speed of light ($E >> m$). In the limit of zero mass, a right-handed state is identically with a positive helicity (spin and momentum are in the same direction). The right-handed projection of the Dirac spinor (in Weyl representation) for the positive helicity state of the anti-neutrino is[124]

$$P_R\begin{pmatrix} 0 \\ \frac{1}{\sqrt{2}}\left(\sqrt{E_\nu + M_\nu} - \sqrt{E_\nu - M_\nu}\right) \\ 0 \\ -\frac{1}{\sqrt{2}}\left(\sqrt{E_\nu + M_\nu} + \sqrt{E_\nu - M_\nu}\right) \end{pmatrix} \approx P_R\begin{pmatrix} 0 \\ \frac{1}{\sqrt{2}}\left(\sqrt{E_\nu} - \sqrt{E_\nu}\right) \\ 0 \\ -\frac{1}{\sqrt{2}}\left(\sqrt{E_\nu} + \sqrt{E_\nu}\right) \end{pmatrix} = P_R\begin{pmatrix} 0 \\ 0 \\ 0 \\ -\sqrt{2E_\nu} \end{pmatrix} = \begin{pmatrix} 0 \\ 0 \\ 0 \\ -\sqrt{2E_\nu} \end{pmatrix}$$

In order to get the total spin to add up to zero, and to have the momentum to be conserved, the muon must have the opposite spin and travel in the opposite direction. That means that the muon has a positive helicity as well. Since the muon does not travel close to the speed of light (due to its mass), its positive helicity state consists of a combination of left- and right-handed states, where only the left-handed state can take part in this decay. The left-handed projection of the Dirac spinor for the positive helicity state of the muon is[124]

$$P_L\begin{pmatrix} 0 \\ \frac{1}{\sqrt{2}}\left(\sqrt{E_\mu + m_\mu} - \sqrt{E_\mu - m_\mu}\right) \\ 0 \\ -\frac{1}{\sqrt{2}}\left(\sqrt{E_\mu + m_\mu} + \sqrt{E_\mu - m_\mu}\right) \end{pmatrix} = \begin{pmatrix} 0 \\ \frac{1}{\sqrt{2}}\left(\sqrt{E_\mu + m_\mu} - \sqrt{E_\mu - m_\mu}\right) \\ 0 \\ 0 \end{pmatrix}$$

If the muon was massless, the second entry of this spinor would vanish, and the positive helicity would get no contribution from the left-handed state at all. This would mean that the pion would not decay. If one compares the pion decay into a muon with a decay into an electron $\pi^- \to e^- \overline{\nu}_e$, the left-handed state of the electron gets a much smaller share of the positive helicity state. This comes from the fact that the electron mass is much smaller than the muon mass, and therefore the second entry in the column vector would get much smaller as well. The consequence is that nature prefers the pion decay into muons over the decay into electrons.

# Appendix L: Angular distribution of the neutrino flux

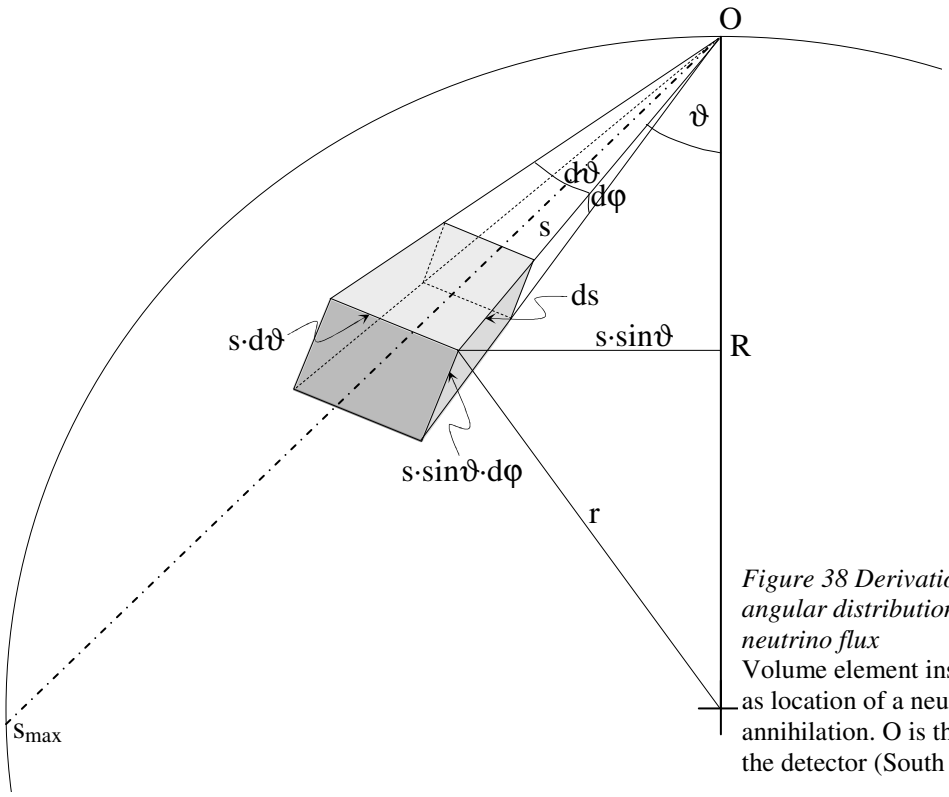


*Figure 38 Derivation of the angular distribution of the neutrino flux*
Volume element inside the Earth as location of a neutralino annihilation. O is the position of the detector (South Pole).

Consider the following volume element from the picture: $dV = s^2 \cdot \sin\vartheta \cdot ds \cdot d\vartheta \cdot d\varphi$. This volume element has the neutralino density $n(r)$. The neutrino production rate is $dR_\nu = \frac{1}{10}\langle\sigma_A v\rangle n^2(r) dV$ as in (77). These annihilations cause a certain neutrino flux from this volume element, which spreads out spherical. Since we measure the neutrino flux at the point O, the distance to the volume element is $s$ and the neutrino flux coming from this volume element is $d\Phi = \frac{\frac{1}{10}\langle\sigma_A v\rangle n^2(r)}{4\pi s^2} dV$ or $\frac{d\Phi}{d\Omega} = \frac{\frac{1}{10}\langle\sigma_A v\rangle n^2(r)}{4\pi s^2} s^2 ds$. For a particular solid angle element at point O one can detect neutrinos, which come from all points along the $s$ axis from 0 to $s_{\max} = \frac{R}{A}\cos\vartheta$, so that with (72)

$$\frac{d\Phi}{d\Omega} = \frac{\frac{1}{10}\langle\sigma_A v\rangle}{4\pi}\int_0^{s_{\max}} \frac{n^2(r)}{s^2}s^2\cdot ds = \frac{\frac{1}{10}\langle\sigma_A v\rangle n_0^2}{4\pi}\int_0^{s_{\max}}\left(\exp\left(-\frac{r^2}{2A^2}\right)\right)^2 ds$$
$$= \frac{\frac{1}{10}\langle\sigma_A v\rangle n_0^2}{4\pi}\int_0^{2R\cos\vartheta}\exp\left(-\frac{R^2+s^2-2Rs\cos\vartheta}{A^2}\right)\cdot ds$$

,

where $r=\sqrt{R^2+s^s-2Rs\cos\vartheta}$ is the distance between the volume element and the center of Earth. This integral can be evaluated by substituting $s\to s'=\frac{s-R\cos\vartheta}{A}$, which leads to

$$\int_{-\frac{R\cos\vartheta}{A}}^{\frac{R\cos\vartheta}{A}}\exp\left(-\frac{R^2+As'^2+2\sqrt{A}s'R\cos\vartheta+R^2\cos^2\vartheta-2R\sqrt{A}s'\cos\vartheta-2R^2\cos^2\vartheta}{A^2}\right)\cdot A\cdot ds'$$
$$=\int_{-\frac{R\cos\vartheta}{A}}^{\frac{R\cos\vartheta}{A}}\exp\left(-\frac{R^2+As'^2-R^2\cos^2\vartheta}{A^2}\right)\cdot A\cdot ds' = A\exp\left(-\frac{R^2}{A^2}\left(1-\cos^2\vartheta\right)\right)\int_{-\frac{R\cos\vartheta}{A}}^{\frac{R\cos\vartheta}{A}}\exp\left(-s'^2\right)\cdot ds'$$
$$= A\exp\left(-\frac{R^2}{A^2}\sin^2\vartheta\right)\left[\int_{-\frac{R\cos\vartheta}{A}}^{0}\exp\left(-s'^2\right)\cdot ds' + \int_0^{\frac{R\cos\vartheta}{A}}\exp\left(-s'^2\right)\cdot ds'\right]$$

In the first integral one can substitute $s'\to -s'$ and flip the integration borders. This leads to $A\exp\left(-\frac{R^2}{A^2}\sin^2\vartheta\right)\cdot 2\int_0^{\frac{R\cos\vartheta}{A}}\exp\left(-s'^2\right)\cdot ds' = A\exp\left(-\frac{R^2}{A^2}\sin^2\vartheta\right)\cdot\sqrt{\pi}\cdot\mathrm{erf}\left(\frac{R\cos\vartheta}{A}\right)$

Bringing everything together, and integrating over $\varphi$, one gets

$$\frac{d\Phi}{\cos\vartheta\cdot d\vartheta} = \frac{1}{20}\langle\sigma_A v\rangle n_0^2 A\sqrt{\pi}\exp\left(-\frac{R^2}{A^2}\sin^2\vartheta\right)\mathrm{erf}\left(\frac{R\cos\vartheta}{A}\right)$$

# Appendix M: Detection of neutrinos from neutralino annihilation in the sun

Additionally to the spin-independent interaction as it happens for the neutralino scattering in the Earth, there is a contribution of spin-dependent interaction for the neutralino scattering in the sun. This calculation is done first; afterwards the calculation for the spin-independent scattering is shown.

The capture rate for neutralinos in the sun via axial-vector interaction is given by[125]

$$\Gamma_C^{SD} = 1.3 \cdot 10^{25}\,\mathrm{s}^{-1} \frac{\rho / 0.3 \frac{\mathrm{GeV}}{\mathrm{cm}^3}}{\left(m_\chi / \mathrm{GeV}\right)\left(\bar{v} / 270 \frac{\mathrm{km}}{\mathrm{s}}\right)} \left(\sigma^{SD} / 10^{-40}\,\mathrm{cm}^2\right) S$$

which already includes the fact only hydrogen is relevant for spin-dependent scattering since it is the only nucleus with spin. The mass fraction of hydrogen in the sun is 77.2%; this value is included in the first factor. Furthermore, form-factor suppression can be neglected for hydrogen, since it has a very low mass.[125] The factor $S = \left( \frac{A^{1.5}}{1 + A^{1.5}} \right)^{1/1.5}$ with $A = \frac{3}{2} \frac{m_N m_\chi}{\left(m_N - m_\chi\right)^2} \left( \frac{\langle v_{esc} \rangle}{\bar{v}} \right)^2$ is the same as in 4.1. The average escape velocity of the sun (averaged over all depths) is $\langle v_{esc} \rangle = 1156\mathrm{km/s}$ and the root mean square speed of the neutralinos is 270km/s. This leads to $S = 0.24$.

The cross-section $\sigma^{SD}$ can be calculated as[126]

$$\sigma^{SD} = \frac{24 m_\chi^2 m_N^2 G_F^2}{\pi (m_\chi + m_N)^2} \left[ 0.3125 \left( Z_{23}^2 - Z_{24}^2 \right) - x_q^2 \left( -3.5 \cdot 10^{-10} \frac{Z_{23}^2}{\cos^2 \beta} + 3.72 \cdot 10^{-9} \frac{Z_{24}^2}{\sin^2 \beta} \right) + 0.173 Z_{22}^2 + 0.1125 Z_{22} Z_{21} + 0.122 Z_{21}^2 \right]^2$$

with $x_q^2 = \frac{m_W^2}{(m_\chi + m_N)^2 - (m_{\tilde{q}} + m_N)^2}$. The squark mass $m_{\hat{q}}$ is arbitrarily set to 200GeV. The values for the $Z_{2i}$ come from the components (55) of the particular neutralino which was chosen as an example at the end of 3.5 and was used through Chapter 4: to calculate the detection rate for the Earth: $\chi_2 = -0.08\tilde{B} + 0.07\tilde{W}^3 - 0.69\tilde{h}_1^0 + 0.71\hat{h}_2^0$ with a mass of $m_\chi = 100\text{GeV}$. The mass of the hydrogen nucleus is $m_N = 0.94\text{GeV}$. Bringing everything together gives $\sigma^{SD} = 6.94 \cdot 10^{-14}\,\text{GeV} = 2.7 \cdot 10^{-14}\,\text{mbarn} = 0.27 \cdot 10^{-40}\,\text{cm}^2$. Now the capture rate can be estimated to $\Gamma_C^{SD} = 8 \cdot 10^{21}\,\text{s}^{-1}$.

The capture rate for the spin-independent scattering is done in a similar way as for the Earth[125]

$$\Gamma_C^{SI} = 4.8 \cdot 10^{24}\,\text{s}^{-1} \frac{\rho / 0.3 \frac{\text{GeV}}{\text{cm}^3}}{(m_\chi / \text{GeV})(\bar{v} / 270 \frac{\text{km}}{\text{s}})} \sum_i F_i \frac{\sigma_i}{10^{-40}\,\text{cm}^2} f_i \phi_i S_i \frac{1}{m_{N_i} / \text{GeV}}$$

with the neutralino density $\rho = 0.3\text{GeV/cm}^3$, the neutralino mass $m_\chi = 100\text{GeV}$, and the root mean square speed of the neutralinos $\bar{v} = 270\text{km/s}$. This formula contains a sum over all nuclei $i$ found in the Earth, where one has to account for the nuclei specific parameters:[125]

- The mass of the nuclei $m_{N_i}$ (see Table 32)

- The fractional abundance of the nuclei $f_i$ (see Table 32)

- A factor depending on the velocity distribution of the nuclei in the Earth $\phi_i$ (see Table 32)

- The form-factor suppression which needs to be taken into account here (unlike for the Earth) since the energy transfer is much higher for scattering in the sun (due to the high escape velocity – see (56)): $F_i \approx F_i^{\inf} + \left(1 - F_i^{\inf}\right)\exp\left(-\left(\frac{\log m_\chi}{\log m_i^C}\right)^{\alpha_i}\right)$. The parameters are given in Table 32

- The kinematic suppression factor $S_i$ (see above at the calculation for the spin-dependent scattering)

- The scalar neutrino-nucleon cross-section $\sigma = \alpha_H \left(G_F m_N^2\right)^2 \frac{m_\chi^2}{\left(m_N + m_\chi\right)^2} \frac{m_Z^2}{m_H^4}$ as in 4.1 with $\alpha_H \approx 0.1$.

| | $N_i$ | $f_i$ | $\phi_i$ | $S_i$ * | $m_i^C$ | $F_i^{\inf}$ | $\alpha_i$ | $F_i$ * | $\sigma_i$ / cm$^{-40}$ * | $\Gamma_{Ci}$ / s$^{-1}$ ** |
|---|---|---|---|---|---|---|---|---|---|---|
| H | 1 | 0.772 | 3.16 | 0.24 | -- | -- | -- | 1.00 | 0.0016 | $4.9\cdot10^{19}$ |
| He | 4 | 0.209 | 3.40 | 0.66 | 18.2 | 0.986 | 1.58 | 0.99 | 0.39 | $2.4\cdot10^{21}$ |
| C | 12 | $3.87\cdot10^{-3}$ | 3.23 | 0.92 | 61.6 | 0.788 | 2.69 | 0.84 | 28 | $1.2\cdot10^{21}$ |
| N | 14 | $9.40\cdot10^{-4}$ | 3.23 | 0.94 | 75.2 | 0.613 | 2.69 | 0.73 | 50 | $3.8\cdot10^{20}$ |
| O | 16 | $8.55\cdot10^{-3}$ | 3.23 | 0.95 | 75.2 | 0.613 | 2.69 | 0.73 | 82 | $5.1\cdot10^{21}$ |
| Ne | 20 | $1.51\cdot10^{-3}$ | 3.23 | 0.97 | 75.2 | 0.613 | 2.69 | 0.73 | 190 | $1.7\cdot10^{21}$ |
| Mg | 24 | $7.39\cdot10^{-4}$ | 3.23 | 0.98 | 71.7 | 0.281 | 2.97 | 0.49 | 370 | $8.9\cdot10^{20}$ |
| Ni | 28 | $8.13\cdot10^{-4}$ | 3.23 | 0.99 | 71.7 | 0.281 | 2.97 | 0.49 | 640 | $1.5\cdot10^{21}$ |
| S | 32 | $4.65\cdot10^{-4}$ | 3.23 | 0.99 | 57.0 | 0.101 | 3.1 | 0.30 | 1000 | $7.4\cdot10^{20}$ |
| Fe | 56 | $1.46\cdot10^{-3}$ | 3.23 | 1.00 | 29.3 | 0.00677 | 3.36 | 0.065 | 7000 | $2.0\cdot10^{21}$ |

*Table 32 List of the properties of the most abundant nuclei in the sun*[125]

*These are values which were calculated with the formulas given above. The following values were used as an example: $m_\chi = 100\text{GeV}$, $\alpha_H = 0.1$, $m_H = 120\text{GeV}$.

**This is the fractional capture rate for each element

Putting everything together gives a capture rate for a 100GeV neutralino in the sun via spin-independent scattering of $\Gamma_C^{SI} = 1.6\cdot10^{22}\,\text{s}^{-1}$. Adding $\Gamma_C^{SD} = 8\cdot10^{21}\,\text{s}^{-1}$ from above leads to a total capture rate in the sun of $\Gamma_C = 2.4\cdot10^{22}\,\text{s}^{-1}$

The annihilation rate[77] was defined in (65) as $\Gamma_A = \frac{\Gamma_C}{2}\tanh^2\left(\sqrt{C\Gamma_C}t\right)$ with $C = \langle\sigma_A v\rangle\frac{V_2}{V_1^2}$, with the velocity-averaged annihilation cross-section $\langle\sigma_A v\rangle = 10^{-8}\,\mathrm{GeV}^{-2}$ as used in previous examples, and the effective volume $V_j = 8.5\cdot 10^{69}\,\mathrm{GeV}^{-3}\left(j\frac{m_\chi}{10\mathrm{GeV}}\right)^{-3/2}$. For a neutralino mass of 100GeV one gets $C = 2.0\cdot 10^{-53}\,\mathrm{s}^{-1}$. Using the age of the sun $t = 1.4\cdot 10^{17}\,\mathrm{s}$ and the previously calculated capture rate $\Gamma_C = 2.4\cdot 10^{22}\,\mathrm{s}^{-1}$, one can see that $\tanh(\sqrt{C\Gamma_C}t) = 1.0$. This means that neutralino capture and annihilation are in equilibrium which was not the case for the Earth. The annihilation rate becomes $\Gamma_A = \frac{1}{2}\Gamma_C = 1.2\cdot 10^{22}\,\mathrm{s}^{-1}$.

This neutrino flux at the Earth (at a distance of $R = 1.5\cdot 10^8\,\mathrm{km}$ from the sun) is $\Phi_\nu = \frac{\frac{1}{10}\Gamma_A}{4\pi R^2} = 4\cdot 10^4\,\mathrm{s}^{-1}\mathrm{km}^{-2}$, where the factor $\frac{1}{10}$ comes from the fact that about 10% of the annihilations lead to neutrinos. The muon rate (the neutrinos undergo a charged current interaction with a nucleon in the ice) is $\frac{dR_\mu}{dt} = \Phi_\nu\sigma_{\nu N\to\mu N'}(E)n_N V$, where $n_N = \rho_{ice}/m_{H_2O} = 3.3\cdot 10^{22}\,\mathrm{cm}^{-3}$ $n_N$ is the nucleon density of the ice in the detector and $\sigma_{\nu N\to\mu N'} = 5\cdot 10^{-39}\,\mathrm{cm}^2\frac{E_\nu}{\mathrm{GeV}} = 2.5\cdot 10^{-37}\,\mathrm{cm}^2$ is the energy dependent cross-section (for 50 GeV muon-neutrinos produced by the annihilations of 100 GeV neutralinos), and $V = 10^7\,\mathrm{m}^3$ is the detector volume. This leads to a muon rate of $\frac{dR_\mu}{dt} = 5\,\mathrm{year}^{-1}$ taking into account that AMANDA can observe the sun only during half of the year. Again, this result is only an estimation for an arbitrary neutralino model, where a lot of simplifications were introduced for each step of the calculation.

# Bibliography / References


[1] J.H. Oort, The force exerted by the stellar system in the direction perpendicular to the galactic plane and some related problems, Bulletin of the Astronomical Institutes of the Netherlands, Vol. 6 (1932), p.249
[2] F. Zwicky, Die Rotverschiebung von extragalaktischen Nebeln, Helvetica Physica Acta, Vol. 6, pp. 110-127
[3] F. Zwicky, On the Masses of Nebulae and Clusters of Nebulae, Astrophysical Journal Vol. 86 (1937), p. 217
[4] K. Begeman et al.: Extended rotation curves of spiral galaxies: dark haloes and modified dynamics, Mon. Not. R. astr. Soc. (1991) 249, p. 527
[5] Clowe et al, A direct empirical proof of the existence of dark matter, astro-ph/0608407
[6] NASA/WMAP science team, http://map.gsfc.nasa.gov/news/index.html
[7] NASA/WMAP science team, http://map.gsfc.nasa.gov/media/080997/index.html
[8] D.J. Raine, E.G. Thomas: An Introduction to the Science of Cosmology, p. 149
[9] E. Kolb, M. Turner: The Early Universe, pp. 78-80
[10] M. Roos: Introduction to Cosmology, 3rd edition, pp. 137-139
[11] E. Kolb, M. Turner: The Early Universe, pp. 322
[12] E. Kolb, M. Turner: The Early Universe, pp. 367-370
[13] M. Roos: Introduction to Cosmology, 3rd edition, p. 242
[14] D. Spergel: Particle Dark Matter, astro-ph/9603026 v1, 3
[15] E. Komatsu, et al.: Five-Year Wilkinson Microwave Anisotropy Probe (WMAP) Observations: Cosmological Interpretation
[16] Published by the Supernova Cosmology Project, Knop et al 2003, Spergel et al 2003, Allen et al 2002
[17] C. Amsler et al,. Physics Letters B667, 1 (2008), Particle Data Group, 20. Big-Bang nucleosynthesis, p. 6
[18] D. Spergel: Particle Dark Matter, astro-ph/9603026 v1, 5
[19] E. Bertschinger: Cosmological Dynamics, p. 25
[20] R. Bender: Galaxies, Cosmology and Dark matter, lecture, summer semester 2000, pp. 248-250
[21] E. Kolb, M. Turner: The Early Universe, pp. 123, 129
[22] E. Kolb, M. Turner: The Early Universe, pp. 370-374
[23] J. Ellis: Astroparticle Aspects of Supersymmetry, hep-ph/0103288 v1, p. 2-3
[24] X. Chen, Cosmic microwave background and large scale structure limits on the interaction between dark matter and baryons, astro-ph/0202496v2
[25] G.D. Mack, Towards Closing the Window on Strongly Interacting Dark Matter: Far-Reaching Constraints from Earth's Heat Flow, astro-ph/0705.4298v2
[26] S. Kolb, Collider Signatures of Sneutrino Dark Matter, hep-ph/9910542v2
[27] C. Arina, Sneutrino cold dark matter, a new analysis: relic abundance and detection rates, hep-ph/0709.4477v1
[28] J. Ellis, Gravitino Dark Matter in the CMSSM, hep-ph/0312262v4
[29] G. Jungman et al.: Supersymmetric dark matter (1995), pp. 33-37

[30] E. Kolb, M. Turner: The Early Universe, pp. 62-67
[31] E. Kolb, M. Turner: The Early Universe, pp. 119-130
[32] W. Greiner, B. Müller: Gauge Theory of Weak Interactions, pp. 79-81
[33] X. Tata: What is supersymmetry and how do we find it?, hep-ph/9706307 v1, p. 3
[34] S. Martin: A supersymmetry primer, hep-ph/9709356 v3, p. 3
[35] S. Martin: A supersymmetry primer, hep-ph/9709356 v3, p. 41
[36] R.N. Mohapatra, Unification and Supersymmetry
[37] S. Dawson: SUSY and such, hep-ph/9612229 v2, pp. 21, 22
[38] K. Cahill: Elements of Supersymmetry, hep-ph/9907295, pp. 20-22
[39] P. Binetruy: Supersymmetry: Theory, Experiment, and Cosmology, p. 38
[40] R.N. Mohapatra, Unification and Supersymmetry
[41] S.J. Gates, et al., Superspace or 1001 Lessons in Supersymmetry, hep-th/0108200
[42] J. Wess, J. Bagger, Supersymmetry and Supergravity
[43] P. Binetruy: Supersymmetry: Theory, Experiment, and Cosmology, p. 13
[44] X. Tata: Weak Scale Supersymmetry: From Superfields To Scattering Events, pp. 38-39
[45] A. Lyon: The basics of supersymmetry, D0 note 2523, p 10-12
[46] M, Srednicki, Quantum Field Theory, p 303
[47] X. Tata: What is supersymmetry and how do we find it?, hep-ph/9706307 v1, pp. 10-12
[48] S. Martin: A supersymmetry primer, hep-ph/9709356 v3, pp. 21, 22
[49] S. Martin: A supersymmetry primer, hep-ph/9709356 v3, pp. 24-26
[50] X. Tata: What is supersymmetry and how do we find it?, hep-ph/9706307 v1, p. 16
[51] S. Dawson: SUSY and such, hep-ph/9612229 v2, p. 6
[52] S. Martin: A supersymmetry primer, hep-ph/9709356 v3, pp. 8-9
[53] S. Dawson: SUSY and such, hep-ph/9612229 v2, p. 7
[54] S. Martin: A supersymmetry primer, hep-ph/9709356 v3, pp. 30, 34
[55] S. Dawson: SUSY and such, hep-ph/9612229 v2, p. 8
[56] S. Martin: A supersymmetry primer, hep-ph/9709356 v3, p. 29
[57] S. Martin: A supersymmetry primer, hep-ph/9709356 v3, p. 37
[58] S. Dawson: SUSY and such, hep-ph/9612229 v2, p. 9
[59] X. Tata: What is supersymmetry and how do we find it?, hep-ph/9706307 v1, p. 26
[60] C. Amsler et al., Physics Letters B667, 1 (2008), Particle Data Group, Physical Constants
[61] S. Martin: A supersymmetry primer, hep-ph/9709356 v4, pp. 70,71
[62] C. Amsler et al,. Physics Letters B667, 1 (2008), Particle Data Group, Supersymmetry I and II
[63] S. Martin: A supersymmetry primer, hep-ph/9709356 v4, p. 44
[64] A. Gould, Resonant Enhancements in weakly interacting massive particle capture by the earth, Astrophys. J. 321 (1987), 571
[65] G. Jungman et al.: Supersymmetric dark matter (1995), pp. 147-157
[66] C. Amsler et al,. Physics Letters B667, 1 (2008), Particle Data Group, 22. Dark Matter, p. 6
[67] G. Jungman et al.: Supersymmetric dark matter (1995), pp. 24-26
[68] G. Jungman et al.: Supersymmetric dark matter (1995), pp. 238-248

[69] G. Jungman et al.: Supersymmetric dark matter (1995), pp. 97, 105
[70] G. Jungman et al.: Supersymmetric dark matter (1995), pp. 148-151
[71] R. Nathaniel: Calculating Indirect Detection Rates For WIMP Dark Matter, pp. 12-16
[72] A. Gould, Gravitational Diffusion of Solar System WIMPs, Astrophys. J. 368 (1991), 610
[73] A. Gould, S.M.K Alam, Can Heavy WIMPs Be Captured by the Earth, astro-ph/9911288 v1
[74] G. Jungman et al.: Supersymmetric dark matter (1995), pp. 154-155
[75] G. Jungman et al.: Supersymmetric dark matter (1995), pp. 108-115
[76] T. Gaisser, F, F. Halzen, T. Stanev, Particle Astrophysics with High Energy Neutrinos, hep-ph/9410384v1, p. 44 / fig. 12
[77] G. Jungman et al.: Supersymmetric dark matter (1995), pp. 145-146
[78] G. Jungman et al.: Supersymmetric dark matter (1995), pp. 71-94
[79] F. Halzen et. al: Indirect Search for Neutralino Dark Matter with High Energy Neutrinos, hep-ph/0105182 v1, pp. 5-6
[80] J. Edsjö: WIMP mass determination with neutrino telescopes, hep-ph/9504283 v1, p. 2
[81] J. Edsjö: WIMP mass determination with neutrino telescopes, hep-ph/9504283 v1, p. 3
[82] G. Jungman et al.: Supersymmetric dark matter (1995), p. 178
[83] G. Jungman et al.: Supersymmetric dark matter (1995), p. 120
[84] A.V. Gladyshev, D.I. Kazakov, Supersymmetry and LHC. hep-ph/0606288v1, p. 16
[85] Icecube collaboration, The Neutrino, http://www.icecube.wisc.edu/info/neutrinos/
[86] C. Amsler et al,. Physics Letters B667, 1 (2008), Particle Data Group, 22. Dark Matter, p. 6
[87] T. Gaisser, F, F. Halzen, T. Stanev, Particle Astrophysics with High Energy Neutrinos, hep-ph/9410384v1, p. 4
[88] X. Bertou, et al., Physics of extremely high energy cosmic rays, astro-ph/0001516
[89] A. Gazizov, M. Kowalski, ANIS: High Energy Neutrino Generator for Neutrino Telescopes
[90] T. Gaisser, F, F. Halzen, T. Stanev, Particle Astrophysics with High Energy Neutrinos, hep-ph/9410384v1, p. 10
[91] Hamamatsu, Photomultiplier Tubes, Basics and Applications, 3rd edition
[92] R. Wischnewski et al, Perforance of the AMANDA II Detector
[93] IceCube NSF Proposal – Design and Description
[94] J. Ahrens et al, Muon Track Reconstruction and Data Selection Technique in AMANDA
[95] Icecube Internal Webpage
[96] E. Andres, et al., The AMANDA Neutrino Telescope: Principle of Operation and First Results, astro-ph/9906203v1
[97] W. Wagner, Design and Realisation of a new AMANDA Data Acquisition System with Transient Waveform Recorders, PhD thesis 2004, pp. 28-30
[98] Patrik Ekström, A Dark Matter Search with AMANDA, PhD thesis 2004, pp 27-28
[99] J. Ahrens, et al. Muon Track Reconstruction and Data Selection Techniques in AMANDA.
[100] P. Steffen, AMANDA Pattern Recognition, Presentation June, 22nd, 2002 at the AMANDA/Icecube meeting in Stockholm

[101] D. Pandel, Bestimmung von Wasser- und Detektorparametern und Rekonstruktion von Myonen bis 100 TeV mit dem Baikal-Neutrinoteleskop NT-72
[102] For this part I would like to thank Carlos de los Heros, Daan Hubert and Anna Davour for their help
[103] D. Chirkin, dCorsika update
[104] L. Bergström, J. Edsjö and P. Gondolo, Phys. Rev. D58 (1998) 103519
[105] C.P. de los Heros, Genniup Manual
[106] D. Chirkin, W. Rhode, Muon Monte Carlo: a high-precision tool for muon propagation through matter.
[107] S. Hundertmark, AMASIM Neutrino Detection Simulation Program
[108] A. Karle, Description of the Photon Transportation and Detection program.
[109] The L1/L2 filtering of the data was done by Carlos de los Heros (thank you!), while the MC samples were filtered by me. The L1/L2 steering files were written by Anna Davour (thank you!).
[110] A.C. Pohl, A Statistical Tool for Finding Non-Particle Events from the AMANDA Neutrino Telescope
[111] G.J. Feldman, R.D.Cousins, A Unified Approach to the Classical Statistical Analysis of Small Signals, physics/9711021v2
[112] G.C. Hill, K. Rawlins, Unbiased cut selection for optimal upper limits in neutrino detectors: the model rejection potential technique, astro-ph/0209350v1
[113] T.K. Gaisser, M. Honda, Flux of Atmospheric Neutrinos, Annu. Rev. Nucl. Part. Sci., 52 (2002), 155-199
[114] A. Achterberg et al, Five years of searches for point sources of astrophysical neutrinos with the AMANDA-II neutrino telescope, 2006.
[115] Figure from M. Ackermann, Searches for signals from cosmic point-like sources of high energy neutrinos in 5 years of AMANDA-II data. PhD thesis, Humboldt-Universität zu Berlin, 2006.
[116] A. Biron, Reconstruction Uncertainties due to Time Calibration Errors, AMANDA Internal report, 2000, p. 25
[117] J. Conrad et al, Including systematic uncertainties in confidence interval construction for Poisson statistics, Phys. Rev. D67 (2003) 012002
[118] L. Bergström, J. Edsjö and P. Gondolo, Phys. Rev. D58 (1998) 103519 The script can be found here http://lisa.physto.se/cgi-bin/edsjo/amanda/convfact.cgi
[119] IceCube collaboration, WIMP working group
[120] E. Kolb, M. Turner: The Early Universe, pp. 499-500
[121] K. Cahill: Elements of Supersymmetry, hep-ph/9907295, p. 8
[122] P. Binetruy: Supersymmetry: Theory, Experiment, and Cosmology, pp. 391-394
[123] R.D. Peccei, Neutrinos in Particle Physics and Cosmology, Maria Laach Lectures 2007
[124] P.J. Mulders: Quantum Field Theory, pp. 29-33
[125] G. Jungman et al.: Supersymmetric dark matter (1995), pp. 150-156
[126] M. Kamionkowski, Energetic neutrinos from heavy-neutralino annihalation in the Sun, Phys. Rev. D 44 (1991) Number 10, p. 3038